

The  $\Delta q$  Experiment: A Proposal to Jefferson Lab PAC42

**Measurements of Semi-Inclusive DIS Double-Spin Asymmetries  
on a Longitudinally Polarized  ${}^3\text{He}$  Target**

Jefferson Lab Hall A Collaboration, June 1, 2014.

(Draft version as of May 30, 2014.)

# Jefferson Lab Hall A Collaboration

K. Aniol

*Cal State University, Los Angeles, California*

G.B. Franklin, B. Quinn

*Carnegie Mellon University, Pittsburgh, Pennsylvania*

C. Chen, Nuruzzaman, L. Tang

*Hampton University, Hampton, Virginia*

A. J. R. Puckett (Co-Spokesperson)

*University of Connecticut, Storrs, Connecticut.*

X. Jiang (Co-Spokesperson)<sup>1</sup>

*Los Alamos National Laboratory, Los Alamos, New Mexico.*

A. Ahmidouch, S. Danagoulian

*North Carolina A&T State University, Greensboro, North Carolina*

W. Korsch

*University of Kentucky, Lexington, Kentucky.*

T. Holmstrom

*Longwood University, Farmville, Virginia*

L. El Fassi, C. E. Hyde

*Old Dominion University, Norfolk, Virginia*

R. Gilman, K. M. Mesick, R. Ransome

*Rutgers University, Piscataway, New Jersey.*

D. Higinbotham, M. Jones, C. Keppel, B. Wojtsekhowski

*Thomas Jefferson National Accelerator Facility, Newport News, Virginia.*

X. Bai, G. Cates, D. Day, D. Di, K .Gnanvo, C. Gu, N. Liyanage (Co-Spokesperson),

V. Nelyubin, H. Nguyen, O. Rondon

*University of Virginia, Charlottesville, Virginia.*

T. Averett

*College of William and Mary, Williamsburg, Virginia.*

V. Bellini

*University and INFN Catania, Italy.*

E. Cisbani

*INFN Roma-I, Italy.*

---

<sup>1</sup>Contact person. Email: [jiang@jlab.org](mailto:jiang@jlab.org)

J. Beričič, M. Mihovilovič, S. Širca, S. Štajner  
*J. Stefan Institute and Dept. of Physics, University of Ljubljana, Slovenia*

J. Annand, D. Hamilton, D.Ireland  
*University of Glasgow, Glasgow, Scotland, UK*

S. Riordan  
*University of Massachusetts, Amherst. Amherst, Massachusetts.*

## Abstract

Precision measurements of longitudinal double-spin asymmetries  $A_{1n}^h$ ,  $h = \pi^+, \pi^-, \pi^0, K^+, K^-$  in semi-inclusive deep-inelastic scattering on a longitudinally polarized  ${}^3\text{He}$  target are proposed. These asymmetries are sensitive to the flavor-separated quark helicity distributions of the nucleon. The flavor decomposition of nucleon spin is one of the major physics goals of the JLab 12 GeV upgrade. The experiment will reach high statistical figure-of-merit using a high-luminosity polarized  ${}^3\text{He}$  target and the BigBite and Super BigBite spectrometers in Hall A, in a configuration identical to approved experiment E12-09-018, that will measure transverse single-spin asymmetries in SIDIS. Compared to existing and planned measurements on proton and deuteron targets, SIDIS asymmetries measured on  ${}^3\text{He}$  provide superior sensitivity to  $\Delta d$  and  $\Delta \bar{d}$ . The kaon SIDIS asymmetries measured by this experiment will provide access to the polarized strange quark distribution  $\Delta s$ . A total of 30 days of running in Hall A are requested, including 20 days at 11 GeV and 10 days at 8.8 GeV. The proposed experiment will dramatically improve our knowledge of the flavor-separated quark helicity distributions in the valence region, and provide precision data for the next generation of NLO QCD global analysis of polarized PDFs.

# Contents

<b>1</b>	<b>Executive Summary</b>	<b>1</b>
<b>2</b>	<b>Introduction</b>	<b>3</b>
2.1	Nucleon Spin: Valence and Sea Quark Polarization . . . . .	3
2.2	Flavor Asymmetry of Unpolarized and Polarized Sea . . . . .	9
<b>3</b>	<b>SIDIS Spin Asymmetries <math>A_{1N}^h</math> and Methods of Spin-Flavor Decomposition</b>	<b>12</b>
3.1	Semi-Inclusive DIS kinematic definitions . . . . .	12
3.2	Beam-target double-spin asymmetries at leading order . . . . .	12
3.3	HERMES and COMPASS results from leading order purity method . . . . .	13
3.4	Neutron SIDIS asymmetries are sensitive to $\Delta d$ and $\Delta \bar{d}$ . . . . .	13
3.5	SIDIS Cross sections at the next-to-leading order . . . . .	14
3.6	NLO global QCD analysis of DIS and SIDIS data . . . . .	15
3.7	Method of spin-flavor decomposition . . . . .	16
3.7.1	LO Christova-Leader method to obtain $\Delta u_v(x)$ , $\Delta d_v(x)$ and $\Delta \bar{u}(x) - \Delta \bar{d}(x)$ .	16
3.7.2	NLO Christova-Leader method . . . . .	17
3.7.3	Cross check $\Delta q_v$ with measurement at RHIC . . . . .	18
3.7.4	Spin observables to check the leading order naive $x$ - $z$ separation . . . . .	19
<b>4</b>	<b>The Experiment</b>	<b>21</b>
4.1	Summary of Requested Beam Time Allocations . . . . .	21
4.2	Experiment Apparatus . . . . .	23
4.2.1	High-Luminosity Polarized ${}^3\text{He}$ Target . . . . .	24
4.2.2	BigBite Spectrometer . . . . .	24
4.2.3	Super BigBite Spectrometer . . . . .	25
4.2.4	Ring-Imaging Cherenkov detector for SBS . . . . .	26
4.3	Experiment Plan and Expected Results . . . . .	28
4.3.1	Monte Carlo Simulation . . . . .	28
4.3.2	SIDIS Cross Section Model . . . . .	30
4.3.3	SIDIS Kinematic Coverage . . . . .	31
4.3.4	Event Rates . . . . .	32
4.3.5	Projected Statistical Uncertainties in $A_{1n}^h(x, z)$ . . . . .	33
4.3.6	Resolution, background and trigger rates . . . . .	36
4.3.7	Comparison to Existing Data . . . . .	36
4.3.8	Comparison to Other Approved Experiments and Unique Advantages of This Proposal . . . . .	37
	Unique advantages of this proposal . . . . .	40

<b>5 Expected Results on Nucleon Spin-Flavor Decomposition</b>	<b>42</b>
5.1 Systematic uncertainties on asymmetry $A_{1He}^h$ and $A_{1n}^h$ . . . . .	42
5.2 Expected results from NLO global fit and impacts to DSSV2008 . . . . .	43
5.3 Expected results from Leading-Oder “purity” method . . . . .	43
5.4 Expected results from Leading-Oder Christova-Leader method . . . . .	43
5.4.1 Statistical uncertainties of the combined asymmetries $A_{1He}^{\pi^+ - \pi^-}$ . . . . .	43
5.4.2 Valence quark polarization . . . . .	43
5.4.3 Statistical uncertainty on $\Delta\bar{u} - \Delta\bar{d}$ when combined with JLab-12 GeV proton target data . . . . .	45
5.5 Other systematic uncertainties . . . . .	46
5.5.1 Effective nucleon polarization in ${}^3\text{He}$ . . . . .	46
5.5.2 $\pi$ - $N$ final state interaction . . . . .	47
5.5.3 Target fragmentation and vector meson production . . . . .	47
5.5.4 Corrections from non-vanishing $A_\perp^n$ (or $A_{LT}^n$ ) . . . . .	47
<b>Acknowledgments</b>	<b>47</b>
<b>A Collaboration Responsibilities</b>	<b>49</b>
<b>B HERMES and COMPASS Results and NLO Global Fits</b>	<b>50</b>
B.1 HERMES and COMPASS results of Leading-Oder purity method . . . . .	50
B.2 NLO global fit to DIS and SIDIS Data . . . . .	52
<b>C Leading-Order SIDIS Asymmetries and SU(2) Assumptions</b>	<b>55</b>
C.1 Leading-order SIDIS asymmetries $A_{1N}^h$ . . . . .	55
C.1.1 Spin-dependent and spin-independent cross sections at LO . . . . .	56
C.1.2 The asymmetries expressed in “fixed- $z$ purity” . . . . .	56
C.2 Systematic uncertainties in Chritova-Leader LO method introduced by SU(2) symmetry violations . . . . .	57
C.2.1 Case-1: only $u$ and $d$ fragmentation functions violate SU(2) . . . . .	58
C.2.2 Case-12: only $\bar{u}$ and $\bar{d}$ fragmentation functions violate SU(2) . . . . .	58
<b>D Projected Results of SIDIS Asymmetries on <math>{}^3\text{He}</math> and Neutron</b>	<b>60</b>
<b>E Projected Results of LO Spin-Flavor Decomposition</b>	<b>66</b>
E.1 Statistical Uncertainties of LO Christova-Leader Method of Spin-Flavor Decomposition . . . . .	66
<b>References</b>	<b>69</b>

# Chapter 1

## Executive Summary

Nucleon spin-flavor decomposition is one of the main challenges facing our field, and is one of the key physics issues that have driven the JLab-12 GeV upgrade.

The physics goals of this experiment includes:

- Provide the highest precision data set of polarized neutron ( ${}^3\text{He}$ ) double-spin asymmetry  $A_{1n}^h$  in several hadron production channels in semi-inclusive Deep-Inelastic Scattering reactions, with hadron  $h = \pi^+, \pi^-, \pi^0, K^+, K^-$ , on a dense grid, over a wide range of  $(x, Q^2, z)$  and also cover a wide range of hadron transverse momentum  $p_T^h$ .
- Investigate the behavior of  $A_{1n}^h$  on its dependency of  $Q^2, z$ , hadron  $p_T^h$  and azimuthal angle  $\phi_h$ . Compare with the expected behavior from Next-Leading-Order QCD predictions, identify possible higher-twist effects
- Through the method of Next-Leading-Order (NLO) QCD global fit , obtain the best knowledge of nucleon spin-flavor decomposition. Provide clear answers to the questions: Are sea quarks polarized ? Do sea up-quarks carry positive helicity as STAR W asymmetry data suggested ? How much helicity each quark flavor carry ?
- Through the method of Leading-Order “Purity Method” obtain 5-flavor nuclear spin decomposition, as applied in HERMES and COMPASS data, obtain point-to-point extraction on ratios of  $\Delta q/q$  for each quark flavor [ $\Delta u/u, \Delta d/d, \Delta \bar{u}/\bar{u}, \Delta \bar{d}/\bar{d}$  and  $(\Delta s + \Delta \bar{s})/(s + \bar{s})$ ].
- Through deliberate careful control of phase space and detection efficiency, obtain high precision results on the charged pion difference asymmetry,  $A_{1n}^{\pi^+ - \pi^-}$ , a charge and flavor non-singlet observable which is only sensitive to valence quark polarization  $\Delta d_v - 1/4\Delta u_v$ . When combined with future JLab SIDIS data on a polarized proton target, obtain  $\Delta u_v, \Delta d_v$  and polarized sea flavor asymmetry  $\Delta \bar{u} - \Delta \bar{d}$ , and their first moments, such as  $\int [\Delta \bar{u}(x) - \Delta \bar{d}(x)] dx$ .
- Through high precision SIDIS hadron multiplicity data within the same experimental set up, on unpolarized reference cell runs, carry out a self-consistent simultaneous NLO fit on multiplicity and spin asymmetry to constrain fragmentation function and parton helicity. High precision results from this experiment will build up into a JLab-12 GeV SIDIS database for future NLO fits, which will also include data from polarized proton and deuteron targets.

This proposal follows the footsteps of earlier JLab-6GeV spin-flavor decomposition proposals and an earlier JLab-12 GeV proposal. Using the same high luminosity polarized  ${}^3\text{He}$  target system and two large acceptance spectrometer combination: BigBite Spectrometer as the electron arm and

Super-BigBite Spectrometer (SBS) as the hadron arm, as in the approved Transversity experiment, this experiment will be able to collect data in the same run group as the Transversity experiment, with a longitudinal target spin setting. The main features of this experiment includes:

- World highest luminosity polarized target ( ${}^3\text{He}$ ), with an average polarization of 65%.
- Two large acceptance magnetic spectrometers, as electron-arm and hadron-arm detect SIDIS in coincidence. The best Figure-Of-Merit for neutron SIDIS spin asymmetries.
- The highest  $Q^2$  available for SIDIS reactions at JLab-12 GeV, completely complimentary to that of the SoLID experiment in Hall A. At beam energies of 11 GeV and 8.8 GeV, provide coverage to a wide range of  $Q^2$ , similar to that of CLAS12.
- Clear particle identification and reliable separation of  $\pi/K$  over the entire range of hadron momentum through the Ring Imaging Cherenkov detector in SBS.
- Identical detection phase space for positively-charged and negatively-charged hadrons, and through SBS magnetic field reversal, a unique feature that is ideal to measure SIDIS yield differences of  $\pi^+ - \pi^-$  and corresponding asymmetries.

# Chapter 2

## Introduction

### 2.1 Nucleon Spin: Valence and Sea Quark Polarization

The last two decades has seen remarkable progress in the knowledge of the polarized parton distribution functions (pPDF)  $\Delta q_f(x)$ . The most precise and clearly interpreted data are from inclusive deep-inelastic lepton scattering (DIS) experiments at CERN and SLAC. However, the information available from inclusive DIS process has inherent limitations. As the cross sections are only sensitive to  $e_q^2$ , the quark charge square, an inclusive experiment probes quarks and anti-quarks on an equal footing, and it is only possible to determine combinations of  $\Delta q + \Delta \bar{q}$ , but never the valence  $\Delta q_v = \Delta q - \Delta \bar{q}$  nor the sea  $\Delta \bar{q}$  separately. Therefore it is not sensitive to the symmetry breaking in the sea sector. Through inclusive DIS measurements, only one particular flavor non-singlet can be directly inferred i.e.  $\Delta q_3(x, Q^2) = \Delta u + \Delta \bar{u} - \Delta d - \Delta \bar{d}$ . The additional assumption of  $SU(3)_f$  flavor symmetry allows the hyperon beta decay data to constrain the first moments of  $\Delta q$ . The well-cited result of this approach is that quark helicities seem to make a small net contribution to the nucleon spin, and the strange sea appears to be negatively polarized.

Are sea quarks polarized ? Do sea quarks' polarization have a flavor asymmetry similar to that of their unpolarized part ? How much do sea quarks polarization (helicity) contribute to nucleon's 1/2-spin ? These question has been tantalizing us for the last two decades. From inclusive deep-inelastic spin asymmetry measurements, combined with hyperon decay data assuming  $SU(3)$  symmetry, it was suggested that sea quarks' polarization are negative [1], contributing about 10% of nucleon's spin. However, semi-inclusive DIS data from SMC [2], HERMES [3], and COMPASS [4] experiment concluded that sea quark's polarization are consistent with zero, as shown in Fig. 2.1, and that sea quarks' polarization do not have a flavor asymmetry.

The sensitivity to each individual quark flavor can also be realized in semi-inclusive deep inelastic scattering (SIDIS) in which one of the leading hadrons in quark fragmentation is also detected. Since the leading hadrons from the current fragmentation carry information about the struck quark's flavor, detection of the leading hadron effectively "tags" the quark flavor. Therefore, SIDIS offers an unique opportunity for determining the spin, flavor, and sea structure of the nucleon [?], thereby significantly enriching our understanding of QCD and the nucleon structure. High precision polarized SIDIS data on the proton and the neutron (in a deuteron or a  ${}^3\text{He}$  nuclei) allows a flavor decomposition of nucleon spin structure, which could lead to the discovery of a possible flavor-asymmetry in the polarized sea. A decade ago, in 2004, the HERMES collaboration published the results of a leading order spin flavor decomposition from polarized proton and deuteron data, and extracted the sea quark polarizations [3] for the first time without assuming flavor symmetry of polarized sea. Unlike the predictions of several theoretical models, HERMES

data indicated that within the available statistics  $\Delta\bar{u} - \Delta\bar{d}$  is consistent with an unbroken  $SU(2)_f$  symmetry. These results have been confirmed in 2010 by the COMPASS Collaboration [4], as shown in Fig.2.2.

Very recently, from RHIC STAR experiment's W-boson spin asymmetry measurements [8], as shown in Fig 2.3, the data strongly favor a positively polarized sea up-quark. Indeed, when include the STAR W data, NLO global fit DSSV [7] favors a positive anti-up quark polarization and a negative anti-down quark polarization, as shown in Fig. 2.4. The STAR data agree reasonably well when compared with the predictions of Statistical Model (BBS2008) [9], in which a sea up-quark polarization as large as 20%, as shown in Fig.2.3 right-panel.

The HERMES data demonstrated that, within the experimental precision, the semi-inclusive double-spin asymmetries  $A_{1N}^h$  at  $\langle Q^2 \rangle = 2.5 \text{ GeV}^2$  agree reasonably well with the SMC data [2] at  $\langle Q^2 \rangle = 10 \text{ GeV}^2$ , COMPASS asymmetry data on proton and deuteron targets [4] averaged at  $\langle Q^2 \rangle = 10 \text{ GeV}^2$ , also agree well with HERMES data.

This non-trivial agreement indicates that semi-inclusive asymmetries have rather weak  $Q^2$  dependencies and the expected violation of naive leading order  $x$ - $z$  separation is not large. The apparent “precocious  $Q^2$ -scaling” suggests that at a modest  $Q^2$ , such as at HERMES  $\langle Q^2 \rangle = 2.5 \text{ GeV}^2$  and at  $\langle Q^2 \rangle = 4.0 \text{ GeV}^2$  for this experiment, information on the quark distributions and quark polarizations should be reasonably well-preserved in semi-inclusive reactions at JLab-12GeV. Ji, Ma and Yuan have explicitly proved [11] that QCD factorization is valid for SIDIS with hadrons emitted in the current fragmentation region with low transverse momentum  $p_{\perp h} \ll Q$ . QCD factorization of spin-dependent cross sections in SIDIS and Drell-Yan has also been proved for the low  $p_{\perp h}$  case [12]. JLab-6GeV Hall-C (E00-108) SIDIS results [13, 14], on unpolarized SIDIS cross section ratios of proton and deuteron with 5.5 GeV beam and  $\langle Q^2 \rangle = 2.3 \text{ GeV}^2$ , also indicated that the leading order naive  $x$ - $z$  separation is rather close to the reality.

It was pointed out by Frankfurt et al. [15], Close and Milner [16] and by Christova and Leader [17, 18] that if the yield-difference helicity-asymmetries  $A_{1N}^{\pi^+ - \pi^-}$  are measured with high precision, quark polarization  $\Delta u_v$ ,  $\Delta d_v$  and  $\Delta\bar{u} - \Delta\bar{d}$  can be extracted at leading order independent of the knowledge of fragmentation functions. Even at the next-to-leading order, information on the valence quark polarizations is well-preserved in the combined asymmetries  $A_{1N}^{\pi^+ - \pi^-}$ , due to the fact that contributions from gluons as well as sea-quarks cancel exactly to all orders of QCD [18] in this charge and flavor non-singlet combination. In practice, the combined asymmetry  $A_{1N}^{\pi^+ - \pi^-}$  poses more experimental challenges, since precise knowledge on hadron phase spaces and detection efficiencies are required. This experiment, in JLab-12GeV Hall A with the Super BigBite and BigBite two spectrometer combination, is specifically designed to measure  $A_{1N}^{\pi^+ - \pi^-}$  with well-controlled hadron phase space and detector efficiencies, very different from other SIDIS measurements carried out earlier such as the HERMES and the COMPASS experiments, this experiment will use two independent magnetic spectrometers. By flipping the magnetic polarity of the hadron spectrometer, identical phase spaces between  $\pi^+$  and  $\pi^-$  reaction can be achieved such that the combined asymmetry  $A_{1He}^{\pi^+ - \pi^-}$  can be determined with high precision. At  $Q^2$  of  $2.0 \sim 6.7 \text{ GeV}^2$ , and  $x = 0.110 \sim 0.600$  ??? xxx.xx, this experiment will provide independent precision data on  $\Delta d_v - \frac{1}{4}\Delta u_v$ . When combined with the expected world data on polarized proton, to obtain  $\Delta u_v - \Delta d_v$ , this experiment will provide the opportunity to address the polarized sea asymmetry  $\Delta\bar{u} - \Delta\bar{d}$ .

At the next-to-leading order, following the well established formalism [?], tools of NLO QCD global fits, which include data sets from both inclusive and semi-inclusive reactions, have become available. As a standard procedure, such global NLO QCD fit has also included RHIC  $pp$  data [?], in forward  $\pi^0$  and jet longitudinal double-spin asymmetries  $A_{LL}^{\pi^0}$ , and  $A_{LL}^{jet}$ . Although there's a reason-

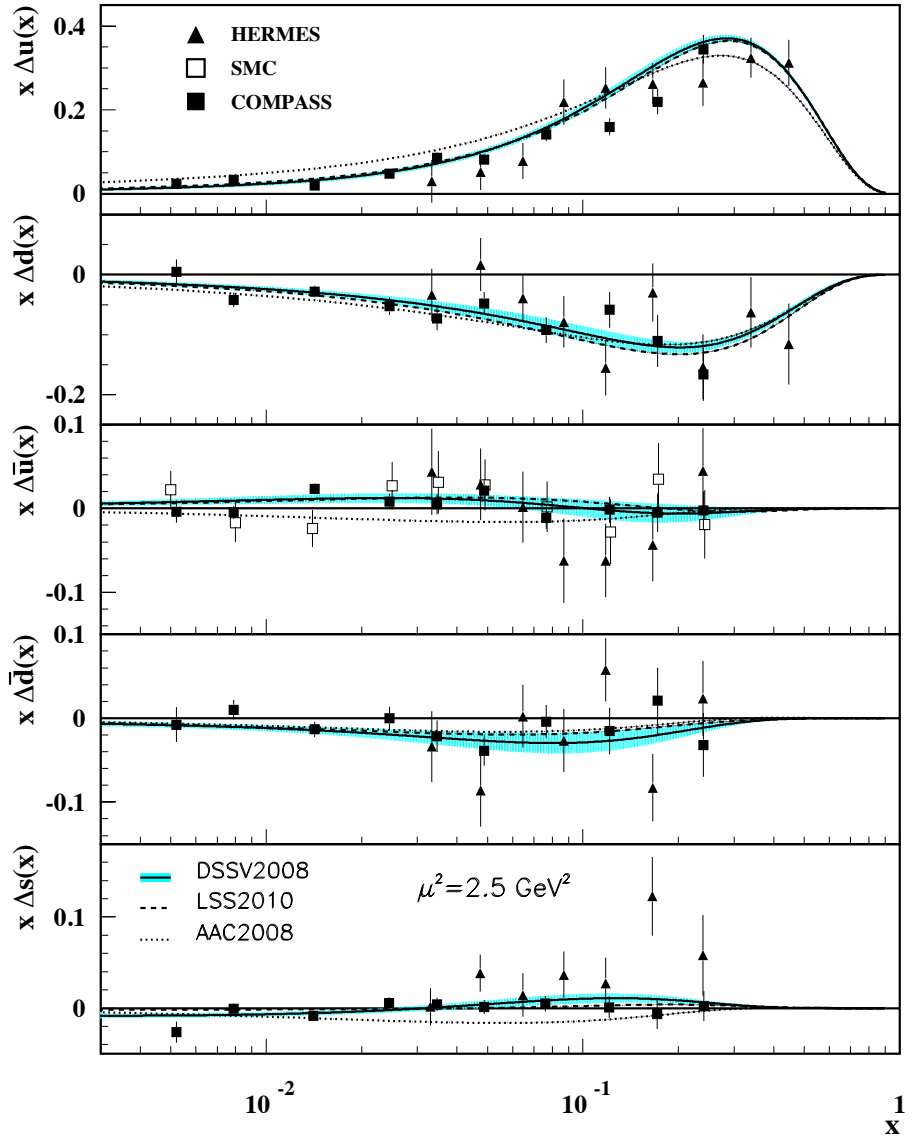


Figure 2.1: From Particle Data Group (2013). As extracted from SIDIS data on proton and deuteron targets, distributions of  $x$  times the polarized parton distributions  $\Delta q(x)$  (where  $q = u, d, \bar{u}, \bar{d}, s$ ), using the LSS2010 [5], AAC2008 [6], and DSSV2008 [7] parameterizations at a scale  $\mu^2 = 2.5 \text{ GeV}^2$ , showing the error corridor of the latter set (corresponding to a one-unit increase in  $\chi^2$ ). Points represent data from semi-inclusive positron (HERMES [3]) and muon (SMC [2] and COMPASS [4]) deep inelastic scattering given at  $Q^2 = 2.5 \text{ GeV}^2$ . SMC results are extracted under the assumption that  $\Delta \bar{u}(x) = \Delta \bar{d}(x)$ .

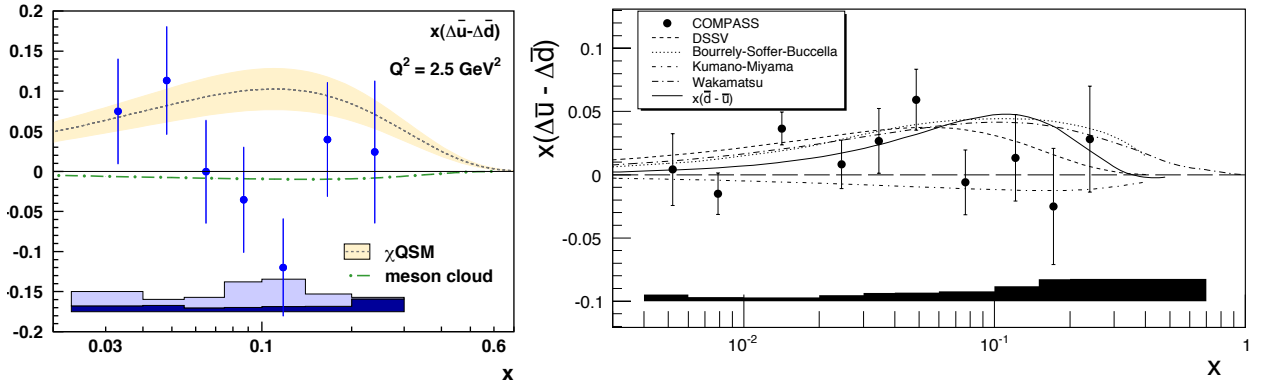


Figure 2.2: The HERMES result [3] of polarized sea flavor asymmetry  $x(\Delta\bar{u} - \Delta\bar{d})$  is shown on the left, COMPASS result [4] is shown on the right. The error bars are statistical, while the shaded bands at the bottom indicate the systematic uncertainties.

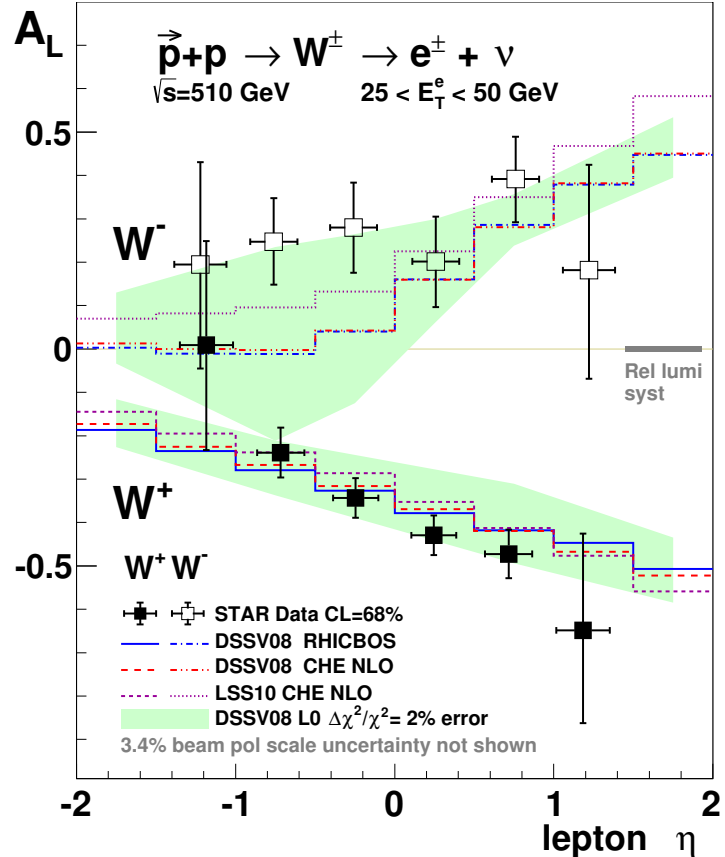


Figure 2.3: Recent results from STAR [8], longitudinal single-spin asymmetry,  $A_L$ , for  $W^\pm$  production as a function of lepton pseudorapidity,  $\eta_e$ , in comparison with theory predictions.

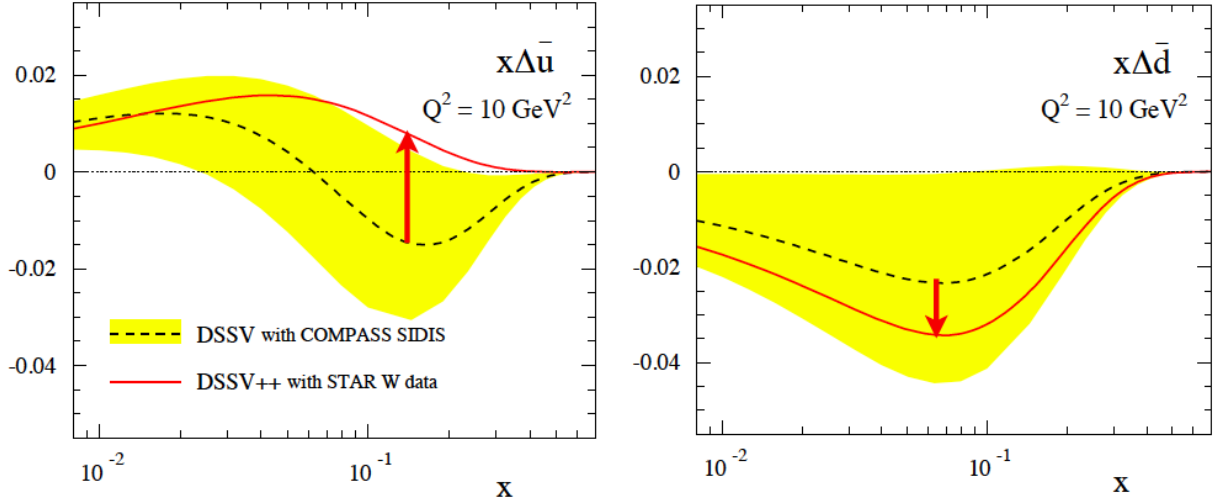


Figure 2.4: While including the STAR W data [8], NLO global fit DSSV [7] favors a positive anti-up quark polarization and a negative anti-down quark polarization.

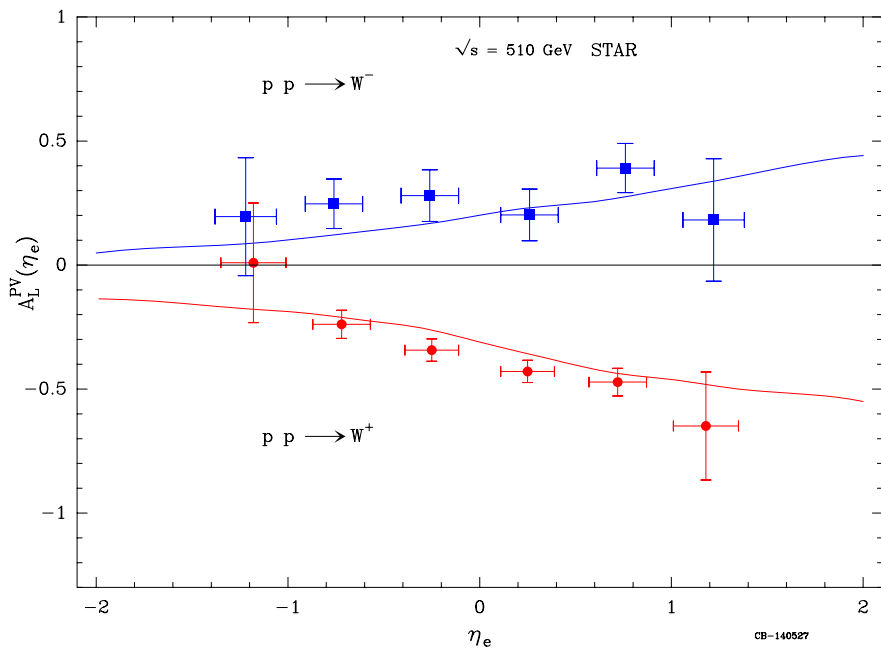


Figure 2.5: BBS2008 prediction [10], compared with STAR  $A_L$  data of  $W^\pm$  production [8].

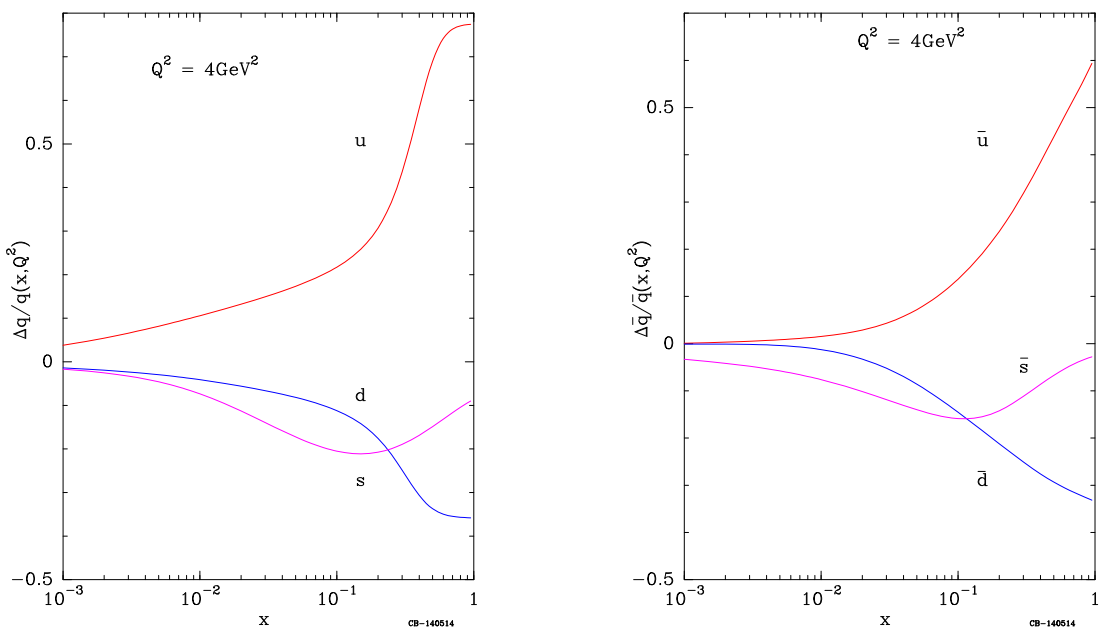


Figure 2.6: BBS2008 prediction [9], of ratio for different quark flavor  $\Delta q/q$  (left) and  $\Delta \bar{q}/\bar{q}$  at the kinematics of this experiment  $Q^2 = 4.0 \text{ GeV}^2$ .

able set of SIDIS data on proton and deuteron targets, from HERMES and COMPASS experiment, and soon from JLab-6GeV CLAS eg1-dvcs run group, the world data on SIDIS asymmetries currently only includes one  $^3\text{He}$  data set, with rather large error bars, obtained by HERMES in 1996. The high statistics  $^3\text{He}$  data from this experiment, adding much precise neutron SIDIS asymmetries to the world data sample, will serve as stringent constraints on pPDFs through NLO global fits [?]. Data from this experiment will indirectly constrain  $\Delta g$  through NLO global fit. The main source of this sensitivity to  $\Delta g$  comes from the  $Q^2$ -evolutions of the inclusive  $g_1$  structure function, but now with sea and valence contributions much better separated by semi-inclusive data in the global fit [?, ?]. Therefore, data from this experiment will independently verify the recent claim of a small positive gluon polarization based on RHIC inclusive jet data.

Jefferson Lab Hall A, with its high luminosity polarized  $^3\text{He}$  target, has the unique advantage in providing high precision neutron asymmetry data in nucleon spin studies. In obtaining quark helicity information from neutron, the Figure-of-Merit of a polarized  $^3\text{He}$  target has always been much better than from that of a polarized deuteron target from ND<sub>3</sub>. For example, Hall A data on inclusive  $A_{1n}$  and  $d_2^n$  measurements [?] has improved previous world knowledge by an order of magnitude in each case. The Hall A polarized  $^3\text{He}$  target system has been under continuous improvements over the last decade. In 2008-2009, it reached an average in-beam polarization of 60% during the Neutron Transversity experiment (E06-010). A large acceptance magnetic spectrometer, the BigBite spectrometer, with its electron detector package has been operated successfully in Neutron Transversity and d2n experiments. The planned Hall A Super-Big-Bite spectrometer with a large solid angle and a large momentum acceptance, in addition to its unique particle identification Ring Imaging Cherenkov detector (RICH), in combination with the high polarization electron beam at 11 GeV, a high luminosity and high polarization  $^3\text{He}$  target, make it possible for a dramatic improvement on the world data set of SIDIS neutron asymmetries.

## 2.2 Flavor Asymmetry of Unpolarized and Polarized Sea

Fermilab experiment E866 reported measurements of the yield ratio of Drell-Yan muon pairs from an 800 GeV/c proton beam incident on hydrogen and deuterium [19, 20]. The data suggested a significantly asymmetric light sea quark distribution over an appreciable range in  $x$ ; the asymmetry  $\bar{d}/\bar{u}$  peaked around  $x = 0.18$ , as shown in Fig. 2.7. Furthermore, based on the E866 data and the CTEQ4M global-fit values of  $\bar{u} + \bar{d}$ , the values of  $\bar{d}(x) - \bar{u}(x)$  were extracted, with the moment  $\int_0^1 [\bar{d}(x) - \bar{u}(x)] dx = 0.118 \pm 0.012$ . Many theoretical models, including the meson cloud model, the chiral-quark model, the Pauli-blocking model, the instanton model, the chiral-quark soliton model and the statistical model, have been proposed to explain the  $\bar{d}/\bar{u}$  asymmetry. These models can describe the  $\bar{d} - \bar{u}$  reasonably well. However, they all have difficulties explaining the  $\bar{d}/\bar{u}$  ratio at  $x > 0.2$ .

Since the unpolarized sea demonstrates a significant flavor asymmetry, one naively speculates a sizable flavor asymmetry also exists for the polarized sea in the same  $x$ -region. Indeed, many theory models have specific implications for the spin structure of the nucleon sea. For example, the Pauli-blocking model and the instanton model both predict a large asymmetry,  $\int_0^1 [\Delta\bar{u}(x) - \Delta\bar{d}(x)] dx = \frac{5}{3} \cdot \int_0^1 [\bar{d}(x) - \bar{u}(x)] dx \approx 0.2$ . In the chiral-quark soliton model,  $\Delta\bar{u} - \Delta\bar{d}$  appears in leading-order ( $N_c^2$ ) in a large  $N_c$ -expansion, while  $\bar{d} - \bar{u}$  appears in the next-to-leading order ( $N_c$ ). On the other hand, those meson cloud models which only include the  $\pi$ -meson predict  $\Delta\bar{u} = \Delta\bar{d} = 0$  since the sea-quarks reside in a spin-0  $\pi$ -meson. By considering a vector meson ( $\rho$ ) cloud, non-zero sea polarization was predicted. A summary of theoretical predictions [?] of  $I_\Delta = \int_0^1 [\Delta\bar{u}(x) - \Delta\bar{d}(x)] dx$  are given in Table. 2.1. If the flavor asymmetry of the polarized sea is indeed as large as the

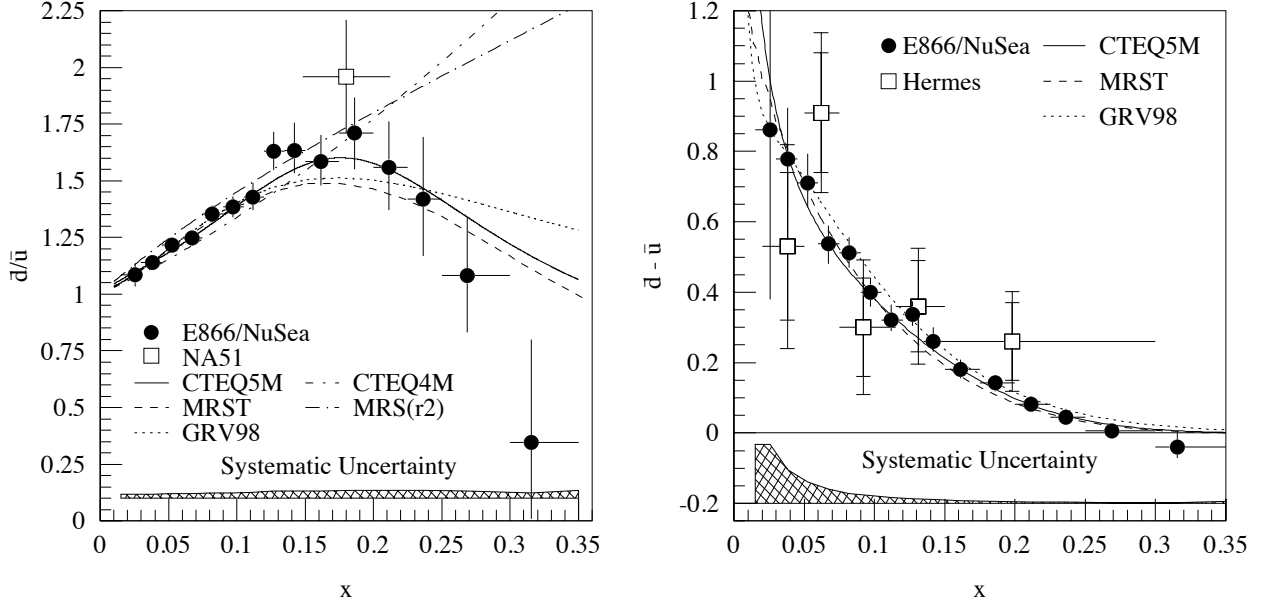


Figure 2.7: The Fermilab E866 results [19, 20]. The left plot shows the ratio  $\bar{d}/\bar{u}$  as a function of  $x$ , the right plot shows the extracted value of  $\bar{d}(x) - \bar{u}(x)$  together with the HERMES semi-inclusive DIS results.

predictions of many models shown in Table. 2.1, it would imply that a significant fraction of the Bjorken sum,  $\int_0^1 [g_1^p(x) - g_1^n(x)] dx$ , comes from the flavor asymmetry of the polarized nucleon sea. The high statistics  ${}^3\text{He}$  data from this experiment, together with the expected world proton data, will provide us with the first opportunity to discover the asymmetry in the polarized sea.

Model	$I_\Delta$ prediction	Authors and References
Meson cloud ( $\pi$ -meson)	0	Eichten <i>et al.</i> [?], Thomas [?]
Meson cloud ( $\rho$ -meson)	$\simeq -0.007$ to $-0.027$	Fries <i>et al.</i> [?]
Meson cloud ( $\pi - \rho$ interference)	$= -6 \int_0^1 g_1^p(x) dx \simeq -0.7$	Boreskov <i>et al.</i> [?]
Meson cloud ( $\rho$ and $\pi - \rho$ interference)	$\simeq -0.004$ to $-0.033$	Cao <i>et al.</i> [?]
Meson cloud ( $\rho$ -meson)	$< 0$	Kumano <i>et al.</i> [?]
Meson cloud ( $\pi - \sigma$ interference)	$\simeq 0.12$	Fries <i>et al.</i> [?]
Pauli-blocking (bag model)	$\simeq 0.09$	Cao <i>et al.</i> [?]
Pauli-blocking (ansatz)	$\simeq 0.3$	Gluck <i>et al.</i> [?]
Pauli-blocking	$= \frac{5}{3} \int_0^1 [\bar{d}(x) - \bar{u}(x)] dx \simeq 0.2$	Steffens [?]
Chiral-quark soliton	0.31	Dressler [?]
Chiral-quark soliton	$\simeq \int_0^1 2x^0.12 [\bar{d}(x) - \bar{u}(x)] dx$	Wakamatsu <i>et al.</i> [?]
Instanton	$= \frac{5}{3} \int_0^1 [\bar{d}(x) - \bar{u}(x)] dx \simeq 0.2$	Dorokhov [?]
Statistical	$\simeq \int_0^1 [\bar{d}(x) - \bar{u}(x)] dx \simeq 0.12$	Bourrely <i>et al.</i> [?]
Statistical	$> \int_0^1 [\bar{d}(x) - \bar{u}(x)] dx \simeq 0.12$	Bhalerao [?]

Table 2.1: A summary [?] of theoretical predictions of  $I_\Delta = \int_0^1 [\Delta \bar{u}(x) - \Delta \bar{d}(x)] dx$ .

# Chapter 3

# SIDIS Spin Asymmetries $A_{1N}^h$ and Methods of Spin-Flavor Decomposition

The principle goal of spin-dependent SIDIS experiments is to perform flavor decomposition of nucleon spin structure taking advantage of flavor tagging. In this section, we first express the SIDIS cross sections and asymmetries at leading order (LO) and summarize the HERMES results of “purity method” (more details in Appendix). After introducing the next-to-leading order cross sections, we summarize the NLO global QCD analysis method. We will then outline new methods of flavor decomposition: the Christova-Leader method at leading order and next-to-leading order. Theoretical models of polarized light sea asymmetry  $\Delta\bar{u}-\Delta\bar{d}$  is summarized at the end. Throughout this proposal, SU(2) isospin symmetry and charge conjugation invariance are assumed and heavy quark contributions are neglected.

## 3.1 Semi-Inclusive DIS kinematic definitions

## 3.2 Beam-target double-spin asymmetries at leading order

At the leading order, the SIDIS process is separated into a hard-scale quark scattering followed by a soft-scale hadronization. The “naive  $x$ - $z$  separation” assumption, on which the SMC and HERMES analysis were based, implies that the spin-independent ( $\sigma^h$ ) and the spin-dependent ( $\Delta\sigma^h$ ) cross sections follow:

$$\sigma^h(x, z) = \sum_f e_f^2 q_f(x) \cdot D_{q_f}^h(z), \quad \Delta\sigma^h(x, z) = \sum_f e_f^2 \Delta q_f(x) \cdot D_{q_f}^h(z), \quad (3.1)$$

where  $x = Q^2/2M\nu$ ,  $z = E_h/\nu$ . The fragmentation functions  $D_{q_f}^h(z)$  represent the probability that a quark  $f$  fragments into a hadron  $h$ .

Considering the beam and target polarization ( $P_B$  and  $P_T$ ), and the dilution factor ( $f^h = \sigma_{pol.N}^h/\sigma_{allN}^h$ ), which accounts for the unpolarized nucleons in the target, the double-spin asymmetry [?] for a longitudinally polarized beam on a longitudinally polarized target is :

$$A_{||}^h = f^h P_B P_T \cdot \mathcal{P}_{kin} \cdot A_{1N}^h, \quad (3.2)$$

the kinematic factor  $\mathcal{P}_{kin}$  is:

$$\mathcal{P}_{kin} = \mathcal{D} \cdot (1 + \gamma\eta) \cdot \frac{1 + R}{1 + \gamma^2}, \quad (3.3)$$

in which

$$\begin{aligned}\eta &= \frac{2\gamma(1-y)}{2-y}, & \mathcal{D} &= \frac{1-(1-y)\epsilon}{1+\epsilon \cdot R}, \\ \epsilon^{-1} &= 1 + 2(1+\nu^2/Q^2) \tan^2(\theta_e/2),\end{aligned}\quad (3.4)$$

$\mathcal{D}$  is the virtual photon polarization,  $R(x, Q^2) = \sigma_L/\sigma_T$  accounts for the longitudinal component of the virtual photon and  $y = \nu/E_0$ ,  $\gamma^2(x, Q^2) = 4M^2x^2/Q^2$ . In the current fragmentation regime, the virtual photon asymmetry is defined as:

$$A_{1N}^h(x, Q^2, z) \equiv \frac{\Delta\sigma^h(x, Q^2, z)}{\sigma^h(x, Q^2, z)} = \frac{\sum_f e_f^2 \Delta q_f(x, Q^2) \cdot D_{qf}^h(z, Q^2)}{\sum_f e_f^2 q_f(x, Q^2) \cdot D_{qf}^h(z, Q^2)}. \quad (3.5)$$

Each individual measurement on  $A_{1N}^h(x, Q^2, z)$  provides an independent constrain on the polarized parton distributions  $\Delta q_f(x, Q^2)$ . Data from HERMES on proton and deuteron, and from COMPASS on deuteron target are summarized in Appendix-A.

In principle, the asymmetry  $A_{1N}^h$  depends on both variables  $x$  and  $z$ , its  $x$ -dependency comes from parton distributions and  $z$ -dependency comes from fragmentation functions. Generally speaking, accurate knowledge of the fragmentation functions is crucial in order to extract quark polarizations from the measured asymmetries according to Eq. 3.5. However, in some special combinations, if  $\sigma^h$  and  $\Delta\sigma^h$  happen to have similar  $z$ -dependencies, as their ratio, the asymmetry will end up with a weak or even vanishing  $z$ -dependency. This type of cancellation can provide us with much cleaner observables to access quark polarizations without the complication of fragmentation functions. For example, Christova and Leader pointed out [?] that at the leading order, under the assumptions of SU(2) isospin symmetry and charge conjugation invariance, the fragmentation functions canceled exactly in the combined  $h^+ \pm h^-$  double-spin asymmetries. Furthermore, if strange quark contribution can be neglected, the semi-inclusive asymmetry  $A_{1N}^{\pi^+ + \pi^-}$  is reduced to the inclusive asymmetry  $A_{1N}$ . Indeed, at the next-to-leading order, the  $z$ -dependence of  $A_{1N}^{\pi^+ + \pi^-}$  is predicted to be very small [?].

### 3.3 HERMES and COMPASS results from leading order purity method

The HERMES [3] and COMPASS [4] result of flavor decomposition results are shown in Fig. 2.1. As expected,  $u$ -quarks are strongly polarized in the direction of proton spin, while  $d$ -quarks are polarized opposite to the proton spin. The sea quark polarizations are consistent with zero. Fig. ?? right panel shows the HERMES result of  $x(\Delta\bar{u} - \Delta\bar{d})$  together with predictions of a broken  $SU(2)_f$  symmetry [?, ?]. The data are consistent with an unbroken  $SU(2)_f$  sea symmetry.

The HERMES and COMPASS results left much room for improvement, with respect to statistical accuracies, especially on  $\Delta\bar{u} - \Delta\bar{d}$ . In addition, the validity and the stability of the leading order purity method needs to be independently verified. As pointed out by many authors, the issue of leading order violation of naive  $x$ - $z$  separation and the intrinsic uncertainties of the fragmentation Monte Carlo simulation need to be quantitatively addressed at a level appropriate to the sea contribution [?].

### 3.4 Neutron SIDIS asymmetries are sensitive to $\Delta d$ and $\Delta\bar{d}$

For a proton and a deuteron target, one expects  $u$ -quark dominates in SIDIS cross section due to  $e_q^2$  weighting, as in the case of HERMES and COMPASS data. However, one expects  $\Delta d$  to be better

constrained by neutron data from a polarized  ${}^3\text{He}$  target. In Fig. 3.1, the fractional contribution of each quark flavor to the SIDIS cross sections  $\sigma_q^h/\sigma_{all}$  are shown for proton (left panel) and neutron (right panel), that is:

$$\frac{\sigma_q^h}{\sigma_{all}} = \frac{e_q^2 \cdot q(x, Q^2) \cdot D_q^h(z, Q^2)}{\sum_f e_f^2 \cdot q_f(x, Q^2) \cdot D_f^h(z, Q^2)}. \quad (3.6)$$

Sensitivities to  $d$  and  $\bar{d}$  contributions in the neutron SIDIS cross sections are clearly demonstrated. The HERMES collaboration collected limited polarized  ${}^3\text{He}$  data back in 1996, which formed the basis of its first flavor decomposition paper [?].

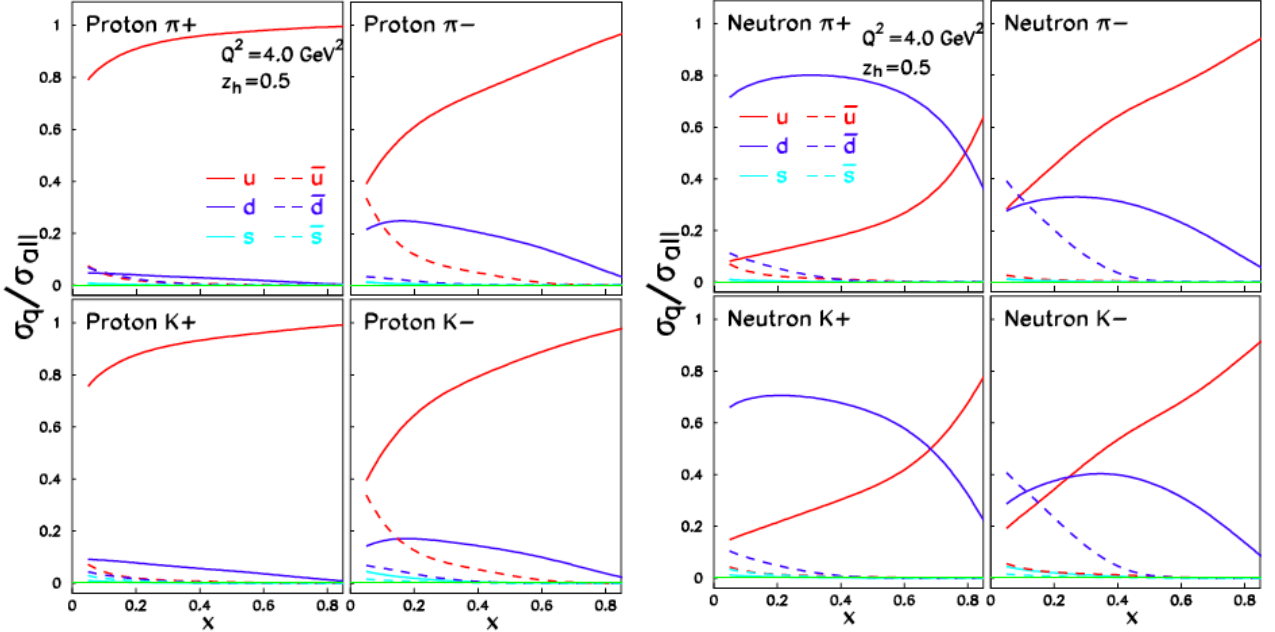


Figure 3.1: The left panel shows the proton SIDIS cross sections as fractional contributions from each quark flavor at  $Q^2 = 4.0 \text{ GeV}^2$  and  $z = 0.5$ . The right panel shows the case for a neutron.

### 3.5 SIDIS Cross sections at the next-to-leading order

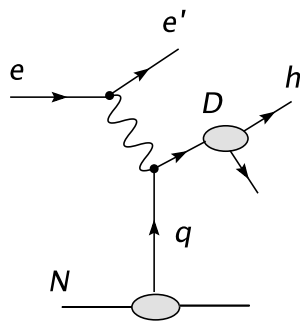
The naive  $x-z$  separation is no longer valid at the next-to-leading order when gluon diagrams in Fig. 3.2 are considered. However, the exact form of the NLO cross section has been well-known [?]. At NLO, the terms of  $q(x) \cdot D(z)$  and  $\Delta q(x) \cdot D(z)$  in Eq. 3.1 are added with the double convolutions of the type  $q \otimes C \otimes D$  and  $\Delta q \otimes \Delta C \otimes D$  in which  $C$  and  $\Delta C$  are well-known Wilson coefficients [?]:

$$[q \otimes C \otimes D](x, z) = \int_x^1 \frac{dx'}{x'} \int_z^1 \frac{dz'}{z'} q\left(\frac{x}{x'}\right) C(x', z') D\left(\frac{z}{z'}\right). \quad (3.7)$$

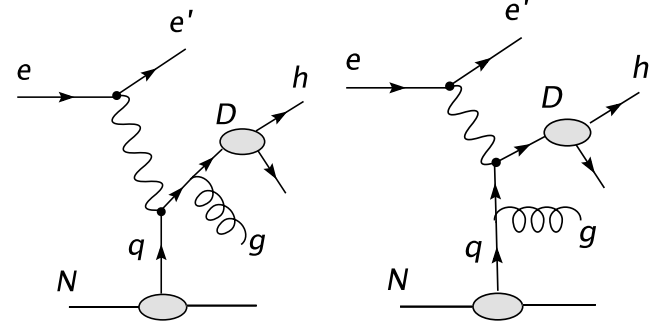
We define the short-hand notation:

$$qD + \frac{\alpha_s}{2\pi} q \otimes C \otimes D = q \left[ 1 + \otimes \frac{\alpha_s}{2\pi} C \otimes \right] D, \quad (3.8)$$

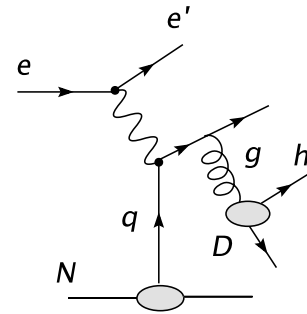
LO:



NLO-qq:



NLO-qg:



NLO-gq:

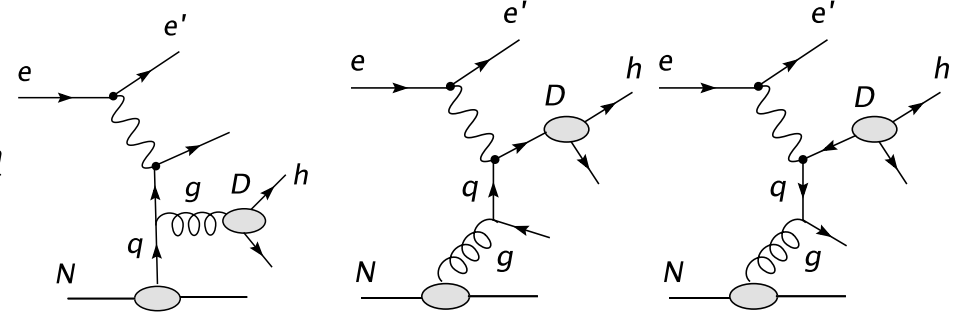


Figure 3.2: SIDIS diagrams at leading order (LO) and the next-to-leading order (NLO).

at NLO instead of Eq. 3.1, we have:

$$\begin{aligned} \sigma^h(x, z) &= \sum_f e_f^2 q_f \left[ 1 + \otimes \frac{\alpha_s}{2\pi} \mathcal{C}_{qq} \otimes \right] D_{q_f}^h \\ &+ \left( \sum_f e_f^2 q_f \right) \otimes \frac{\alpha_s}{2\pi} \mathcal{C}_{qg} \otimes D_G^h + G \otimes \frac{\alpha_s}{2\pi} \mathcal{C}_{gq} \otimes \left( \sum_f e_f^2 D_{q_f}^h \right), \end{aligned} \quad (3.9)$$

$$\begin{aligned} \Delta\sigma^h(x, z) &= \sum_f e_f^2 \Delta q_f \left[ 1 + \otimes \frac{\alpha_s}{2\pi} \Delta C_{qq} \otimes \right] D_{q_f}^h \\ &+ \left( \sum_f e_f^2 \Delta q_f \right) \otimes \frac{\alpha_s}{2\pi} \Delta C_{qg} \otimes D_G^h + \Delta G \otimes \frac{\alpha_s}{2\pi} \Delta C_{gq} \otimes \left( \sum_f e_f^2 D_{q_f}^h \right). \end{aligned} \quad (3.10)$$

It is also well-known that in the Mellin- $n$  space, the double-convolutions factorize into simple products under moments, and the parton distributions can be recovered by an inverse Mellin transformation with all moments of Wilson coefficients already calculated [?].

### 3.6 NLO global QCD analysis of DIS and SIDIS data

At the next-to-leading order, the cross sections in Eq. 3.5 are replaced by Eq. 3.9 and Eq. 3.10. Following the well established [7] formalism, tools of NLO QCD global fits, which include data sets from inclusive and semi-inclusive reactions as well as  $pp$  data, have become available [7], and the uncertainties of the pPDF can be addressed in the global fits. With the HERMES results, the

polarized SIDIS data have a non-negligible weight in the combined global analysis, comparable to that of inclusive data. It helped to constrain the sea quark and gluon polarization complementing the information obtained from DIS. The NLO global fit [7] to the existing DIS and SIDIS data are shown in Fig. B.5 in Appendix.

The precision data from SIDIS spin asymmetry  $A_{1N}^h$ , especially adding the neutron asymmetries such as from this experiment to the world data, will serve as stringent constraints on pPDFs through NLO global fits, constraining sea quark polarization, and indirectly constrain gluon polarization  $\Delta g(X)$ , as shown through an earlier study for the JLab-6GeV case [21]. An “impact study” of the expected data from this experiment to the global NLO fit (DSSV++) is currently underway, the final results of the “impact study” will be presented at the PAC42 presentation. Since the combined asymmetries  $A_{1n}^{\pi^+ - \pi^-}$  are also measured in this experiment, the result of the NLO global fit can be cross checked with that from the NLO Christova-Leader method.

### 3.7 Method of spin-flavor decomposition

#### 3.7.1 LO Christova-Leader method to obtain $\Delta u_v(x)$ , $\Delta d_v(x)$ and $\Delta \bar{u}(x) - \Delta \bar{d}(x)$

At the leading order, under isospin symmetry and charge conjugation invariance, the fragmentation functions cancel exactly in the combined asymmetry  $A_{1N}^{\pi^+ \pm \pi^-}$ . In addition, higher-twist terms in the fragmentation functions are also expected to be largely canceled [?]. In the quantities related to  $\sigma^{\pi^+} - \sigma^{\pi^-}$  which is a charge and flavor non-singlet combination, sea-quarks and gluons do not contribute at any QCD-order [?].

From the Appendix, at leading order , for polarized protons, polarized deuterons and polarized neutrons <sup>1</sup> (in  ${}^3\text{He}$ ), we have:

$$A_{1p}^{\pi^+ - \pi^-}(\vec{p}) = \frac{\Delta\sigma_p^{\pi^+} - \Delta\sigma_p^{\pi^-}}{\sigma_p^{\pi^+} - \sigma_p^{\pi^-}} = \frac{4\Delta u_v - \Delta d_v}{4u_v - d_v}, \quad (3.11)$$

$$A_{1d}^{\pi^+ - \pi^-}(\vec{p} + \vec{n}) = \frac{\Delta\sigma_d^{\pi^+} - \Delta\sigma_d^{\pi^-}}{\sigma_d^{\pi^+} - \sigma_d^{\pi^-}} = \frac{\Delta u_v + \Delta d_v}{u_v + d_v}, \quad (3.12)$$

$$A_{1He}^{\pi^+ - \pi^-}(\vec{n} + 2\vec{p}) = \frac{\Delta\sigma_{He}^{\pi^+} - \Delta\sigma_{He}^{\pi^-}}{\sigma_{He}^{\pi^+} - \sigma_{He}^{\pi^-}} = \frac{4\Delta d_v - \Delta u_v}{7u_v + 2d_v}. \quad (3.13)$$

Measurements on three different targets will over-determine  $\Delta u_v$  and  $\Delta d_v$ . Proton and deuteron measurements are more sensitive to  $\Delta u_v$ , measurements on  ${}^3\text{He}$  are more sensitive to  $\Delta d_v$ . One can re-write the last relation as:

$$(\Delta d_v - \frac{1}{4}\Delta u_v)_{LO} = \frac{1}{4}(7u_v + 2d_v) A_{1He}^{\pi^+ - \pi^-}. \quad (3.14)$$

This method of flavor decomposition involves helicity asymmetries of cross section differences. Kinematics need to be carefully chosen such that  $\pi^+$  and  $\pi^-$  cross sections are reasonably different. Error propagation on  $A_{1N}^{\pi^+ - \pi^-}$  make this method unfavorable when  $\pi^-/\pi^+$  ratio approaches unity. Fig. B.3 in Appendix illustrates this point by comparing the purity method with the Christova-Leader method for HERMES data [?].

---

<sup>1</sup> After the effective neutron polarization (86.5%) in  ${}^3\text{He}$  is taken into account and the correction corresponding to the small proton polarization (2.8%) is applied.

We can obtain the leading order quantity  $\Delta u_v - \Delta d_v$  from combinations of either proton and  $^3\text{He}$  data or proton and deuteron data as:

$$(\Delta u_v - \Delta d_v)_{LO} = \frac{1}{5} \left[ (4u_v - d_v) A_{1p}^{\pi^+ - \pi^-} - (7u_v + 2d_v) A_{1He}^{\pi^+ - \pi^-} \right], \quad (3.15)$$

$$(\Delta u_v - \Delta d_v)_{LO} = \frac{1}{5} \left[ 2(4u_v - d_v) A_{1p}^{\pi^+ - \pi^-} - 3(u_v + d_v) A_{1d}^{\pi^+ - \pi^-} \right]. \quad (3.16)$$

On the other hand, constrained by the inclusive data, the flavor non-singlet quantity at all QCD orders is:

$$\Delta q_3(x, Q^2) \equiv (\Delta u + \Delta \bar{u}) - (\Delta d + \Delta \bar{d}). \quad (3.17)$$

The polarized sea asymmetry at all QCD orders is:

$$\Delta \bar{u} - \Delta \bar{d} = \frac{1}{2} \Delta q_3 - \frac{1}{2} (\Delta u_v - \Delta d_v). \quad (3.18)$$

At the leading order, we have:

$$\Delta q_3(x, Q^2)|_{LO} = 6 [g_1^p(x, Q^2) - g_1^n(x, Q^2)], \quad (3.19)$$

$$[\Delta \bar{u}(x) - \Delta \bar{d}(x)]_{LO} = 3 [g_1^p(x) - g_1^n(x)] - \frac{1}{2} (\Delta u_v - \Delta d_v)|_{LO}. \quad (3.20)$$

### 3.7.2 NLO Christova-Leader method

At the next-to-leading order, under isospin symmetry and charge conjugation invariance, the NLO convolution terms become much simpler in quantities that are related to  $\sigma^{\pi^+} - \sigma^{\pi^-}$ . Since the gluon-related terms are identical for  $\pi^+$  and  $\pi^-$  production, they drop out in the differences [?]:

$$A_{1p}^{\pi^+ - \pi^-}(\vec{p}) = \frac{(4\Delta u_v - \Delta d_v) [1 + \otimes(\alpha_s/2\pi) \Delta C_{qq} \otimes] (D^+ - D^-)}{(4u_v - d_v) [1 + \otimes(\alpha_s/2\pi) \mathcal{C}_{qq} \otimes] (D^+ - D^-)}, \quad (3.21)$$

$$A_{1d}^{\pi^+ - \pi^-}(\vec{p} + \vec{n}) = \frac{(\Delta u_v + \Delta d_v) [1 + \otimes(\alpha_s/2\pi) \Delta C_{qq} \otimes] (D^+ - D^-)}{(u_v + d_v) [1 + \otimes(\alpha_s/2\pi) \mathcal{C}_{qq} \otimes] (D^+ - D^-)}, \quad (3.22)$$

$$A_{1He}^{\pi^+ - \pi^-}(\vec{n} + 2\vec{p}) = \frac{(4\Delta d_v - \Delta u_v) [1 + \otimes(\alpha_s/2\pi) \Delta C_{qq} \otimes] (D^+ - D^-)}{(7u_v + 2d_v) [1 + \otimes(\alpha_s/2\pi) \mathcal{C}_{qq} \otimes] (D^+ - D^-)}. \quad (3.23)$$

in which  $\Delta u_v$  and  $\Delta d_v$  evolve as non-singlets and do not mix with sea-quark and gluon densities. Therefore, measurements of  $A_{1N}^{\pi^+ - \pi^-}$  can determine  $\Delta u_v$  and  $\Delta d_v$  at the next-to-leading order without any consideration of gluon and sea distributions. The double-convolution terms in Eq. 3.21 are expected to introduce negligible  $z$ -dependency in  $A_{1N}^{\pi^+ - \pi^-}$  at the kinematics of this experiment, as demonstrated in calculation of de Florian, Navarro and Sassot [?].

The first moment of  $\Delta u_v - \Delta d_v$  is related to the moment of  $\Delta \bar{u} - \Delta \bar{d}$  through the Bjorken sum rule at all orders of QCD [?]. The Bjorken sum rule, written in terms of the moment  $\Delta_1 q = \int_0^1 dx \Delta q$ ,

$$\begin{aligned} \Delta_1 q_3 &\equiv [\Delta_1 u(Q^2) + \Delta_1 \bar{u}(Q^2)] - [\Delta_1 d(Q^2) + \Delta_1 \bar{d}(Q^2)] \\ &= \left| \frac{g_A}{g_v} \right| = 1.2670 \pm 0.0035 \quad \text{valid in all QCD orders.} \end{aligned} \quad (3.24)$$

Therefore, valid in all QCD orders, we have:

$$\int_0^1 (\Delta \bar{u} - \Delta \bar{d}) dx = \frac{1}{2} \left| \frac{g_A}{g_v} \right| - \frac{1}{2} \int_0^1 (\Delta u_v - \Delta d_v) dx. \quad (3.25)$$

In other words, if one measures the valence quark moment  $\Delta u_v - \Delta d_v$  precise enough, for example to  $\delta[\Delta_1 u_v - \Delta_1 d_v] = \pm 0.05$ , one can pin down the polarized sea asymmetry, to  $\delta[\Delta_1 \bar{u} - \Delta_1 \bar{d}] = \pm 0.025$ , that's eight standard deviations from the prediction of Chiral Quark Soliton model.

A well-defined procedure has been given [?] to obtain the moment  $\Delta_1 u_v - \Delta_1 d_v$  directly from the measured asymmetries  $A_{1N}^{\pi^+ - \pi^-}$  without first solving Eq. 3.21 point-to-point. The stability of this procedure has been demonstrated [?] using the HERMES-1999 data.

From the deuteron data alone, one can also form  $\Gamma_v$ , the first moment of  $\Delta u_v + \Delta d_v$ , and extract at leading order the moment:

$$\int_0^1 (\Delta \bar{u} + \Delta \bar{d}) dx = 3\Gamma_1^N - \frac{1}{2}\Gamma_v + \frac{1}{12}a_8 \quad (3.26)$$

where  $\Gamma_1^N$  is the moment of  $g_1^N = (g_1^p + g_1^n)/2$  from inclusive data, and  $a_8 = 3F - D$  is from hyperon  $\beta$ -decays.

The COMPASS deuteron target results [?] of  $A_d^{h^+ - h^-}$  are shown in Fig. 3.3. The extracted valence quark polarization  $x(\Delta u_v + \Delta d_v)$  and the running- $x_{min}$  integral of  $\Delta u_v + \Delta d_v$  are shown in Fig. 3.4. The fact that the integral of  $\Delta u_v + \Delta d_v$  is significantly different from that of assumption of a symmetrical polarized sea indicated that the sign of  $\Delta \bar{u}$  is opposite to that of  $\Delta \bar{d}$ .

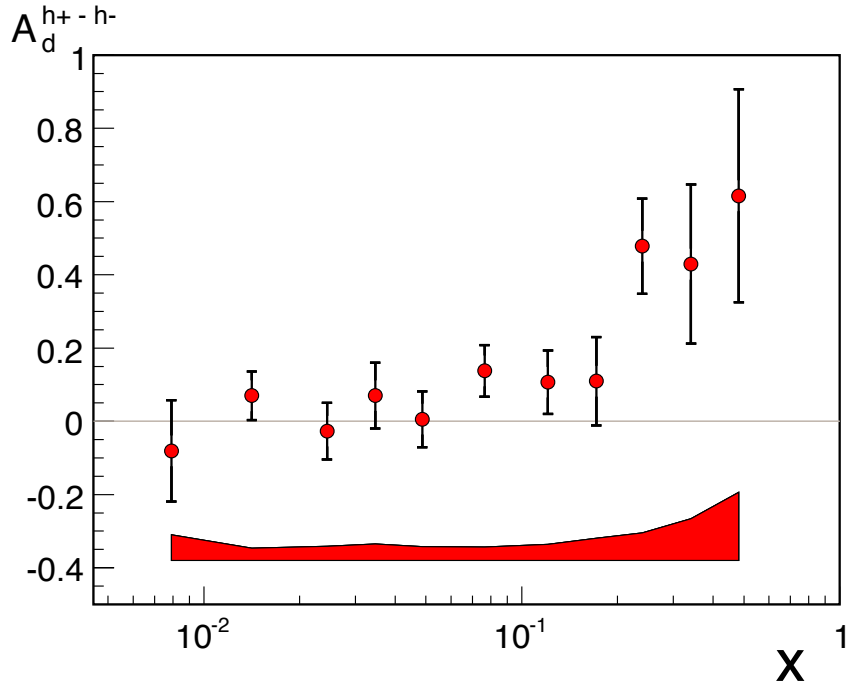


Figure 3.3: Charged hadron combined asymmetry  $A_d^{h^+ - h^-}$  measured by COMPASS [?].

### 3.7.3 Cross check $\Delta q_v$ with measurement at RHIC

At RHIC,  $\Delta q$  can be measured through  $W^\pm$  decays [?]. Since the  $Q^2$ -evolutions of valence densities  $\Delta q_v$  are well understood in QCD, consistency cross checks can be made between JLab data at  $\langle Q^2 \rangle = 4.0 \text{ GeV}^2$  and RHIC data at  $Q^2 = M_W^2$ .

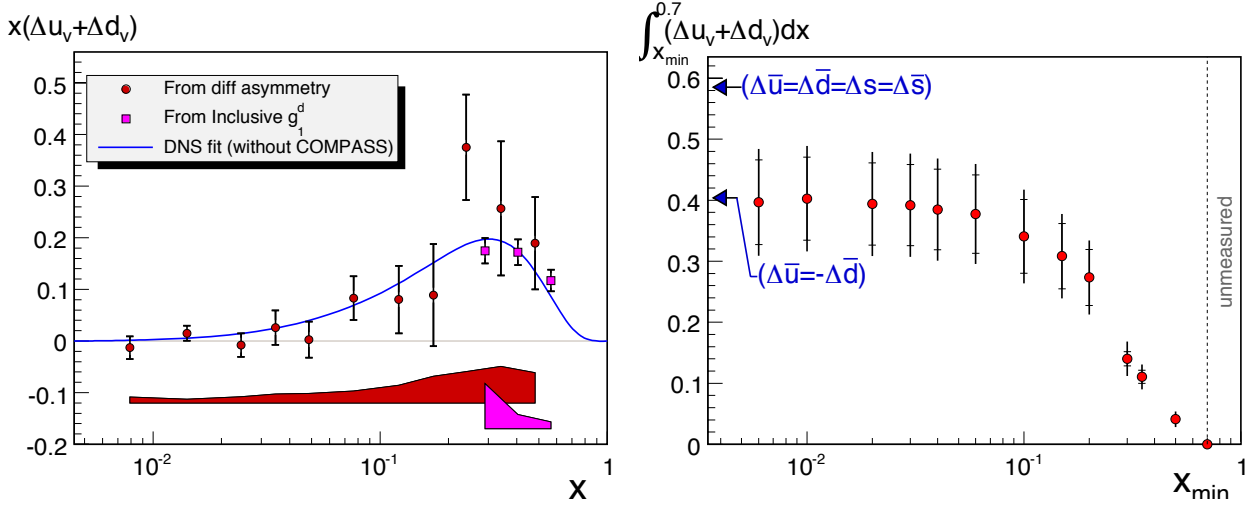


Figure 3.4: The valence quark polarization  $x(\Delta u_v + \Delta d_v)$  compared with that from inclusive  $g_1^d$  data, and the running- $x_{min}$  integral of  $\Delta u_v + \Delta d_v$  from the deuteron data of COMPASS [?] at  $Q^2 = 10$  GeV $^2$ .

### 3.7.4 Spin observables to check the leading order naive $x$ - $z$ separation

A schematic strategy of to test leading order naive  $x$ - $z$  separation was suggested [?] which requires prior knowledge of neither fragmentation functions nor parton distributions. The experimental observables in this strategy is to make the combined double-spin asymmetry  $A_{1N}^{\pi^+ + \pi^-}$ . If leading order naive  $x$ - $z$  separation holds perfectly,  $A_{1N}^{\pi^+ + \pi^-}$  will turn out to be identical to the inclusive  $A_{1N}$  asymmetry due to the exact cancellation of the fragmentation functions in the asymmetry under charge conjugation invariance and isospin symmetry. Their difference,  $A_{1N}^{\pi^+ + \pi^-} - A_{1N}$ , gives a clear indication on the size of the next-to-leading-order terms which violate the naive leading order  $x$ - $z$  separation.

Assume  $\Delta s = \Delta \bar{s} \approx 0$ , the fragmentation functions are canceled at the leading order in the combined asymmetry  $A_{1N}^{\pi^+ + \pi^-}$ , such that:

$$\begin{aligned} A_{1p}^{\pi^+ + \pi^-}(x, Q^2, z) &= \frac{\Delta\sigma_p^{\pi^+} + \Delta\sigma_p^{\pi^-}}{\sigma_p^{\pi^+} + \sigma_p^{\pi^-}} = \frac{4(\Delta u + \Delta \bar{u}) + \Delta d + \Delta \bar{d}}{4(u + \bar{u}) + d + \bar{d}} \equiv A_{1p}(x, Q^2), \\ A_{1d}^{\pi^+ + \pi^-}(x, Q^2, z) &= \frac{\Delta\sigma_d^{\pi^+} + \Delta\sigma_d^{\pi^-}}{\sigma_d^{\pi^+} + \sigma_d^{\pi^-}} = \frac{\Delta u + \Delta d + \Delta \bar{u} + \Delta \bar{d}}{u + d + \bar{u} + \bar{d}} \equiv A_{1d}(x, Q^2), \\ A_{1n}^{\pi^+ + \pi^-}(x, Q^2, z) &= \frac{\Delta\sigma_n^{\pi^+} + \Delta\sigma_n^{\pi^-}}{\sigma_n^{\pi^+} + \sigma_n^{\pi^-}} = \frac{\Delta u + \Delta \bar{u} + 4(\Delta d + \Delta \bar{d})}{u + \bar{u} + 4(d + \bar{d})} \equiv A_{1n}(x, Q^2). \end{aligned} \quad (3.27)$$

The combined asymmetry  $A_{1N}^{\pi^+ + \pi^-}$  reduces to the inclusive asymmetry  $A_{1N}$  under the leading order naive  $x$ - $z$  separation. The relation  $A_{1N}^{\pi^+ + \pi^-}(x, Q^2, z) = A_{1N}(x, Q^2)$  is a rather strong condition to satisfy, since the left-hand side involves the hadron observable  $z$  while the right-hand side doesn't. The deviation of  $A_{1N}^{\pi^+ + \pi^-}$  from the inclusive  $A_{1N}$  asymmetry “effectively” measures the relative importance of the contribution from the next-to-leading order terms.

The HERMES experiment extracted the combined asymmetry  $A_{1N}^{h+\bar{h}}$  as shown in Fig. ?? in comparison with the inclusive asymmetry  $A_{1N}$ . The near perfect agreement of  $A_{1N}^{h+\bar{h}}$  with  $A_{1N}$

at  $\langle Q^2 \rangle = 2.5$  GeV $^2$  indicated that the next-to-leading order correction terms are small or mostly canceled in the asymmetries and the target fragmentation contribution has a negligible impact to the asymmetries. Even better agreements should be expected in this experiment at JLab-12GeV, since the much higher luminosity allow reasonable statistics at larger scattering angle resulted in  $\langle Q^2 \rangle = 4.0$  GeV $^2$  for this experiment. Once this agreement can be clearly demonstrated with high precision, parton polarizations can be reliably extracted through the leading order interpretation of SIDIS asymmetries.

# Chapter 4

## The Experiment

### 4.1 Summary of Requested Beam Time Allocations

An experiment is proposed to measure the longitudinal virtual photon asymmetries  $A_{1n}^h$  in the SIDIS reaction on a longitudinally polarized  ${}^3\text{He}$  target. The experiment will use a high-luminosity polarized  ${}^3\text{He}$  target currently under development for several approved experiments, together with the BigBite [22, 23, 24] and Super BigBite [25, 26] spectrometers in Hall A. There are essentially five adjustable parameters of the experiment; the beam energy  $E_{beam}$ , the two spectrometer angles  $\theta_{BB}$  and  $\theta_{SBS}$ , and the target-magnet yoke distances  $d_{BB}$  and  $d_{SBS}$ . Table 4.1 shows the requested

Table 4.1: Requested beam time allocations. In total, 30 beam-days of production on  ${}^3\text{He}$  and 3 beam-days for configuration changes and calibration measurements are requested. Production data collection is divided between beam energies of 11 GeV (20 days) and 8.8 GeV (10 days). At each beam energy, the beam time is divided equally between two SBS angle settings of 14 and 10 degrees. Calibrations include measurements on unpolarized  ${}^3\text{He}$ ,  $\text{N}_2$ ,  $\text{H}_2$  and empty reference cells for dilutions and multi-foil solid targets for spectrometer optics calibrations.  $E_{beam}$  is the beam energy,  $\theta_{BB/SBS}$  is the spectrometer central angle and  $d_{BB/SBS}$  is the distance from the center of the target to the front face of the magnet yoke along the spectrometer axis.

Beam days	Purpose	$E_{beam}$ (GeV)	$\theta_{BB}$ (deg.)	$\theta_{SBS}$ (deg.)	$d_{BB}$ (m)	$d_{SBS}$ (m)
10	Production	11	30	14	1.55	2.5
10	Production	11	30	10	1.55	2.6
5	Production	8.8	30	14	1.55	2.5
5	Production	8.8	30	10	1.55	2.6
1	Calibration	11	30	14	1.55	2.5
1	Calibration	11	30	10	1.55	2.6
0.5	Calibration	8.8	30	14	1.55	2.5
0.5	Calibration	8.8	30	10	1.55	2.6
30	Total production					
3	Total calibrations					

beam allocations in each experiment configuration. The configuration of the spectrometers in

the proposed experiment is identical to that of the approved experiment E12-09-018 [27] in most respects. The main differences between the proposed experiment and E12-09-018 are:

- This proposal uses a longitudinally polarized  ${}^3\text{He}$  target, whereas E12-09-018 will measure asymmetries on a transversely polarized target.
- The proposed experiment also includes data taking at a smaller SBS central angle of  $10^\circ$  to focus the hadron arm acceptance at smaller values of  $p_T^h$ , where the  $\phi_h$  coverage is more complete and SIDIS cross sections are larger.

The double-spin asymmetries will be extracted with high statistical precision in a dense two-dimensional grid of  $(x, z)$  for  $\pi^{\pm,0}$  and  $K^\pm$ , with  $0.1 \leq x \leq 0.7$  and  $0.2 \leq z \leq 0.8$ . The data from two different SBS central angles will also provide a wide coverage in  $p_T^h$  and  $\phi_h$  at the same  $x$  and  $z$ . Data at two different beam energies provide significantly different  $Q^2$  values at the same  $x$ , leading to a “fully differential” mapping of the SIDIS asymmetries. However, since the main physics goal of this proposal is to provide data of high statistical precision for the flavor decomposition of the nucleon’s longitudinal spin structure in the collinear approximation, the two-dimensional  $(x, z)$  kinematic binning is emphasized in the discussion of expected results presented here.

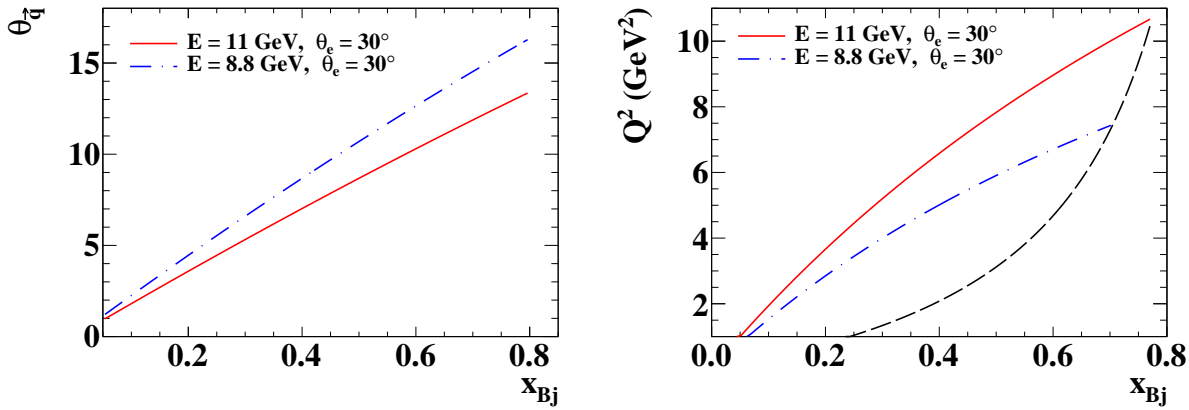


Figure 4.1: Left: Angle of the momentum transfer  $\vec{q}$  relative to the beam direction vs  $x$  for an electron scattering angle  $\theta_e = 30^\circ$  and beam energies of 11 and 8.8 GeV. Right:  $Q^2$  vs  $x$  at  $\theta_e = 30^\circ$  for 11 and 8.8 GeV. The black dashed curve shows the  $W > 2 \text{ GeV}$  cutoff.

The motivation for taking roughly half the data at a smaller SBS central angle derives from the differences in physics goals between this proposal and E12-09-018. Figure 4.1 shows the direction of the momentum transfer  $\vec{q}$  as a function of  $x$  at the central electron scattering angle of 30 degrees. In the absence of competing constraints, the optimal hadron arm angle coincides with the virtual photon direction  $\theta_{\vec{q}}$ . Since  $\theta_{\vec{q}}$  varies as a function of  $x$ , the hadron arm acceptance can only be centered along  $\vec{q}$  for a particular value of  $x$ . The transverse target single-spin asymmetries that will be measured by E12-09-018 vanish as  $p_T^h \rightarrow 0$ , such that the optimal SBS central angle for the study of transversity is that which centers the SIDIS kinematic coverage at moderate, non-zero  $p_T^h$ . On the other hand, the longitudinal double-spin asymmetries used as input to the extraction of flavor-separated quark helicity distributions  $\Delta q$  do not vanish as  $p_T^h \rightarrow 0$ , so the optimal central angle of the hadron arm in this experiment is that which maximizes the SIDIS event rate for the  $x - Q^2$  range covered by the electron arm. The ability to move to smaller SBS central angles is limited by the spatial constraints of the BigBite and SBS magnet and detector geometries and the

downstream beam pipe in Hall A; for a fixed position of BigBite, the minimum target-SBS magnet distance increases as the SBS central angle is reduced. Moreover, the detector background rates increase at smaller angles. The data obtained at two different SBS central angles will result in an overall increase in  $\phi_h$  and  $p_T^h$  coverage and a significant increase in total statistics at lower  $x$  and  $p_T^h$  values.

## 4.2 Experiment Apparatus

In the proposed experiment, longitudinally polarized electron beams from CEBAF with energies of 11 and 8.8 GeV will collide with longitudinally polarized  ${}^3\text{He}$  nuclei in a 60 cm-long target. A beam polarization of 85% is assumed throughout this proposal. This value for electron beam polarization has been routinely achieved and exceeded during the 6 GeV era of CEBAF operations. The beam current will be 40  $\mu\text{A}$  on the 60-cm target at a pressure of 10.5 atm, leading to an effective electron-polarized-neutron luminosity of approximately  $4 \times 10^{36} \text{ cm}^{-2} \text{ s}^{-1}$ . Figure 4.2 shows the basic layout

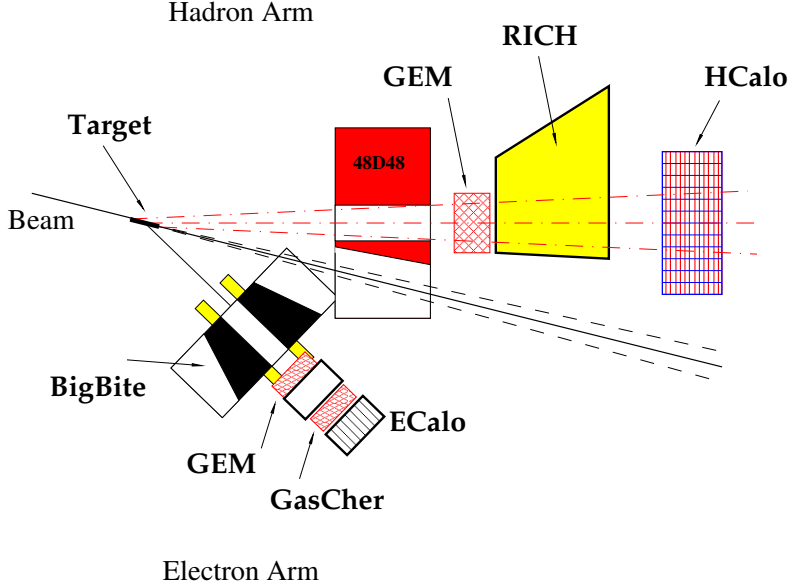


Figure 4.2: Schematic layout of the proposed measurements. The BigBite Spectrometer detects DIS electrons at a central angle of  $30^\circ$  on the beam right, while the Super BigBite Spectrometer detects SIDIS hadrons on the beam left in the vicinity of the momentum transfer direction at central angles of  $14^\circ$  and  $10^\circ$ .

of the experiment. BigBite will detect DIS electrons with momenta  $p_e \geq 1 \text{ GeV}$  at a central angle of  $30^\circ$  on the beam right. Super BigBite (SBS) will detect SIDIS hadrons including  $\pi^\pm$ ,  $\pi^0$  and  $K^\pm$  on the beam left, with data taking equally divided between central angles of  $14^\circ$  and  $10^\circ$ . The trigger threshold of the SBS hadronic calorimeter (HCAL) will be set for the efficient detection of hadrons with momentum  $P_h \geq 2 \text{ GeV}$ .

The detector package of SBS will be oriented vertically behind the SBS magnet in the proposed experiment, such that the acceptances for positive and negative charged hadrons are symmetric and identical to a very good approximation. Moreover, the polarity of the SBS magnetic field will be periodically reversed, such that approximately half the data will be collected in up-bending

and down-bending configurations for both positive and negative hadrons; the SBS polarity reversals will cancel the effects of any residual differences in acceptance/efficiency between positive and negative hadrons, which will drastically reduce the systematic uncertainties in the charge-sum and charge-difference asymmetries. Reversing the SBS magnet polarity also increases the  $\phi_h$  acceptance by roughly 14%, and the  $\phi_h$  acceptance of the combination of upbending and downbending configurations is also symmetric about  $\phi_h = 0$ .

#### 4.2.1 High-Luminosity Polarized $^3\text{He}$ Target

The operation of polarized  $^3\text{He}$  targets at substantially higher luminosities than in previous experiments has been made possible by the recent development of targets using convection to more rapidly recirculate the  $^3\text{He}$  gas from the optical pumping chamber in which it is polarized to the target cell in which it is exposed to the beam [28]. The  $^3\text{He}$  target in the proposed experiment has the same basic operating parameters as the target to be used in E12-09-018 [27] and another approved SBS experiment E12-09-016 [29] that will measure the neutron electromagnetic form factor ratio  $G_E^n/G_M^n$  up to  $Q^2 \sim 10 \text{ GeV}^2$ . The target will be 60 cm thick along the beam direction at a pressure of 10.5 atm. The use of thin metal end windows to reduce backgrounds will allow an increase in the useful luminosity by a factor of 3-4 while only increasing the total luminosity by roughly a factor of 2 compared to representative experiments from the 6 GeV era, such as the E06-010 experiment [30]. The target in the proposed experiment differs from the other two SBS  $^3\text{He}$  experiments only in the orientation of the target polarization, which will be along the beam direction in this experiment. An in-beam  $^3\text{He}$  polarization of 60% is assumed throughout this proposal in the calculation of projected asymmetry uncertainties.

#### 4.2.2 BigBite Spectrometer

BigBite is a non-focusing magnetic spectrometer consisting of a vertical-bend dipole magnet with a maximum field-integral of approximately 1.0 T·m that can be instrumented with a flexible configuration of detectors. At its maximum field setting, the BigBite dipole bends the trajectory of a 1.5 GeV particle of charge  $e$  by approximately 10 degrees, providing for moderate momentum resolution of approximately 1% for charged-particle momenta up to several GeV. The BigBite spectrometer was first used at the NIKHEF facility [23, 22] and was later installed in Hall A at Jefferson Lab, where it has been successfully used in several different experiments, including but not limited to the measurement of the neutron electric form factor  $G_E^n$  up to  $Q^2 = 3.4 \text{ GeV}^2$  [31], SIDIS on a transversely polarized  $^3\text{He}$  target [30] and many other experiments that have completed data taking. In the  $G_E^n$  and SIDIS experiments, BigBite was used as the electron spectrometer in coincidence with a hadron detector on the opposite side of the beamline. Following the 12 GeV upgrade, BigBite will be used in this role again in several approved experiments, including E12-09-016 [29] and E12-09-018 [27].

In order to tolerate the higher luminosities of planned experiments at 11 GeV, and to realize the improvements in tracking resolution needed to preserve the  $\sim 1\%$  momentum resolution of BigBite for higher-momentum particles at the same field integral, the BigBite drift chambers will be replaced with Gas Electron Multiplier (GEM) trackers [32, 33], which have been shown to have stable gain at charged-particle rates of up to 1 MHz/mm<sup>2</sup>. A large number of GEM chambers are currently being produced at UVA and INFN for E12-07-109 [34], a measurement of the proton electromagnetic form factor ratio  $G_E^p/G_M^p$  to  $Q^2 = 12 \text{ GeV}^2$ . The GEMs are modular in design, with an active area of up to  $50 \times 60 \text{ cm}^2$ , and will be available to other experiments in Hall A when E12-07-109, which does not use BigBite, is not running. These GEM modules will be used to

assemble a GEM tracker with three tracking planes for Bigbite. Each of the first two GEM planes will have an active area of  $40\text{ cm} \times 150\text{ cm}^2$  from the combination of three  $40 \times 50\text{ cm}^2$  modules. Four  $50 \times 60\text{ cm}^2$  GEM modules will be assembled to form the third tracking plane with an active area of  $60 \times 200\text{ cm}^2$ .

Another planned upgrade to the BigBite detector package for experiments at 11 GeV is a highly-segmented gas Cherenkov detector currently under construction at the College of William and Mary, which will improve electron identification in BigBite compared to 6 GeV experiments that primarily used the lead-glass calorimeter for this purpose.

#### 4.2.3 Super BigBite Spectrometer

The Super BigBite Spectrometer (SBS) [25, 26] is a device conceptually similar to BigBite. The SBS will use a “48D48” magnet acquired by JLab from BNL as a magnetic spectrometer, operated at a field integral of roughly  $1.8\text{ T}\cdot\text{m}$ . The SBS will be capable of reaching forward scattering angles by means of a cut in the magnet yoke for passage of the beam pipe. In E12-07-109, which was proposed to run at luminosities approaching  $10^{39}\text{ cm}^{-2}\text{s}^{-1}$ , the SBS will be instrumented with a proton polarimeter constructed from GEM trackers and  $\text{CH}_2$  analyzers, and a hadronic calorimeter for triggering on high-momentum protons. A significant challenge in the use of open-geometry spectrometers such as BigBite and SBS is the implementation of a trigger that is selective enough to reduce the data acquisition (DAQ) rate to a manageable level while maintaining high efficiency for the events of interest. The BigBite and SBS designs achieve this by exploiting the exponential decrease of the trigger rate as a function of the energy threshold in total-absorption calorimeters. Manageable trigger rates are achieved using a calorimeter-based coincidence trigger between two independent spectrometer arms, each with as high a threshold as the experiment physics goals and detector performance will allow.

All of the SBS experiments will make use of a hadronic calorimeter currently under construction at Carnegie Mellon University. The design of the calorimeter is very similar to that of the “HCAL1” detector used by the COMPASS experiment [35], but with several improvements needed to meet the performance specifications of the SBS experiments. The calorimeter consists of a  $12 \times 24$  array of modules, each consisting of a stack of 40 alternating layers of 20 mm-thick iron and 5 mm-thick scintillator, with a frontal area of  $15 \times 15\text{ cm}^2$ . The design goals for HCAL include a high ( $\gtrsim 95\%$ ) trigger efficiency for protons with momenta from roughly 3-8 GeV at a threshold of 25% of the average signal, a timing resolution of 1 ns or less, and a coordinate resolution better than 5 cm. To meet these requirements, the SBS HCAL will use fast scintillator and wavelength shifter materials and a novel light guide to collect the scintillation light onto two-inch-diameter PMTs with faster response time and higher quantum efficiency than those used by the COMPASS experiment. In E12-09-018 and in the proposed experiment, the SBS HCAL will be used as a charged hadron trigger and will also detect  $\pi^0$ s. A Monte Carlo evaluation of the  $\pi^0$  acceptance and reconstruction efficiency in the SBS showed that the  $\pi^0$  statistics will be similar to those of charged kaons.

Two different types of GEM trackers are being constructed for the SBS experiments. The SBS front tracker GEMs, currently under construction at INFN, consist of six tracker planes, each consisting of three  $40 \times 50\text{ cm}^2$  GEM modules, arranged vertically for a total area per plane of  $40 \times 150\text{ cm}^2$ . In the  $G_E^p$  experiment, the front tracker is used to measure the kinematics of the scattered proton in elastic  $ep$  scattering and to define the incident proton trajectory before the polarization-analyzing scattering in  $\text{CH}_2$ . The front tracker GEMs are subject to the most stringent performance requirements because they are in direct view of the target at a luminosity of  $\sim 8 \times 10^{38}\text{ cm}^{-2}\text{s}^{-1}$ , and experience soft-photon-induced background hit rates of roughly  $400\text{ kHz/cm}^2$  [26]. To realize efficient track reconstruction capability with low false-positives in this

environment, a spatial resolution of  $70 \mu\text{m}$  is required. To realize this spatial resolution, a readout strip pitch of 0.4 mm in both directions is used, leading to a total of about 60,000 readout channels for the entire front tracker.

The SBS polarimeter GEMs, currently under construction at UVA, are subject to different and less stringent performance requirements. These GEMs are used to track protons scattered in  $\text{CH}_2$  analyzers. They are shielded from the target by the  $\text{CH}_2$  analyzers and therefore have lower background rates than the front trackers. On the other hand, a larger area is needed for the polarimeter GEMs in order to provide complete azimuthal acceptance for protons scattered by up to 10 degrees in the  $\text{CH}_2$ . A total of 40 GEM modules of area  $50 \times 60 \text{ cm}^2$  will be produced. These modules will be arranged into two trackers, each consisting of five planes of area  $60 \times 200 \text{ cm}^2$ . The first polarimeter tracker will be located between the two  $\text{CH}_2$  analyzers, while the second will be located between the second  $\text{CH}_2$  analyzer and HCAL. In E12-09-018 and in the proposed experiment, GEM-based trackers for BigBite and SBS will be assembled from a combination of the front tracker and polarimeter GEM modules. The SBS GEM tracker for these experiments will consist of five tracking planes of area  $60 \times 200 \text{ cm}^2$  with four  $50 \times 60 \text{ cm}^2$  polarimeter GEM modules forming each layer. As mentioned in the previous section, the Bigbite GEM tracker will consist of two planes of the INFN GEM modules and one plane of polarimeter GEM modules. Because the luminosity in E12-09-018 and the proposed experiment is a factor of 40 lower than E12-07-109, the background environment in SBS is much more forgiving, such that a large-area tracker assembled from polarimeter GEM modules will have sufficient tracking performance and resolution.

The production of GEM modules is well underway at both INFN and UVa. By now the INFN group has completed the construction of five  $40 \times 50 \text{ cm}^2$  GEM modules while the UVa group has built four  $50 \times 60 \text{ cm}^2$  polarimeter GEM modules. The work on all GEM modules and the readout electronics is expected to be completed by 2016. The testing of the already constructed GEM modules has indicated that they meet all SBS design requirements. Fig 4.3 shows two of the polarimeter GEM modules being tested at the Fermilab test beam facility. Fig 4.4 shows the x and y position resolutions achieved during this beam test.

The readout electronics for all GEM modules is currently being fabricated as part of the SBS program. This readout is based on the APV25 chip, an analog chip developed by Imperial College London for CMS silicon trackers and adopted by several experiments like COMPASS trackers at CERN, STAR Forward GEM Tracker at BNL and others. The APV25 chip samples 128 channels in parallel at 20 MHz or 40 MHz and stores 192 analog samples. Following a trigger, up to 30 consecutive samples from the buffer are read-out and transmitted to an ADC unit that demultiplexes the data from the 128 channels and digitizes the analog information. Both INFN and UVa groups have already assembled and tested large scale APV25 based prototype GEM readout systems.

#### 4.2.4 Ring-Imaging Cherenkov detector for SBS

The designs of SBS and BigBite lend themselves naturally to the study of SIDIS at high  $x$  and  $Q^2$ . To make the SBS a viable hadron spectrometer for SIDIS requires a robust particle identification (PID) capability. The dual-radiator Ring-Imaging Cherenkov (RICH) detector from the HERMES experiment [36], which became available following the end of the HERMES experiment, was quickly recognized as an excellent low-cost solution for PID in the SBS. The HERMES RICH detector uses aerogel with a refractive index  $n = 1.0304$  and  $\text{C}_4\text{F}_{10}$  gas with  $n = 1.00137$  to provide redundant separation of pions, kaons and protons for momenta ranging from the kaon aerogel Cherenkov threshold of 2 GeV up to a limit of 15 GeV determined by the resolution of the reconstructed emission angle in the gas radiator. Cherenkov photons emitted by above-threshold charged hadrons

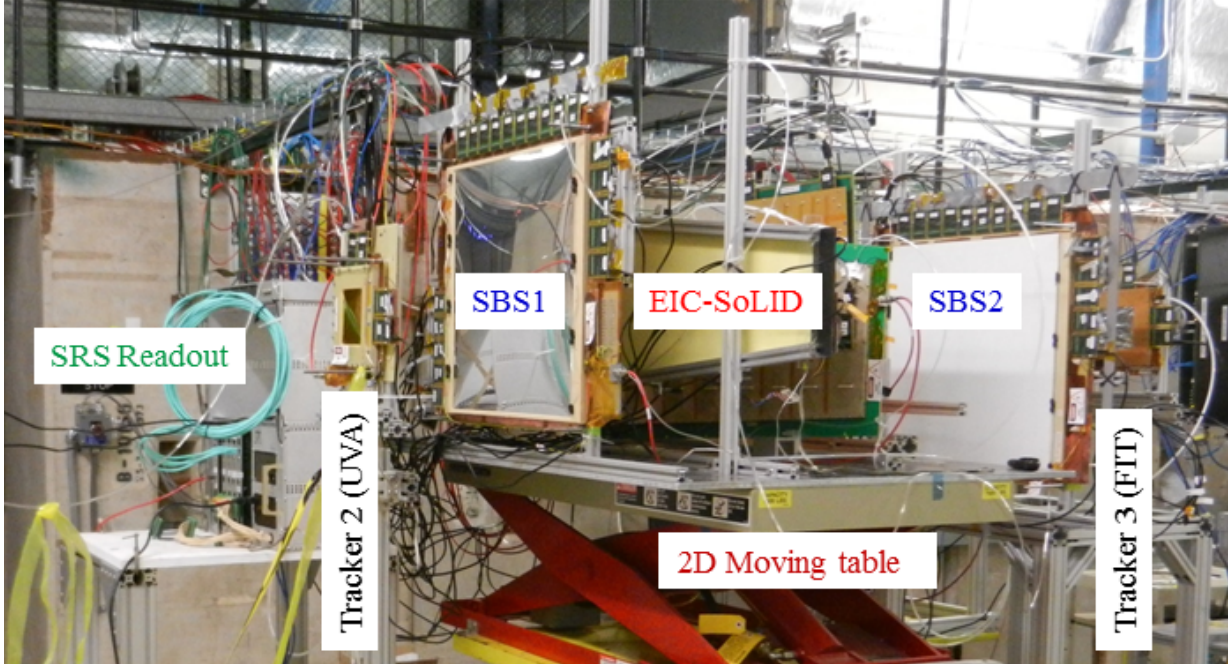


Figure 4.3: Two of the SBS polarimeter GEM modules constructed at UVa during a beam test at Fermilab with several other GEM chambers.

in the aerogel and gas radiators are collected by a large-area spherical mirror with a radius of curvature of 2.2 m onto an array of 1,934 3/4"-diameter photomultiplier tubes (PMTs). The HERMES RICH consists of two identical detector halves on opposite sides of the HERA beam pipe in the HERMES spectrometer. One of the detector halves has been preserved and transferred to JLab for use in SBS, as well as the aerogel wall from the second half. Fig. 4.5 shows the basic design and working principle of the RICH. The aerogel wall consists of an array of 5 rows  $\times$  17 columns of aerogel tiles stacked 5 tiles deep. The average tile dimensions are  $(11.4 \times 11.4 \times 1.13)$  cm<sup>3</sup>.

Detailed Monte Carlo simulations of the HERMES RICH in SBS were carried out to determine the background rates in the PMTs and the useful acceptance of the RICH; i.e., the range of particle trajectories for which adequate PID performance is expected. Fig. 4.6 shows the layout of the RICH in the SBS Monte Carlo simulation using the GEANT4 toolkit [37], and examples of the Cherenkov light emitted by a pion and a kaon with identical trajectories. The simulation includes details of BigBite, the SBS magnet, the <sup>3</sup>He target, the GEM tracker, the RICH, HCAL, and the materials along the beamline. Preliminary background rate calculations for the PAC38 proposal for E12-09-018 [27] indicated an average PMT occupancy<sup>1</sup> of 0.1%, assuming the RICH PMT signals can be correlated in time with the signals from the other detectors to within  $\pm 5$  ns. Such an occupancy leads to very high signal/noise ratios for the PID analysis. To achieve such a small effective timing window requires the implementation of a TDC readout for the RICH PMTs in SBS, a feature which was absent from the HERMES setup because the beam repetition rate at HERA was such that the smallest useful time window for detector readout was 100 ns.

Fig. 4.7 shows preliminary PID results from the SBS RICH Monte Carlo simulation. The PID performance is characterized by the probability  $P_{ij}$  of assigning particle hypothesis  $j$  to a track with

<sup>1</sup>“Occupancy” is defined as the probability of an accidental background hit within the timing window of an event.

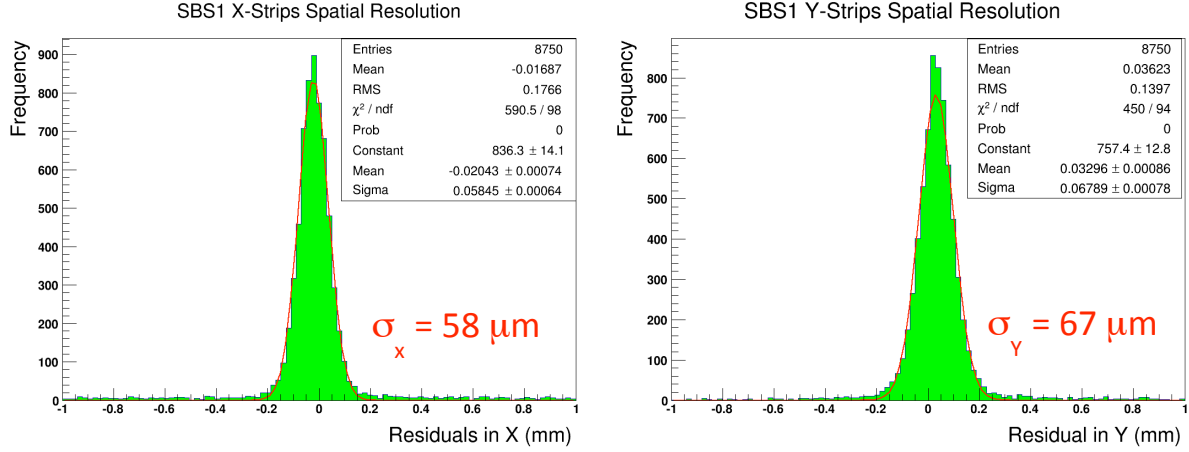


Figure 4.4: The x and y position resolutions achieved with the SBS GEM modules.

known true particle type  $i$  and reconstructed<sup>2</sup> momentum  $p$ . The PID assignment is made based on a simplified version of the inverse ray tracing algorithm described in [36]. The only requirement imposed on the selection of MC events for the PID analysis is the presence of a track, so that the misidentification probabilities shown include the effects of acceptance mismatch (i.e., those events which have small or non-existent signals because of a failure to produce and/or collect sufficient Cherenkov light). These preliminary results already demonstrate that the efficiency and purity of the PID analysis are high across the entire momentum range of interest, and that the geometry of the RICH does not significantly reduce the SBS acceptance relative to the combined acceptance of the SBS magnet and GEM tracker. Of particular importance is the low ( $\lesssim 1\%$ ) probability to misidentify pions as kaons above the pion gas threshold of  $\sim 2.7$  GeV, since the expected flux of pions is about ten times that of kaons in E12-09-018 and in the proposed experiment.

## 4.3 Experiment Plan and Expected Results

### 4.3.1 Monte Carlo Simulation

Figure 4.8 shows the GEANT4 model of the proposed experiment in each of the two proposed SBS angle settings. The simulation includes the detailed geometries and field layouts of both magnets, the essential features of the  ${}^3\text{He}$  target and the Hall A beamline, and realistic models of the detectors, which include the GEM tracker, the RICH and the HCAL for the hadron arm, and a GEM-based tracker, gas Cherenkov counter and electromagnetic calorimeter for the electron arm. SIDIS events were generated separately for each hadron species and propagated through the GEANT4 model. For all events, a good electron track in BigBite and above-threshold energy deposition in the BigBite calorimeter were required. For charged hadrons, a good track in SBS and above-threshold energy deposition in HCAL were required. The preliminary Monte Carlo studies of the RICH PID performance in SBS (see Fig. 4.7) already show that the acceptance of the RICH does not significantly reduce the useful acceptance of SBS for high-performance PID, relative to the acceptance defined by the magnet gap and the tracker area. Therefore, because the GEANT4 simulation of Cherenkov radiation in the SBS RICH is computationally expensive, the RICH was

<sup>2</sup>The momentum resolution of SBS is  $\sigma_p/p \approx 1\%$ .

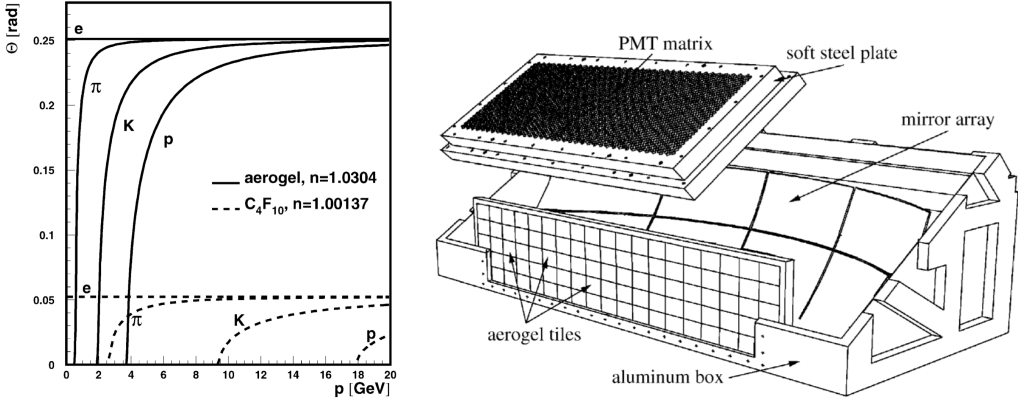


Figure 4.5: Left: Cherenkov emission angle  $\theta$  as a function of particle momentum  $p$  for the dual-radiator HERMES RICH counter. Right: layout of the major components of the RICH. Figures reproduced from [36].

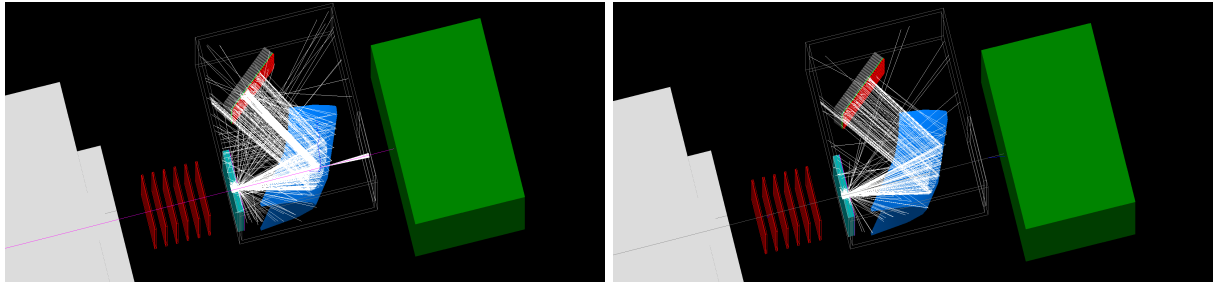


Figure 4.6: Layout of the HERMES RICH in the Monte Carlo simulation of E12-09-018. Left: A pion with a momentum of 5 GeV emits Cherenkov radiation in aerogel and gas. Right: A kaon moving along the same trajectory at the same momentum only produces Cherenkov light in aerogel at smaller emission angles. The spherical mirror collects the light onto the PMT matrix.

not included in the analysis for rate estimates and asymmetry uncertainty projections. For  $\pi^0$  events, both  $\pi^0$  decay photons were required in HCAL with a minimum separation of one pixel. The following global cuts were applied to the “true” (nucleon rest frame) kinematics of generated SIDIS events:

- $Q^2 \geq 1 \text{ GeV}^2$ : Standard DIS cut.
- $W \geq 2 \text{ GeV}$ : Standard DIS cut to avoid the nucleon resonance region.
- $M_X \geq 1.5 \text{ GeV}$ : Large missing-mass cut to avoid the exclusive and resonance regions of  $n(e, e'h)X$ .
- $P_h \geq 2 \text{ GeV}$ : Minimum hadron momentum to minimize effects of nuclear final-state-interactions and target fragmentation.
- $y \leq 0.9$ : Maximum fractional electron energy loss to avoid large QED radiative corrections, as well as large pair-production backgrounds present at low electron energies.

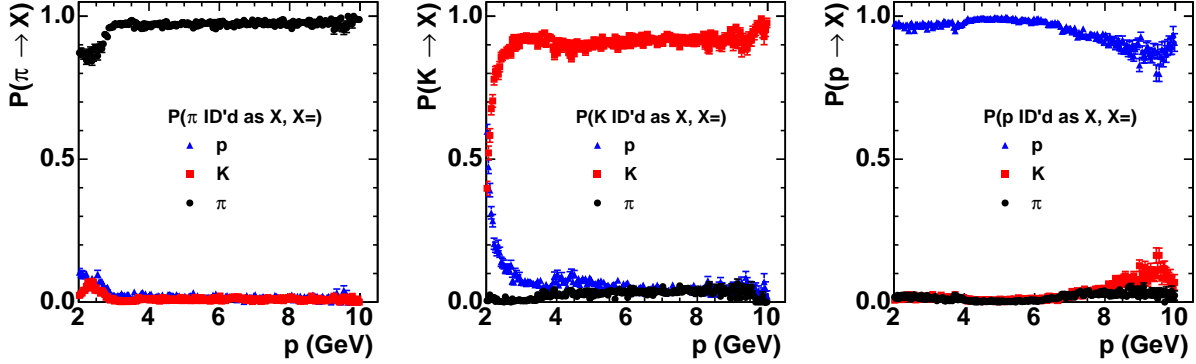


Figure 4.7: PID results from SBS Monte Carlo simulation. Particle ID probabilities as a function of momentum for pions (left), kaons (center) and protons (right). Results are preliminary and can be improved via further optimization of the PID algorithm.

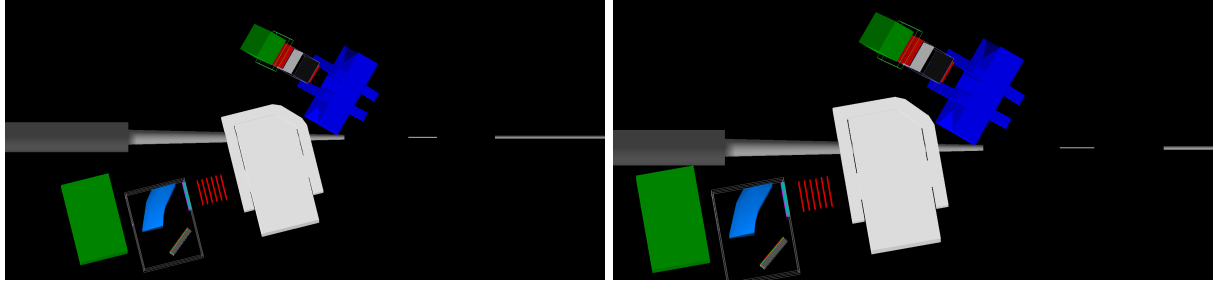


Figure 4.8: GEANT4 Monte Carlo model of the proposed experiment. Left: with SBS at a central angle of  $14^\circ$  at a distance of 2.5 meters, identical to approved experiment E12-09-018. Right: with SBS at a central angle of  $10^\circ$  at a distance of 2.6 meters.

- $P_e \geq 1$  GeV: “Trigger threshold” for BigBite; redundant with  $y$  cut.

### 4.3.2 SIDIS Cross Section Model

For the purpose of rate estimation for this proposal, the unpolarized SIDIS cross section was calculated using a naive, leading-order, leading-twist approximation with the CTEQ6 PDFs [38] and the DSS2007 fragmentation functions [39] for pions and kaons, neglecting any  $\phi_h$  dependence. The unpolarized differential scattering cross section is given in this simple model by

$$\frac{d\sigma}{dE'_e d\Omega_e dz dp_T^2 d\phi_h} = \frac{4\alpha^2 {E'_e}^2}{Q^4} \left[ \frac{2H_1}{M} \sin^2 \left( \frac{\theta_e}{2} \right) + \frac{H_2}{\nu} \cos^2 \left( \frac{\theta_e}{2} \right) \right], \quad (4.1)$$

where  $E'_e$  is the scattered electron energy,  $M$  is the nucleon mass,  $\theta_e$  is the electron scattering angle,  $\nu$  is the electron energy loss in the target rest frame, and the SIDIS structure function  $H_2$  is given at leading order by

$$H_2(x, Q^2, z, p_T^2) = x \sum_q e_q^2 q(x, Q^2) D_q^h(z, Q^2) \frac{b_q^h}{2\pi} e^{-b_q^h p_T^2}. \quad (4.2)$$

Six light quark flavors  $q = u, d, s, \bar{u}, \bar{d}, \bar{s}$  are included in the sum.  $q(x, Q^2)$  is the unpolarized PDF for quark flavor  $q$  and  $D_h^q(z, Q^2)$  is the unpolarized fragmentation function for quark  $q$  to hadron  $h$ . A factorized Gaussian transverse momentum dependence is assumed, with a flavor-independent average width given by:

$$b_q^h = \frac{1}{z^2 \langle k_\perp^2 \rangle + \langle p_\perp^2 \rangle}, \quad (4.3)$$

where  $\langle k_\perp^2 \rangle$  is the transverse momentum width of the initial quark distribution and  $\langle p_\perp^2 \rangle$  is the width of the transverse momentum distribution of hadrons produced in the fragmentation of the recoiling quark. Constant values  $\langle k_\perp^2 \rangle = 0.25 \text{ GeV}^2$  and  $\langle p_\perp^2 \rangle = 0.20 \text{ GeV}^2$  were assumed, following Ref. [40]. The Callan-Gross relation  $H_2 = 2xH_1$  was assumed for the SIDIS structure functions, implying neglect of the longitudinal virtual photoabsorption cross section. The kinematic coverages and rate estimates shown in the next sections correspond to the simplified SIDIS cross section model of Eqn. (4.1) convoluted with the combined acceptance of the two-spectrometer setup.

SIDIS events on  ${}^3\text{He}$  “smeared” by the Fermi motion of the initial nucleons were generated in the GEANT4 simulation using the following procedure. First, the nucleon participating in the scattering event is chosen randomly; i.e., a neutron (proton) is chosen with probability  $\frac{1}{3}$  ( $\frac{2}{3}$ ). After choosing the initial nucleon, its initial momentum is sampled from the neutron (proton) momentum distribution in  ${}^3\text{He}$  obtained from a fit to the results of a calculation using the Argonne V18 potential, and its initial direction of motion is chosen randomly. The polar ( $\cos \theta_{e/h}$ ) and azimuthal ( $\phi_{e/h}$ ) scattering angles and energies  $E'_{e/h}$  of outgoing particles in the *lab frame* are generated randomly within limits chosen to populate the full solid angle and momentum acceptance of both spectrometers. The initial and final electron and nucleon four-momenta are then boosted to the nucleon rest frame, and the SIDIS cross section is computed using Eqn. (4.1). If the nucleon participating in the scattering is a neutron, the cross section is obtained from that on a proton by interchanging  $u$  and  $d$  quarks. The “true” (nucleon rest frame) SIDIS kinematics are also calculated. Finally, the lab-frame cross section is computed from the nucleon-rest-frame cross section by accounting for the modification of the flux factor by the boost due to the fact that the collision in the lab frame is no longer collinear<sup>3</sup>. The weight of each event is then calculated by multiplying the lab frame differential cross section by the Lorentz-invariant phase space volume of event generation and the integrated luminosity and dividing by the number of generated events. The weight thus defined represents the expected number of experimental counts corresponding to each Monte Carlo event. By keeping track of the identity of the nucleon participating in the collision, the dilution factors relating the  ${}^3\text{He}$  asymmetry to the neutron asymmetry are also determined.

### 4.3.3 SIDIS Kinematic Coverage

Figure 4.9 shows the projected SIDIS  ${}^3\text{He}(e, e'\pi^+)X$  yield as a function of the kinematic variables  $x$ ,  $z$ ,  $p_T^h$  and  $\phi_h$  for each of the four beam energy/SBS angle configurations. The ten-degree setting exhibits higher event rates at low  $x$  and low  $p_T^h$  values and greater  $\phi_h$  coverage than the 14-degree setting. On the other hand, for  $x \gtrsim 0.5$  and  $p_T^h \gtrsim 0.6 \text{ GeV}$ , the yield for the 14-degree setting equals or exceeds that of the 10-degree setting. In both settings, the  $\phi_h$  coverage is peaked near  $\phi_h \approx \pm\pi$ , averages about half of  $2\pi$ , and increases at low  $p_T^h$ /high  $x$  values.

Figure 4.10 shows the coverages of the SIDIS kinematic variables  $Q^2$ ,  $z$ ,  $p_T^h$  and  $\phi_h$  as a function of  $x$  in each of the four proposed energy/angle combinations. The color scale of the plots corresponds

---

<sup>3</sup>The flux factor  $F \propto |\mathbf{v}_e - \mathbf{v}_N|$  is the only part of the cross section which is not Lorentz-invariant, but has the Lorentz transformation properties of a cross-sectional area.

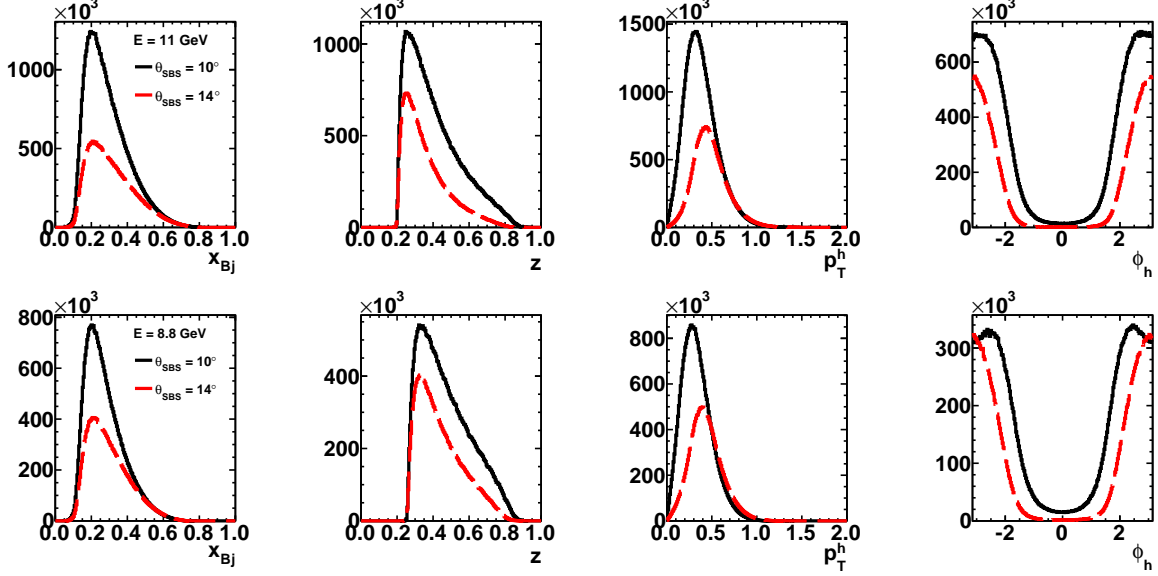


Figure 4.9: Expected distributions of the kinematic variables  $x$ ,  $z$ ,  $p_T^h$  and  $\phi_h$  (from left to right) in  ${}^3\text{He}(e, e'\pi^+)X$ , for  $E = 11$  GeV (top row) and  $E = 8.8$  GeV (bottom row). Black solid (red dashed) lines are for  $\theta_{SBS} = 10^\circ(14^\circ)$ . The histograms are normalized so that the vertical axis corresponds to the total number of  ${}^3\text{He}(e, e'\pi^+)X$  events in the beam time allocated to the configuration in question.

to the expected total number of  ${}^3\text{He}(e, e'\pi^+)X$  events in each bin.  $Q^2$  is strongly correlated with  $x$  as a consequence of the large horizontal/vertical aspect ratio of the BigBite magnet gap. Due to the large momentum acceptance of both spectrometers, the  $z$  and  $x$  acceptances are largely uncorrelated, leading to a wide, independent range of  $x$  and  $z$  within a single angle/beam energy setting. The correlation between the momentum transfer direction and  $x$  leads to a weak negative correlation between  $p_T^h$  and  $x$ . The  $\phi_h$  coverage increases with  $x$  for the same reason. Figure 4.11 shows the average  $\langle Q^2 \rangle$  vs. the average  $\langle x \rangle$  in the proposed experiment at 11 and 8.8 GeV beam energies. By focusing the kinematic coverage for the electron at large scattering angles and running the experiment at high luminosity, the proposed configuration reaches high statistical figure-of-merit at a larger average  $Q^2$  than that of the HERMES experiment, despite the lower beam energy.

#### 4.3.4 Event Rates

Table 4.2 shows the total SIDIS event rates for the five hadron species after applying kinematic cuts to select the SIDIS reaction in the current fragmentation region. Although the  $\pi^0$  production rate is similar to the charged pion production rates<sup>4</sup>, the SBS acceptance for  $\pi^0$ s is further reduced relative to the charged pion acceptance by the requirement that both  $\pi^0$  decay photons are detected with a minimum separation of one pixel.

---

<sup>4</sup>The  $\pi^0$  fragmentation functions are assumed to be averages of  $\pi^+$  and  $\pi^-$  (isospin symmetry assumption).

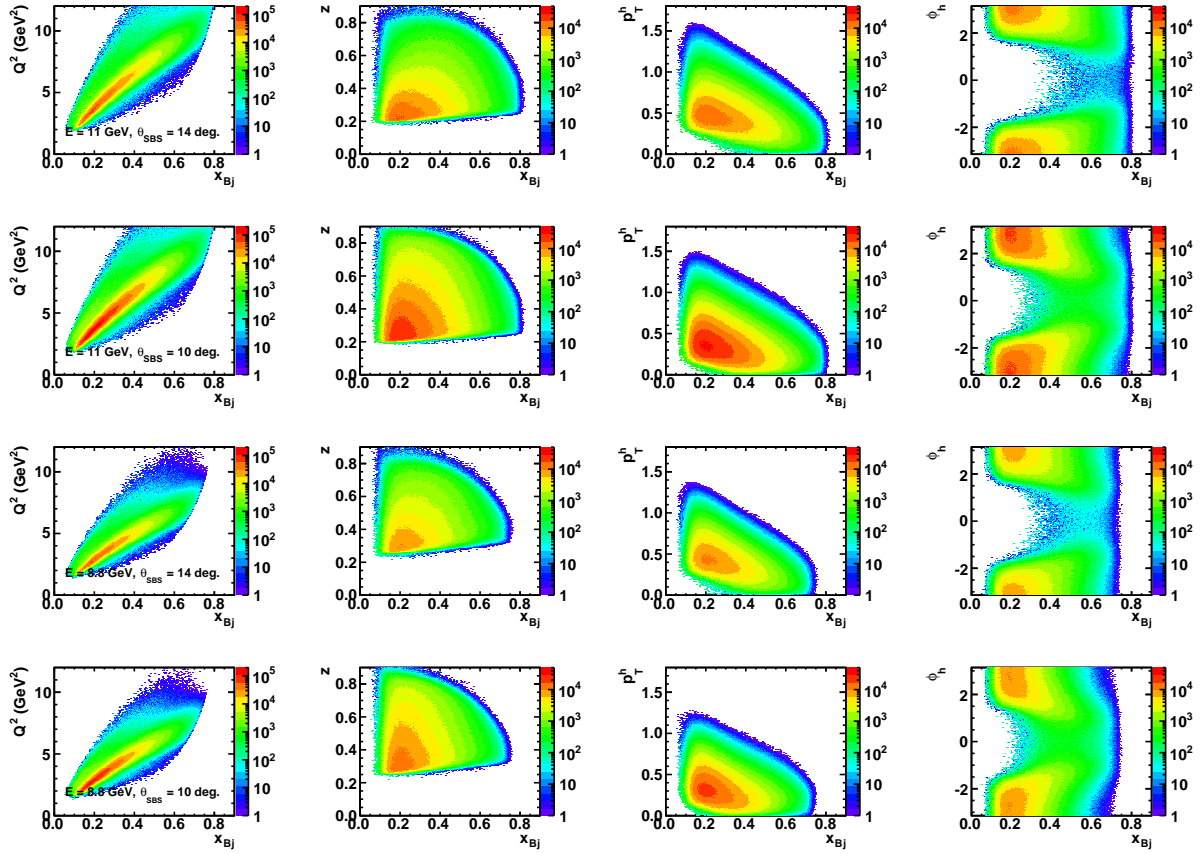


Figure 4.10: SIDIS phase space coverage of the four proposed experiment configurations for the  ${}^3\text{He}(e, e'\pi^+)X$  channel. From left to right:  $Q^2$ ,  $z$ ,  $p_T^h$  and  $\phi_h$  vs  $x$ . From top to bottom:  $E = 11 \text{ GeV}$ ,  $\theta_{SBS} = 14^\circ$ ,  $E = 11 \text{ GeV}$ ,  $\theta_{SBS} = 10^\circ$ ,  $E = 8.8 \text{ GeV}$ ,  $\theta_{SBS} = 14^\circ$ , and  $E = 8.8 \text{ GeV}$ ,  $\theta_{SBS} = 10^\circ$ . Color scale corresponds to the expected total number of events.

#### 4.3.5 Projected Statistical Uncertainties in $A_{1n}^h(x, z)$

The experimentally observed double-spin asymmetry  $A_{LL,h}^{exp}$  for hadron  $h$  on  ${}^3\text{He}$  is related to the longitudinal virtual photon asymmetry by:

$$A_{LL,exp}^h = P_B P_T A_{LL,{}^3\text{He}}^h = P_B P_T \mathcal{P}_{kin} A_{1,{}^3\text{He}}^h \approx P_B P_T \mathcal{P}_{kin} \left[ P_n f_n A_{1n}^h + P_p f_p A_{1p}^h \right], \quad (4.4)$$

where  $P_B$  and  $P_T$  are the beam and target polarizations,  $P_n = 0.86^{+0.036}_{-0.02}$  and  $P_p = -0.028^{+0.009}_{-0.004}$  are the neutron and proton effective polarizations in  ${}^3\text{He}$ ,  $f_{n/p}$  is the “dilution” factor representing the fraction of the total  ${}^3\text{He}$  SIDIS cross section carried by the neutron/protons, and  $\mathcal{P}_{kin}$  is the kinematic factor appearing in Eqn. (3.3). This effective polarization approximation has been used for the extraction of neutron asymmetries from measured  ${}^3\text{He}$  asymmetries by a number of previous experiments studying DIS on polarized  ${}^3\text{He}$  targets [30, 42, 43]. The experimentally observed asymmetry is defined by the asymmetry in the measured SIDIS yield between events obtained with beam and target polarizations parallel and anti-parallel. Defining  $N_+ \equiv N_{++} + N_{--}$  and  $N_- \equiv N_{+-} + N_{-+}$  as the total SIDIS yields in parallel and anti-parallel conditions, respectively,

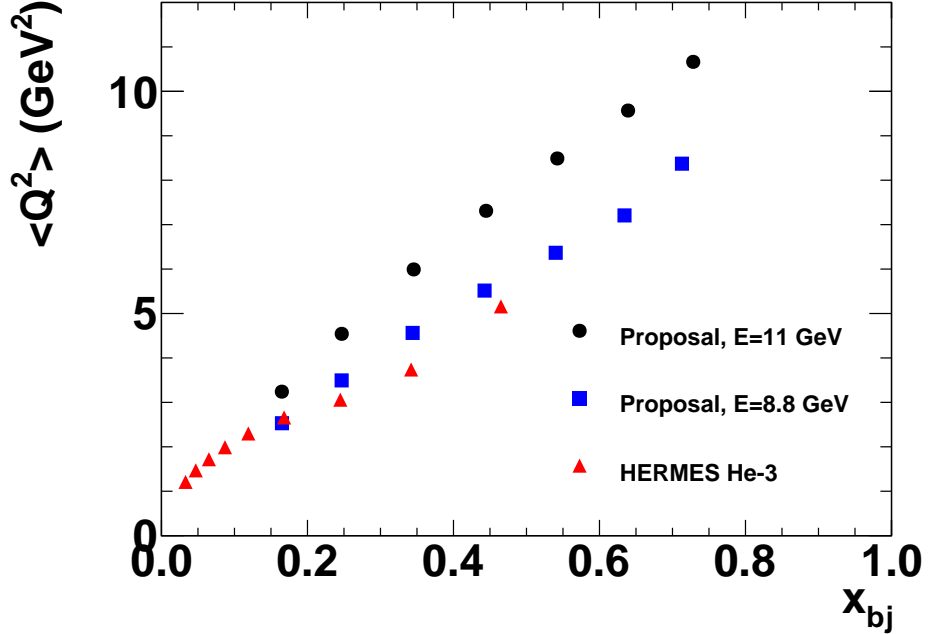


Figure 4.11: Average  $Q^2$  vs average  $x$  in the proposed experiments, compared to the kinematics of existing HERMES data on  ${}^3\text{He}$  [41].

the observed asymmetry is then defined as:

$$A_{LL,exp}^h = \frac{N_- - N_+}{N_+ + N_-} \quad (4.5)$$

The statistical uncertainty in  $A_{LL,h}^{exp}$  is given by

$$\Delta A_{LL,exp}^h = \sqrt{\frac{1 - (A_{LL,exp}^h)^2}{N}}, \quad (4.6)$$

where  $N \equiv N_+ + N_-$  is the total number of events. The projected uncertainty in  $A_{1n}^h$  for each  $(x, z)$  bin was estimated from equations (4.6) and (4.4). For the ratio  $R = \sigma_L/\sigma_T$  that enters the kinematic factor  $\mathcal{P}_{kin}$  of equation (3.3), the SLAC R1998 parametrization of inclusive DIS data was used [44], which implies the assumption, in the absence of data for  $R$  in SIDIS, that  $R_{SIDIS} = R_{DIS}$ . The small  $A_{1p}^h$  correction due to the small but non-zero proton polarization in  ${}^3\text{He}$  was neglected. This correction will be well-constrained by existing data from HERMES as well as from future JLab measurements in CLAS12, and its contribution to the systematic uncertainty in  $A_{1n}^h$  will be small.

For the analysis of projected physics results, Monte-Carlo generated SIDIS events passing all cuts were subdivided into a two-dimensional rectangular grid of  $(x, z)$  bins in the range  $(0.1 \leq x \leq 0.8, 0.2 \leq z \leq 0.8)$  with bin widths of  $(\Delta x, \Delta z) = (0.1, 0.1)$ . In each bin, the total number of events and the weighted-average kinematics  $\langle x \rangle$ ,  $\langle Q^2 \rangle$ ,  $\langle z \rangle$  and  $\langle p_T^h \rangle$  were calculated as well as the kinematic factor  $\langle \mathcal{P}_{kin} \rangle$  and the dilution factor  $f_n$ . The uncertainty  $\Delta A_{1n}^h$  was then calculated in

Table 4.2: Expected total SIDIS  ${}^3He(e, e'h)X$  event rates passing all SIDIS kinematic cuts:  $Q^2 \geq 1$  GeV $^2$ ,  $W \geq 2$  GeV,  $M_X \geq 1.5$  GeV,  $y \leq 0.9$ ,  $P_h \geq 2$  GeV,  $p_e \geq 1$  GeV.

Channel	$E = 11$ GeV	$E = 11$ GeV	$E = 8.8$ GeV	$E = 8.8$ GeV
	$\theta_{SBS} = 14^\circ$	$\theta_{SBS} = 10^\circ$	$\theta_{SBS} = 14^\circ$	$\theta_{SBS} = 10^\circ$
${}^3He(e, e'\pi^+)X$ rate (Hz)	35.8	70.2	47.8	77.8
${}^3He(e, e'\pi^-)X$ rate (Hz)	23.2	44.0	28.6	45.7
${}^3He(e, e'\pi^0)X$ rate (Hz)	3.7	9.5	4.5	9.0
${}^3He(e, e'K^+)X$ rate (Hz)	5.8	12.6	8.7	15.2
${}^3He(e, e'K^-)X$ rate (Hz)	1.1	2.4	1.4	2.4

each bin using

$$\Delta A_{1n}^h = \frac{1}{P_B P_T f_n P_n \mathcal{P}_{kin} \sqrt{N}}, \quad (4.7)$$

where again the small  $A_{1p}^h$  correction has been neglected.

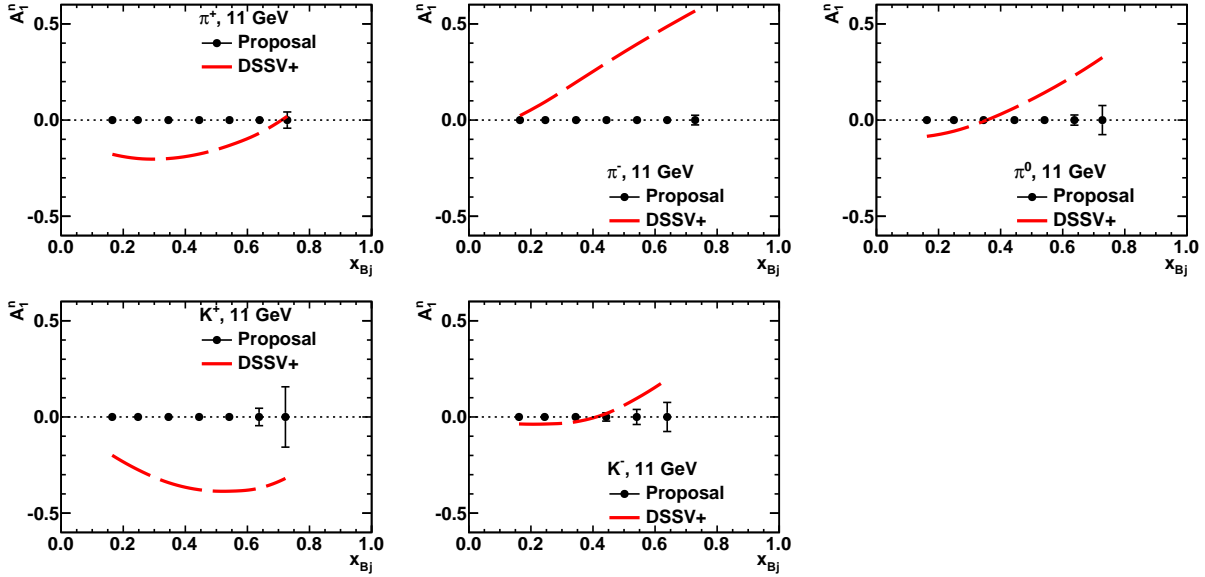


Figure 4.12: Projected uncertainties in  $A_{1n}^h$  for each hadron species at 11 GeV as a function of  $x$ , integrated over all  $z$  values passing the global SIDIS kinematic cut, compared to the “DSSV+” prediction [45].

Figures 4.12 and 4.13 show the projected statistical uncertainties in  $A_{1n}^h$  for each hadron species as a function of  $x$ , from the combined running at both SBS angle settings at 11 and 8.8 GeV, respectively, integrated over all  $z$  values for events passing the global SIDIS kinematic cut. The projected asymmetry uncertainties are compared to the predictions of the “DSSV+” NLO global QCD analysis of the DSSV group [45], which expanded the 2008 “DSSV” analysis [7, 46] to include

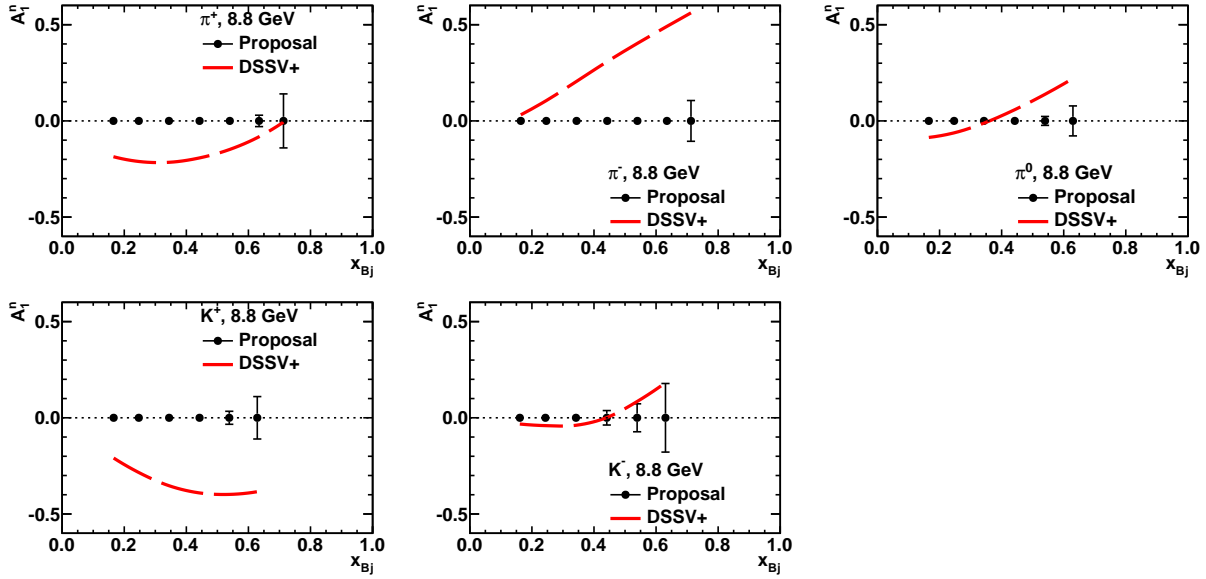


Figure 4.13: Projected uncertainties in  $A_{1n}^h$  for each hadron species at 8.8 GeV as a function of  $x$ , integrated over all  $z$  values passing the global SIDIS kinematic cut, compared to the “DSSV+” prediction [45].

subsequent data from the COMPASS collaboration on longitudinal spin asymmetries in  $\mu p$  and  $\mu d$  SIDIS [47, ?]. Figures D.1-D.5 show the projected statistical uncertainties  $\Delta A_{1n}^h(x, z)$  for the combined data from both SBS angle settings at 11 GeV beam energy as a function of  $x$  in each  $z$  bin. Figures D.6-D.10 show the projected statistical uncertainties  $\Delta A_{1n}^h(x, z)$  from the combined 8.8 GeV running at both SBS angle settings. In all figures, the curves showing the predicted neutron asymmetries in each kinematic bin are obtained via trilinear interpolation of a three dimensional grid kindly provided by the authors of [45] at the average kinematics ( $\langle x \rangle, \langle z \rangle, \langle Q^2 \rangle$ ) of each bin.

#### 4.3.6 Resolution, background and trigger rates

Detailed discussions of the effects of detector resolution, estimates of the detector background and trigger rates and the logic of the data acquisition were presented in the proposal of E12-09-018 to PAC38 [27]. Since the configuration of the proposed experiment is mostly identical to E12-09-018, the reader is referred to the earlier proposal for technical details. At the time of submission of this proposal, new Monte Carlo calculations of the detector background and trigger rates for the ten-degree setting of SBS are in progress. At both settings, updated simulations reflecting the progress in design of the SBS magnet and the downstream beamline in Hall A since the PAC38 proposal are ongoing. Given the relatively small difference in SBS central angle between the two settings and the slight increase in the target-SBS magnet distance, a moderate but tolerable increase in the background and trigger rates at the small-angle setting is expected.

#### 4.3.7 Comparison to Existing Data

The only previously published data for SIDIS double-spin asymmetries  $A_1^h$  measured on a  ${}^3\text{He}$  target are from the HERMES Collaboration [41]. Figure 4.14 shows the projected uncertainties in

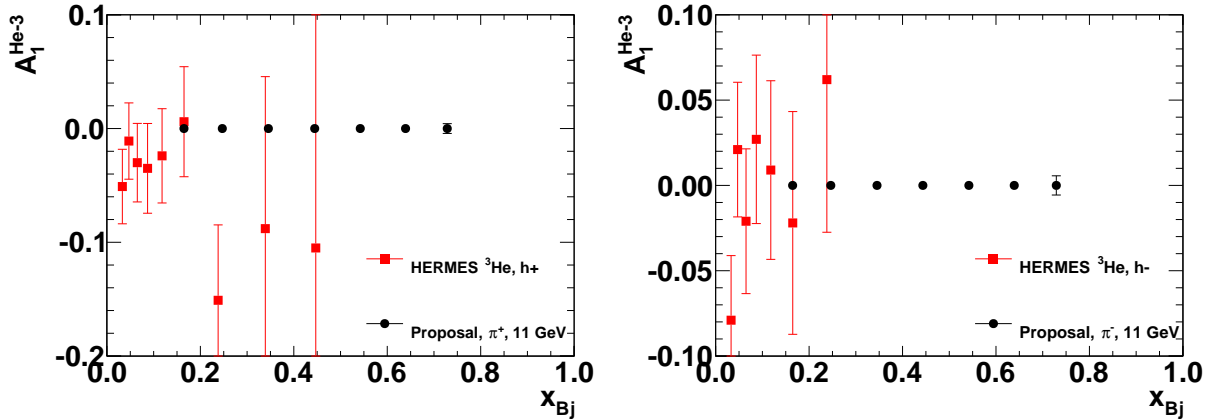


Figure 4.14: Projected uncertainties in  $A_{1^{3}\text{He}}^h$  for  $h = \pi^+$  (left) and  $h = \pi^-$  (right), as a function of  $x$ , integrated over all  $z$  values satisfying the global SIDIS kinematic cut (from the data collected at 11 GeV only). Projected  ${}^3\text{He}$  asymmetry uncertainties are compared to the results from HERMES [41] for unidentified positive (left) and negative (right) charged hadrons.

$A_{1,{}^3\text{He}}^{\pi^+}(x)$  and  $A_{1,{}^3\text{He}}^{\pi^-}(x)$  for the data collected at a beam energy of 11 GeV in the proposed experiment, integrated over all  $z$  values, for events satisfying the global SIDIS kinematic cuts described above. The projected statistical precision of the proposed measurements is compared to the HERMES results on  ${}^3\text{He}$  [41] for unidentified charged hadrons. A dramatic improvement compared to existing  ${}^3\text{He}$  data is evident. Existing deuterium data from the SMC [2] and COMPASS [48, 47, 4] collaborations are also sensitive to neutron asymmetries. Moreover, the eg1-dvcs experiment in JLab Hall B has also obtained high-statistics SIDIS data using 6 GeV electrons on a longitudinally polarized ND<sub>3</sub> target, which are currently under analysis. A more detailed discussion of the impact of the proposed measurements compared to existing data for nucleon spin-flavor decomposition is given in chapter 5 and appendices B and E.

#### 4.3.8 Comparison to Other Approved Experiments and Unique Advantages of This Proposal

Two other JLab 12 GeV experiments have been approved with physics goals similar to this proposal. The CLAS12 collaboration proposed to measure SIDIS asymmetries in charged and neutral pion production on a longitudinally polarized ND<sub>3</sub> target in a 50 day run in Hall B [49] and the Hall A Collaboration proposed to measure charged pion SIDIS asymmetries on a longitudinally polarized  ${}^3\text{He}$  target using a new large-acceptance solenoidal magnetic spectrometer known as SOLID [50] in a 35-day run in Hall A. While the relative statistical figure of merit (FOM) and physics impacts of the various experiments are complicated functions of acceptance, luminosity, target parameters, and the underlying kinematic dependencies of the SIDIS cross section, a naive approximate figure-of-merit comparison can be made based on a few key parameters. The experimental FOM for double-spin asymmetries is defined as the reciprocal relative statistical asymmetry uncertainty squared, and is proportional to the product of the event rate and the square of the asymmetry magnitude:

$$\left(\frac{\Delta A}{A}\right)^{-2} \propto (f_D P_B P_T)^2 \mathcal{L} \times \left(\sigma = \int_{\Delta\Omega} \frac{d\sigma}{d\Omega} d\Omega\right), \quad (4.8)$$

where  $\Delta A$  is the statistical error on the physics asymmetry of interest,  $f_D$  is the product of all “dilution” factors, including the fractions of events occurring on unpolarized nucleons and any other factors (such as kinematics) that suppress observed asymmetry magnitudes,  $P_B$  and  $P_T$  are the beam and target polarizations, respectively, and  $\sigma$  is the scattering cross section integrated over the experimental acceptance  $\Delta\Omega$  in all dimensions of the kinematic phase space of the SIDIS reaction. All of the three proposed experiments to measure neutron double-spin asymmetries in SIDIS use spectrometers with large momentum acceptance that does not substantially restrict the accessible phase space. As a first approximation, it might appear that the appropriate measure of solid-angle acceptance for comparison of FOM between different experiments is the product  $\Delta\Omega_e\Delta\Omega_h$  of the electron and hadron solid angle acceptances of the experiment. However, a simple product of the electron and hadron acceptances fails to account for the fact that most of the SIDIS event rate is concentrated at small values of  $p_T^h \approx p_h \sin\theta_{pq} \lesssim 1$  GeV. For fixed electron kinematics, the potentially *useful* solid angle coverage for the hadron arm is limited to a narrow range of angles of the observed hadron relative to the momentum transfer  $\mathbf{q}$ . For example, for a beam energy of 11 GeV, electron scattering angle  $\theta_e = 30^\circ$  and SIDIS kinematics of  $(x, z, Q^2) = (0.4, 0.5, 6.6 \text{ GeV}^2)$ , the total hadron solid angle corresponding to  $2\pi$  acceptance in  $\phi_h$  and  $0 \leq p_T \leq 1$  GeV is 174 msr.

Table 4.3: Comparison of experiment parameters for JLab 12 GeV experiments measuring  $A_{LL}$  asymmetries in SIDIS on polarized neutrons. The maximum useful hadron solid angle was estimated for “typical” SIDIS 11 GeV kinematics of  $(x, z, Q^2) = (0.4, 0.5, 6.6 \text{ GeV}^2)$ . The “naive” relative FOM was estimated using  $FOM = (f_D P_B P_T)^2 \mathcal{L} \Delta\Omega_e \Delta\Omega_h$ .

Experiment	SBS+BB ${}^3\text{He}$ (This proposal)	CLAS12 ND <sub>3</sub>	SOLID ${}^3\text{He}$
$P_B$	0.85	0.85	0.85
$P_T$	0.6	0.4	0.6
$f_D$	0.3	0.15	0.3
$\mathcal{L}$ (Hz/cm <sup>2</sup> )	$1.2 \times 10^{37}$	$1.0 \times 10^{35}$	$3 \times 10^{36}$
$\Delta\Omega_e$ (msr)	64	667	416
<i>Useful</i> $\Delta\Omega_h, p_T \leq 1$ GeV (msr)	40	174	96
Naive relative FOM (a.u.)	1	0.035	3.9

Table 4.3 shows a comparison of the basic parameters of the three proposed JLab 12 GeV experiments measuring SIDIS double-spin asymmetries on polarized neutrons, including the approved CLAS12 ND<sub>3</sub> run, the approved SOLID longitudinal  ${}^3\text{He}$  run, and the proposed measurements. These comparisons involve crude estimates for typical SIDIS kinematics using approximate acceptances of the detectors. The actual FOM varies strongly as a function of kinematics. Because of the higher luminosity, more favorable dilution factor and higher polarization of the  ${}^3\text{He}$  targets in this proposal and the SOLID proposal, the FOM for neutron asymmetries extracted from measurements on  ${}^3\text{He}$  is typically 10-100 times larger than for ND<sub>3</sub> measurements using CLAS12 at its design luminosity of  $10^{35} \text{ cm}^{-2} \text{ s}^{-1}$ , *before* accounting for the strongly polarized proton in deuterium and the requirement that the proton asymmetry be independently measured and subtracted from the deuteron asymmetry to extract the neutron information. Owing to the  $e_q^2$  weighting of the cross section, scattering on  $u$  quarks tends to dominate and therefore the sensitivity of deuteron asymmetries to the neutron is further reduced. On the other hand, the very large acceptance of CLAS12 makes it ideally suited for measurements on polarized proton targets, given the limited maximum

luminosity capability of polarized proton targets based on dynamic nuclear polarization such as ND<sub>3</sub>.

The comparison between this proposal and the approved proposal using SOLID is more subtle, since at first glance the SOLID experiment appears to have far superior FOM based on a naive comparison of the total charged pion event rates between the two experiments. In fact, the two experiments are complementary because there is very little overlap between the kinematic coverages of this proposal and the SOLID proposal, and the SBS-BB combination has several advantageous features for the study of SIDIS that will be discussed below. Figure 4.15 illustrates the comple-

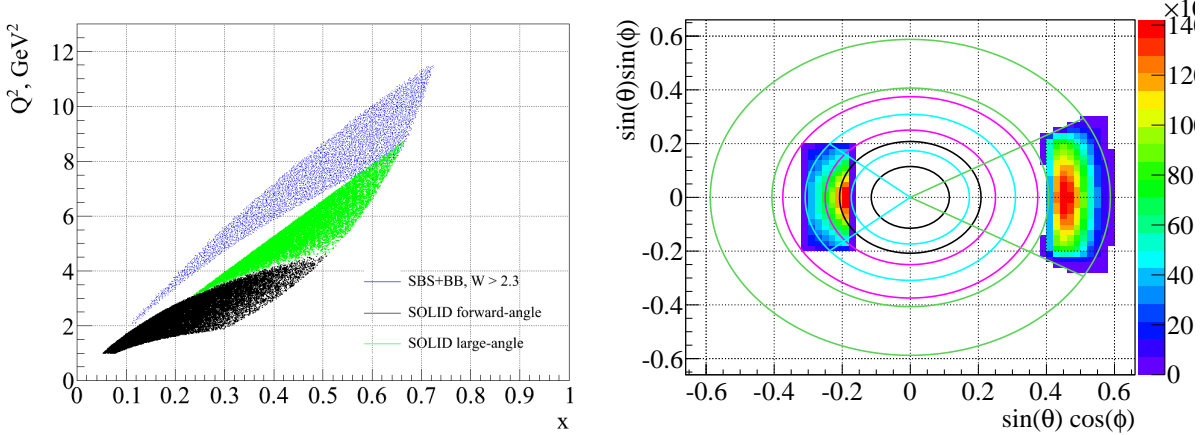


Figure 4.15: Comparison of  $Q^2 - x$  coverage (left) and  $(\theta, \phi)$  scattering angle coverage around the beam direction (right) between the SOLID experiment and the SBS-BB configuration with SBS at  $14^\circ$ . In the right panel, the circles show contours of constant  $\theta$ . The coverage of the SOLID forward-angle detectors (black circles) is  $6.6^\circ \leq \theta \leq 12^\circ$ . The coverage of the SOLID large-angle detectors (magenta circles) is  $14.5^\circ \leq \theta \leq 22^\circ$ . At a central angle of  $14^\circ$ , the SBS  $\theta$  coverage (cyan) is approximately  $10^\circ \leq \theta \leq 18^\circ$ , and for BigBite at  $30^\circ$ , the  $\theta$  coverage is roughly  $24^\circ \leq \theta \leq 36^\circ$ . The azimuthal coverages of SBS and BigBite are approximately  $\pm 40^\circ$  and  $\pm 30^\circ$ , respectively.

mentarity of the kinematic coverages of this proposal and the SOLID experiment [50]. The SOLID design emphasizes extremely high statistical precision for a fully differential mapping of SIDIS asymmetries in all dimensions of the kinematic phase space at somewhat lower average  $Q^2$  values. The SOLID forward-angle (large-angle) detector covers the range  $6.6^\circ(14.5^\circ) \leq \theta \leq 12^\circ(22^\circ)$ , with roughly  $2\pi$  azimuthal coverage around the beamline in each case. In SOLID, electrons are detected in both forward-angle and large-angle detectors, whereas charged pions are identified only in the forward detectors. In the proposed experiment, by operating the target at roughly four times higher luminosity than that of the SOLID proposal and focusing the kinematic coverage at larger scattering angles, higher values of  $Q^2$  and  $x_{Bj}$  become accessible. At a given beam energy and  $x$  value, the electron scattering angle  $\theta_e$  (and the corresponding  $Q^2$ ) is always larger in this proposal than in the SOLID experiment, making the kinematic coverages of this proposal and SOLID entirely complementary.

Figure 4.16 shows a comparison between the FOM of the SOLID experiment [51] and the approved transversity experiment E12-09-018 [27] for transverse single-spin asymmetry measurements as a function of  $Q^2$ . Similar considerations apply for  $A_{LL}$  measurements. Most of the SOLID advantage in FOM over the SBS+BB configuration of E12-09-018 and this proposal derives from the

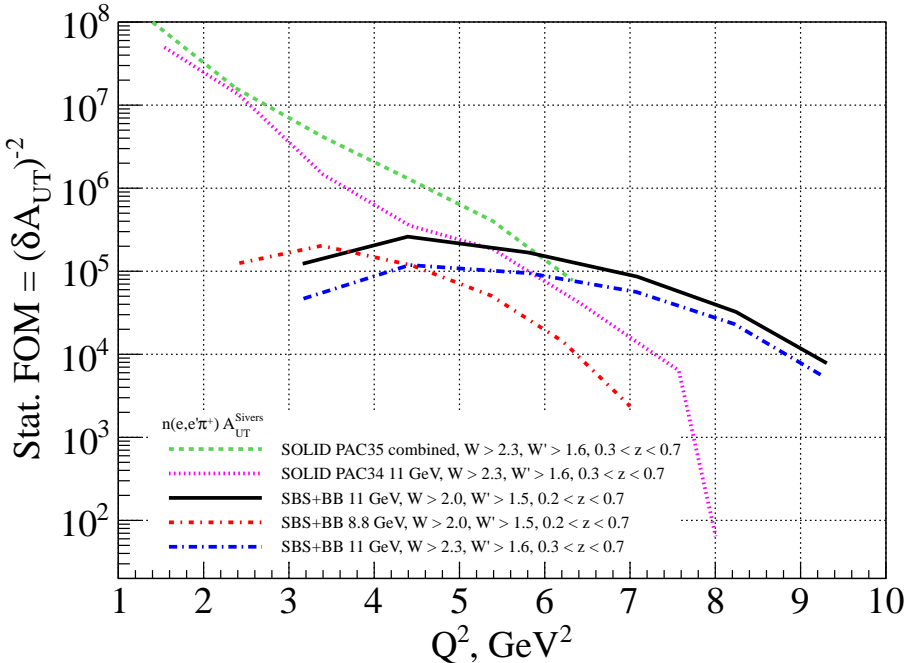


Figure 4.16: Comparison of SBS+BB and SOLID statistical FOM for transverse single spin asymmetry  $A_{UT}$  measurements in  $n(e, e'\pi^+)X$  as a function of  $Q^2$  at a beam energy of 11 GeV. The green dashed curve shows the SOLID FOM with cuts of  $W > 2.3$  GeV,  $W' = M_X > 1.6$  GeV and  $0.3 < z < 0.7$ , from the PAC35 proposal [51], while the magenta dotted curve shows the FOM from the SOLID PAC34 proposal, which considered a different solenoid magnet option. The black solid curve shows the SBS+BB FOM at 11 GeV for  $W > 2$  GeV,  $M_X > 1.5$  GeV,  $0.2 < z < 0.7$ , while the blue dot-dashed curve shows the effect of using the same cuts as SOLID. The red dot-dashed curve shows the SBS+BB FOM at 8.8 GeV.

region  $1 \leq Q^2 \leq 3$  GeV $^2$  where event rates are large. As shown in table 4.3, although the SOLID device possesses a significant advantage in electron and hadron solid angle acceptance compared to BigBite/SBS, this is partially offset by the higher luminosity of the target used in the SBS+BB experiments, and without considering the details of kinematics and cross sections, the “naive” FOM values of the two experiments (luminosity  $\times$  solid angle) are of the same order of magnitude. Figure 4.16, which includes the full details of the acceptance-convoluted cross section, shows that the advantage in statistical precision of the SOLID device derives largely from higher event rates at lower  $Q^2$  values. The SBS+BB configuration and the SOLID device also have complementary  $(\phi_h, p_T)$  coverages, as shown in Figure 4.17. Whereas the SOLID device has reasonably complete  $\phi_h$  coverage at low  $x$  values, the SBS, which detects hadrons at slightly larger angles, has increasing  $\phi_h$  coverage at high  $x$ .

### Unique advantages of this proposal

In addition to the foregoing comparisons of this proposal with other similar approved proposals, we mention here several of the key advantages of the proposed experiment in the study of SIDIS physics. For more detailed discussions, see also the PAC38 proposal for the approved E12-09-018 [27].

- Measurements at high  $Q^2$  values, where an interpretation in terms of leading-twist PDFs and

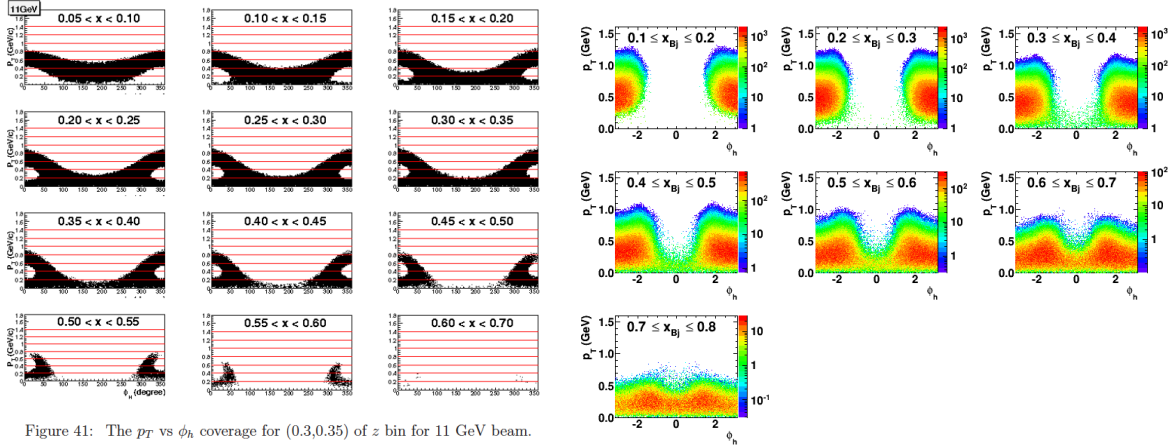


Figure 41: The  $p_T$  vs  $\phi_h$  coverage for  $(0.3, 0.35)$  of  $z$  bin for 11 GeV beam.

Figure 4.17: Left: SOLID  $(\phi_h, p_T)$  coverage at 11 GeV in different  $x$  bins at a fixed  $z$  bin of  $0.3 \leq z \leq 0.35$ . Right: SBS+BB  $(\phi_h, p_T)$  coverage at 11 GeV in different  $x$  bins for a fixed  $z$  range of  $0.4 \leq z \leq 0.5$ .

FFs is likely to be a better approximation to reality.

- Detectors located in field-free regions behind dipole magnets; simplicity and reliability of reconstruction and data analysis.
- Identical phase-spaces for positive and negative hadrons; reversing SBS magnet polarity cancels residual differences in acceptance/efficiency between positive and negative hadrons and increases  $\phi_h$  coverage, *without changing electron phase space; a unique advantage of using independent electron and hadron spectrometers*.
- Reliable identification of charged kaons and neutral pions in addition to charged pions significantly increases physics impact. Kaons enhance sensitivity to strange sea polarization, while the  $\pi^0$  channel will provide additional flavor sensitivity and aid in the understanding of the reaction mechanism.
- Hadron arm solid angle acceptance optimized for more complete  $(\phi_h, p_T)$  coverage at high  $x$  values where counting rates are low.

## Chapter 5

# Expected Results on Nucleon Spin-Flavor Decomposition

In this Chapter, we present expected results on nucleon-spin flavor decomposition according various methods described in Chapter 2, and the corresponding statistical uncertainties. We also address major sources of systematical uncertainties.

### 5.1 Systematic uncertainties on asymmetry $A_{1He}^h$ and $A_{1n}^h$

Knowledge of target polarization and dilution factor dominates the systematic uncertainty of  $A_{1n}^h$ . The effects of radiative corrections will be treated in a Monte Carlo simulation following the procedures of the HERMES analysis [?], which found that the systematic uncertainties introduced by this procedure are negligible. Kinematic smearing will also be treated following the procedure of the HERMES analysis.

Major systematic uncertainties on  $A_{1He}^h$ :

Target polarization $\delta P_T/P_T$ :	$\pm 2.5\%$ relative
Beam polarization $\delta P_B/P_B$ :	$\pm 2.0\%$ relative
Helicity correlated beam charge uncertainty $\delta(Q_+/Q_-)$ :	$\ll 10^{-4}$ absolute
Radiative correction and kinematic smearing:	$\pm 1.5\%$ relative
Knowledge of $R$ and correction from $A_\perp$ :	$\pm 1.5\%$ relative
<b>Total systematic uncertainty on <math>A_{1He}^h</math></b>	<b><math>\pm 3.8\%</math> relative</b>

Extra systematic uncertainties involved in extracting  $A_{1n}^h$ :

Dilution factor $\delta f/f$ :	$\pm 2.5\%$ relative
Effective neutron polarization in ${}^3\text{He}$ $\delta P_n/P_n$ :	$\pm 4.2\%$ relative
<b>Systematic uncertainty on <math>A_{1n}^h</math> (exp.+theory):</b>	<b><math>\pm 6.2\%</math> relative</b>

## 5.2 Expected results from NLO global fit and impacts to DSSV2008

### 5.3 Expected results from Leading-Oder “purity” method

### 5.4 Expected results from Leading-Order Christova-Leader method

#### 5.4.1 Statistical uncertainties of the combined asymmetries $A_{1He}^{\pi^+ - \pi^-}$

The combined asymmetry  $A_{1He}^{\pi^+ - \pi^-}$  needs the cross section ratio  $r = \sigma_{He}^{\pi^-}/\sigma_{He}^{\pi^+}$  as an extra input:

$$A_{1He}^{\pi^+ - \pi^-} = \frac{\Delta\sigma_{He}^{\pi^+} - \Delta\sigma_{He}^{\pi^-}}{\sigma_{He}^{\pi^+} - \sigma_{He}^{\pi^-}} = \frac{A_{1He}^{\pi^+} - A_{1He}^{\pi^-} \cdot r}{1 - r}. \quad (5.1)$$

For this experiment, we have roughly  $r = \sigma_{He}^{\pi^-}/\sigma_{He}^{\pi^+} = 0.4 \sim 0.8$ . The error propagation follows:

$$(\delta A_{1He}^{\pi^+ - \pi^-})^2 = \frac{1}{(1-r)^2} \left[ (\delta A_{1He}^{\pi^+})^2 + r^2 (\delta A_{1He}^{\pi^-})^2 + (A_{1He}^{\pi^+} - A_{1He}^{\pi^-} \cdot r)^2 \cdot \frac{(\delta r)^2}{(1-r)^2} \right]. \quad (5.2)$$

The value of  $r$  can be reasonably determined to better than  $|\delta r|/r \leq 2.0\%$  relatively in this experiment since phase spaces are identical for  $\pi^+$  and  $\pi^-$  measurements. Inside the bracket of Eq. 5.2, the first term is always larger than the second term, while the third term is in the order of  $(0.5 \sim 1.5 \times 10^{-3})^2$ . Therefore, the first term dominates in Eq. 5.2, except in the few very high statistics bins at low- $x$  and low- $z$  in which  $A_{1He}^{\pi^+}$  can be determined to better than  $10^{-3}$ . Basically, through Eq. 5.2, statistical uncertainties of  $A_{1He}^{\pi^+ - \pi^-}$  receives an amplification factor of  $1/(1-r)$ .

#### 5.4.2 Valence quark polarization

Following Eq. 3.14, we have statistical uncertainties:

$$\delta(\Delta d_v - \frac{1}{4}\Delta u_v)_{LO} = \frac{1}{4}(7u_v + 2d_v)\delta(A_{1He}^{\pi^+ - \pi^-}). \quad (5.3)$$

Statistical uncertainties of  $\Delta d_v - \frac{1}{4}\Delta u_v$ , according to the Leading-Order Christova-Leader spin-flavor decomposition method and taking into account of effective neutron polarization in a  ${}^3\text{He}$  nuclei, are listed in Appendix E, for each bin of  $(x, Q^2, z)$ , together with the expected statistical uncertainties in determining  $A_{1He}^{\pi^+ - \pi^-}$ . For most bins of  $(x, Q^2, z)$ , the combined asymmetry  $A_{1He}^{\pi^+ - \pi^-}$  can be determined to better than 1% level. The  $z$ -dependence behavior of  $A_{1He}^{\pi^+ - \pi^-}$  (and  $A_{1He}^{\pi^+ + \pi^-}$ ), for different  $z$ -bins corresponding to the same  $(x, Q^2)$ , can be used to verify the predicted Leading-Order  $x - z$  naive separation, or set a systematic upper limit on how well this assumption holds.

Once the  $z$ -dependence behavior is verified, data from different  $z$ -bins corresponding to the same  $(x, Q^2)$  can be combined, the results are listed in Table 5.1. Assuming other experiments on polarized proton target can reach a similar precision on  $\Delta u_v - \frac{1}{4}\Delta d_v$ , especially from CLAS12 polarized  $\text{NH}_3$  target SIDIS data, the expected statistical uncertainties on  $\Delta u_v - \Delta d_v$

Statistical accuracies of  $x\Delta d_v$  from this experiment, according to the leading order Christova-Leader method, are plotted in Fig. 5.1. Each data point represents a combination of six  $z$ -bins as listed in Appendix E. The published data from SMC [2], HERMES [3] and COMPASS [4], which used the “purity” method and included inclusive asymmetry data, are also plotted. Noticed that since the sum of  $\Delta q + \Delta \bar{q}$  is reasonably well-constrained by inclusive DIS data of spin structure functions  $g_{1p}$  and  $g_{1n}$ , through SIDIS, statistical uncertainties on  $\Delta q$  and  $\Delta q_v$  follow as  $\delta(\Delta q) \sim$

$\langle x \rangle$	$\langle Q^2 \rangle$ GeV $^2$	$\delta \left( A_{^{1}He}^{\pi^+ - \pi^-} \right)$ %	$\delta [x(\Delta d_v - \frac{1}{4}\Delta u_v)]_{CL}$	$\delta(\Delta u_v - \Delta d_v)_{CL}$
E <sub>0</sub> =11 GeV	5.20			
0.166	3.29	0.25	0.0038	0.0259
0.249	4.64	0.18	0.0028	0.0125
0.347	6.09	0.22	0.0026	0.0084
0.445	7.38	0.30	0.0023	0.0058
0.532	8.65	0.46	0.0021	0.0045
0.629	9.65	0.83	0.0018	0.0032
0.720	10.73	2.16	0.0017	0.0027
E <sub>0</sub> =8.8 GeV	3.84			
0.168	2.58	0.27	0.0042	0.0281
0.248	3.54	0.21	0.0032	0.0144
0.345	4.61	0.26	0.0032	0.0105
0.436	5.60	0.39	0.0033	0.0085
0.520	6.77	0.69	0.0036	0.0078
0.628	7.19	1.57	0.0037	0.0066
0.714	8.33	12.49	0.0117	0.0185

Table 5.1: Combining all  $z$ -bins for the same  $(x, Q^2)$ , the expected statistical uncertainties of  $A_{^{1}He}^{\pi^+ - \pi^-}$  and extracted valence quark polarization  $\delta(\Delta d_v - \frac{1}{4}\Delta u_v)_{CL}$  according to leading order Christova-Leader (CL) method. The expected statistical precision of  $\Delta u_v - \Delta d_v$  are also listed, assuming other experiments on polarized proton target can reach a similar precision on  $\Delta u_v$ .

$\delta(\Delta\bar{q})$  and  $\delta(\Delta q_v) = \delta(\Delta q - \Delta\bar{q}) \sim 2 \cdot \delta(\Delta\bar{q})$ . QCD global fit of DSSV2008 [7] and a covariant Quark-Diquark Model [52] of I. Cloet *et al.* are also shown. When the HERMES data were analyzed following the Christova-Leader method, dramatic increase in statistical uncertainties can not be avoided due to the unfavorable cross section ratio of  $\sigma^{\pi^-}/\sigma^{\pi^+}$  in the HERMES kinematics (see Fig. B.3 in Appendix). The SMC data, which assumed symmetric sea polarization, are also shown.

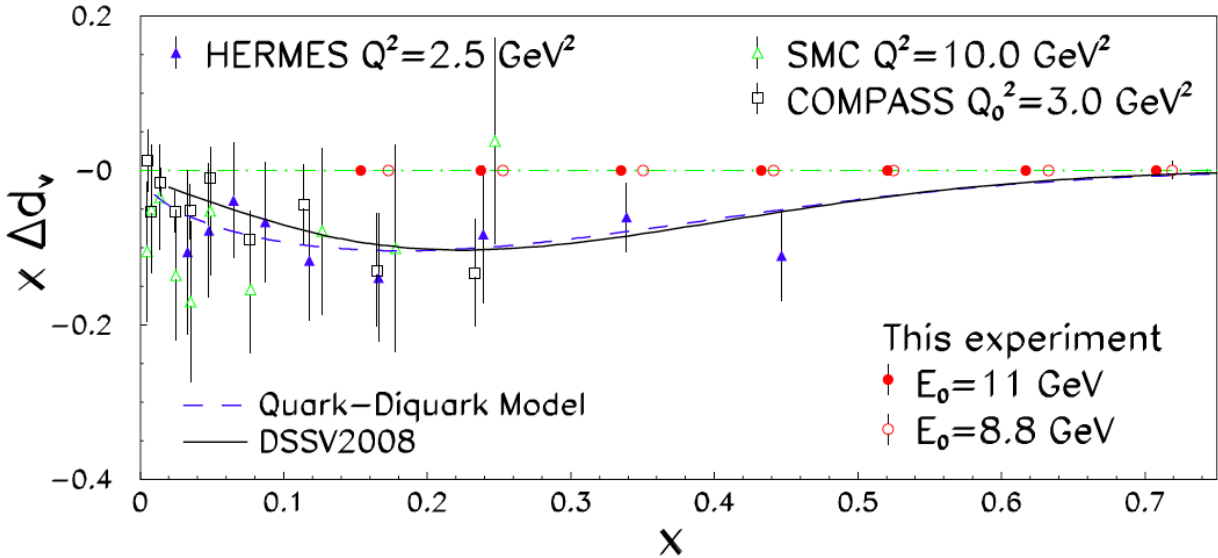


Figure 5.1: The expected statistical precision of  $x\Delta d_v$  from Leading Order Christova-Leader method. Each data point represents a combination of six  $z$ -bins as listed in Appendix E. The published SMC [2], HERMES [3] and COMPASS [4] results which included a combined data set of inclusive and semi-inclusive asymmetries, are also shown. QCD global fit of DSSV2008 [7] and a covariant Quark-Diquark Model [52], both calculated at  $Q^2 = 4.0 \text{ GeV}^2$ , are also shown.

When extracting  $(\Delta d_v - \frac{1}{4}\Delta u_v)_{LO}$  the knowledge of unpolarized PDF ( $\delta q/q \approx \pm 4\%$ ) contributes to the systematic uncertainties. Theoretical uncertainties PDF on unpolarized and  ${}^3\text{He}$  to neutron correction) dominate the systematics in  $\Delta d_v$ , However, these systematic uncertainties are to be multiplied by the size of  $A_{1\text{He}}^{\pi^+ - \pi^-}$ , at the level of a few percent, when entering into  $\Delta d_v$ ,

#### 5.4.3 Statistical uncertainty on $\Delta\bar{u} - \Delta\bar{d}$ when combined with JLab-12 GeV proton target data

To further extract  $\Delta\bar{u} - \Delta\bar{d}$  according to Eq. 3.20, knowledge of  $\Delta u_v - \Delta d_v$ , and inclusive spin structure function  $g_{1p}$  and  $g_{1n}$  are needed. Of course, the best option is to perform measurements on three different polarized targets (proton, deuteron and  ${}^3\text{He}$ ) within the same experimental set up, such that consistency checks are possible to set limits on systematic uncertainties of  $\Delta u_v - \Delta d_v$ .

For this experiment, we will follow the “second best” option. The neutron ( ${}^3\text{He}$ ) data from this experiment, or  $\Delta d_v - \frac{1}{4}\Delta u_v$ , will be combined with the world data on polarized proton target, especially from the planned CLAS12 measurement, to obtain the best knowledge of  $\Delta u_v - \Delta d_v$ .

Assuming the world future proton target SIDIS data can reach the similar statistical uncertainties of this experiment, and recall Eq. 3.20:

$$[\Delta\bar{u}(x) - \Delta\bar{d}(x)]_{LO} = 3[g_1^p(x) - g_1^n(x)] - \frac{1}{2}(\Delta u_v - \Delta d_v)|_{LO}.$$

From JLab-6 GeV experiments [?, ?], currently we have  $\delta g_1^p \leq 0.0059$ ,  $\delta g_1^n \leq 0.0057$ . Table 5.2 lists the expected statistical uncertainties on  $x(\Delta\bar{u} - \Delta\bar{d})_{LO}$ , based on our current knowledge of  $g_1^p(x, Q^2)$  and  $g_1^n(x, Q^2)$ . We note that several experiments at JLab-12 GeV, such as the Hall A  $A_{1n}$ , Hall C  $A_{1n}$  experiments, and CLAS12 measurements, together with the BigBite single-arm electron measurement of this experiment could dramatically reduce the uncertainties on the inclusive spin structure  $g_1^p(x, Q^2)$  and  $g_1^n(x, Q^2)$ .

$\langle x \rangle$	$\langle Q^2 \rangle$	$\frac{1}{2}\delta(\Delta u_v - \Delta d_v)$	$3\delta g_1^p$	$3\delta g_1^n$	$\delta(\Delta\bar{u} - \Delta\bar{d})_{LO}$
		stat.	stat.	stat.	stat.
E <sub>0</sub> =11 GeV	5.20				
0.166	3.29	0.0130	0.0177	0.0171	0.0278
0.249	4.64	0.0062	0.0177	0.0171	0.0254
0.347	6.09	0.0042	0.0177	0.0171	0.0250
0.445	7.38	0.0029	0.0177	0.0171	0.0248
0.532	8.65	0.0022	0.0177	0.0171	0.0247
0.629	9.65	0.0016	0.0177	0.0171	0.0247
0.720	10.73	0.0014	0.0177	0.0171	0.0246
E <sub>0</sub> =8.8 GeV	3.84				
0.168	2.58	0.0141	0.0177	0.0171	0.0283
0.248	3.54	0.0072	0.0177	0.0171	0.0256
0.345	4.61	0.0052	0.0177	0.0171	0.0252
0.436	5.60	0.0042	0.0177	0.0171	0.0250
0.520	6.77	0.0039	0.0177	0.0171	0.0249
0.628	7.19	0.0033	0.0177	0.0171	0.0248
0.714	8.33	0.0093	0.0177	0.0171	0.0263

Table 5.2: Expected statistical uncertainties of  $(\Delta\bar{u} - \Delta\bar{d})_{LO}$ , when combined with future SIDIS JLab-12 GeV proton target data, taking the current knowledge on inclusive DIS spin structure function  $g_1^p(x, Q^2)$  and  $g_1^n(x, Q^2)$ .

## 5.5 Other systematic uncertainties

### 5.5.1 Effective nucleon polarization in ${}^3\text{He}$

Effective nucleon polarization in  ${}^3\text{He}$  for deep-inelastic scattering gives:

$$g_1^{^3\text{He}} = P_n g_1^n + 2P_p g_1^p \quad (5.4)$$

where  $P_n(P_p)$  is the effective polarization of the neutron (proton) inside  ${}^3\text{He}$  [?]. These effective nucleon polarizations  $P_{n,p}$  can be calculated using  ${}^3\text{He}$  wave functions constructed from N-N interactions, and their uncertainties were estimated using various nuclear models [?, ?, ?, ?], giving

$$P_n = 0.86_{-0.02}^{+0.036} \text{ and } P_p = -0.028_{-0.004}^{+0.009}. \quad (5.5)$$

The small proton effective polarization (2.8%) causes small offsets in the  ${}^3\text{He}$  asymmetries, compared to that from a free neutron. The uncertainties associated with this small offset are even smaller when considering that the corresponding proton asymmetries are better known and will be improved in the coming years.

At  $x = 0.110 \sim 0.461$ , especially around  $x = 0.3$ , the nuclear EMC effect becomes rather small, as has been demonstrated on many different nucleus.

### 5.5.2 $\pi$ - $N$ final state interaction

Since pions carry no spin,  $\pi N$  final state interactions will not introduce asymmetries in  $A_{1He}^h$ . Effect of  $\pi$ - $N$  final state interaction will come through the dilution factors. By measuring the leading pions at 4.3 GeV/c, where the  $\pi$ - $N$  total cross sections are reasonably flat, effects of FSI are minimized. A detailed  $\pi$ - $N$  re-scattering calculation [?] confirmed that the modifications to the cross section are rather small at this kinematics.

### 5.5.3 Target fragmentation and vector meson production

In principle, intermediate  $\rho$  production processes are part of the fragmentation process and should not be subtracted from the SIDIS cross sections. Furthermore, due to the charge conjugation, the effect of intermediate  $\rho^0$  production is canceled in observables related to  $\pi^+ - \pi^-$ . Therefore, the Christova-Leader method of flavor decomposition is not sensitive to  $\rho$  production.

At a high- $z$  setting of this experiment ( $z \approx 0.5$ ), target fragmentation contamination is expected to be small, as has been shown by the HERMES LUND based Monte Carlo simulation. In addition, in the  $\pi^+ - \pi^-$  yield target fragmentation contributions are mostly canceled.

### 5.5.4 Corrections from non-vanishing $A_\perp^n$ (or $A_{LT}^n$ )

Since the target polarization is along the beam direction, not exactly along the virtual photon direction  $\theta_{\gamma^*}$ , measurements of  $A_{||}$  should in principle be corrected by a small contribution from  $A_\perp$  in order to obtain the physics asymmetry  $A_{1N}^h$ . In this experiment, we have  $\sin \theta_{\gamma^*} \approx 0.1$ , therefore, the uncertainty associated with this correction is of the order  $0.1 \times (\delta A_\perp^n)$ .

In the published HERMES and SMC data, the corrections from  $A_\perp$  were neglected based on the observation that in inclusive DIS  $g_2(x)$  turned out to be rather small. The residual effect of non-vanishing  $g_2$  (or  $A_\perp$ ) in SIDIS has been included in the estimation of systematic uncertainties in the HERMES case. The contribution to the fractional systematic uncertainties on  $A_{1N}^h$  was estimated to be 0.6% for proton and 1.4% for deuteron.

- The leading order contribution in  $A_\perp$  (or  $A_{LT}$  in Mulders' notation) is modulated by an angular dependence of  $\cos(\phi_s - \phi_h)$ . When a reasonable range of  $\phi_h$  is covered, as in this experiment, the averaged contribution from  $A_\perp$  will most likely to be washed out.
- Aside from the angular modulation,  $A_{LT}^n$  was predicted to be at the 10% level for the proton in bag-model calculations (Mulders, Yuan). Assuming  $A_{LT}^n$  is at the similar level, the correction to  $A_{1n}^h$  will be at 1% level for this experiment, much less than the statistical uncertainties.
- The value of  $A_{LT}^n$  has been determined in the Hall A Neutron Transversity experiment [42], with a in-plane transversely polarized  ${}^3\text{He}$  target, have provide information on  $A_{LT}^n$ . Although  $A_{LT}$  turned out to be non-zero, its size is not large [42] In addition the transverse target run in SBS Transversity will also measure  $A_{LT}^n$  to a high precision.

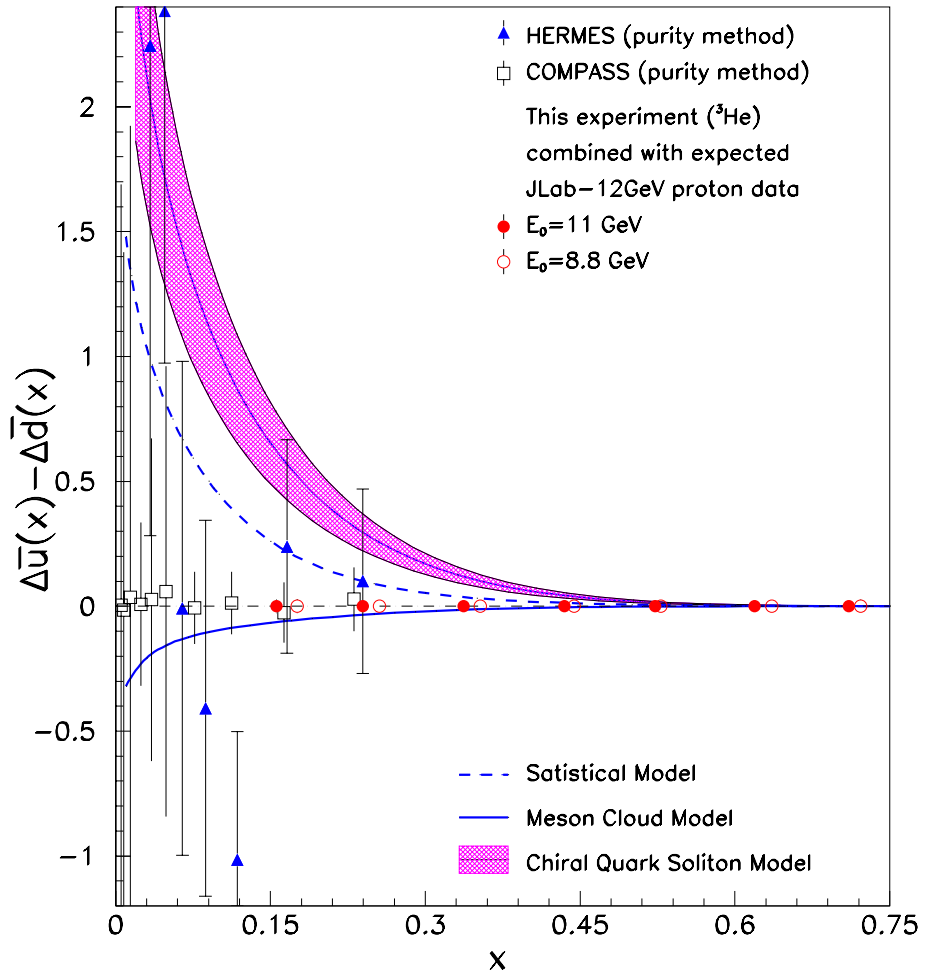


Figure 5.2: The expected statistical accuracy of  $\Delta\bar{u} - \Delta\bar{d}$ , assuming JLab-12GeV proton target data can reach a similar precision as this experiment. The published HERMES [3] and COMPASS [4] purity results, which included combined data sets of inclusive and semi-inclusive asymmetries, are also shown. Model predictions are from the Statistical Model [?], Meson Cloud Model [?] and the Chiral Quark Soliton Model [?].

## Appendix A

# Collaboration Responsibilities

The following is a list of intended contributions to the proposed experiment from the collaborating institutions.

- The Los Alamos group has played a lead role in transverse nucleon spin structure experiments including the JLab Hall A transversity experiment E06-010. The LANL group also led the effort to develop the physics motivation for the proposed experiment by collaborating with leading theorists working in the field of nucleon spin structure to characterize the physics impact of the proposed measurements in depth.
- The University of Connecticut (UConn) Group will take responsibility for the preparation of the RICH detector that will be used in SBS for the proposed experiment and the approved transversity experiment E12-09-018, including testing of the PMTs and optical components of the RICH. UConn will also make major contributions to Monte Carlo simulations and software development for both reconstruction and physics analysis of all the SBS experiments. The UConn group intends to put at least one Ph.D. thesis student on the proposed experiment.
- The UVa group will take responsibility for the construction and operation of the high-polarization high-luminosity  ${}^3\text{He}$  target, which is also a major part of an approved GEN experiment. The UVa group will also take responsibility for the construction of the GEM-based tracker in the Super Bigbite Spectrometer and its operation.
- The CMU group will use their expertise in calorimeters to implement the hadron calorimeter and the beam line magnetic shielding, both of which are also required in the GEP5 experiment E12-07-109. The CMU group also plays a lead role in the approved  $G_M^n$  experiment using the SBS.
- The INFN group is committed to the realization of the approved  $G_{Ep}$  experiment and to providing a GEM tracker for BigBite, as well as taking the lead in its operation and support. They will also have a significant role in the implementation of the RICH detector. The source of funding for this group is INFN.
- The Hall A collaborators will take responsibility for the infrastructure associated with the 48D48 magnet, which will be used in both this and the three approved SBS-related Form-Factor experiments.

## Appendix B

# HERMES and COMPASS Results and NLO Global Fits

### B.1 HERMES and COMPASS results of Leading-Order purity method

The HERMES [3] and COMPASS [4] analysis explicitly assumed the  $x - z$  naive separation of Eq. 3.1 at the leading order, the asymmetries are related to the parton polarizations through linear relations as:

$$A_{1N}^h(x, Q^2, z) = \frac{\sum_f e_f^2 \Delta q_f(x, Q^2) \cdot D_f^h(z, Q^2)}{\sum_f e_f^2 q_f(x, Q^2) \cdot D_f^h(z, Q^2)}. \quad (\text{B.1})$$

The HERMES and COMPASS analysis used the “purity method” to achieve leading order flavor decomposition [?]. In Eq. B.1, a “purity matrix”  $\mathcal{P}_f^h(x, Q^2, z)$  was defined such that:

$$A_{1N}^h(x, Q^2, z) \equiv \sum_f \mathcal{P}_f^h(x, Q^2, z) \cdot \frac{\Delta q_f(x, Q^2)}{q_f(x, Q^2)}, \quad (\text{B.2})$$

where

$$\mathcal{P}_f^h(x) = \frac{e_f^2 q_f(x) \int dz D_f^h(z)}{\sum_i e_i^2 q_i(x) \int dz D_i^h(z)}, \quad (\text{B.3})$$

and the explicit  $Q^2$  notation has been omitted for simplicity. The “purity method” integrates over all the experimentally allowed  $z$ -range such that SIDIS events are included as much as possible to improve statistical accuracy. The exact values of  $\mathcal{P}_f^h(x, Q^2, z)$  in the HERMES analysis were obtained through a detailed Monte Carlo simulation which was based on the Lund fragmentation model [?] and take into account the experimental phase space and detector efficiencies. The parameters used in the fragmentation model were fine-tuned in order to reproduce the measured hadron yields.

Integrating over hadrons with  $0.2 < z < 0.8$ , HERMES extracted five flavor quark polarizations:

$$\vec{Q} = (x\Delta u, x\Delta d, x\Delta \bar{u}, x\Delta \bar{d}, x\Delta s), \quad (\text{B.4})$$

from a data base of measured double-spin asymmetries

$$\vec{A} = (A_{1p}^{\pi^+}, A_{1p}^{\pi^-}, A_{1d}^{\pi^+}, A_{1d}^{\pi^-}, A_{1d}^{K^+}, A_{1d}^{K^-}, A_{1p}, A_{1d}) \quad (\text{B.5})$$

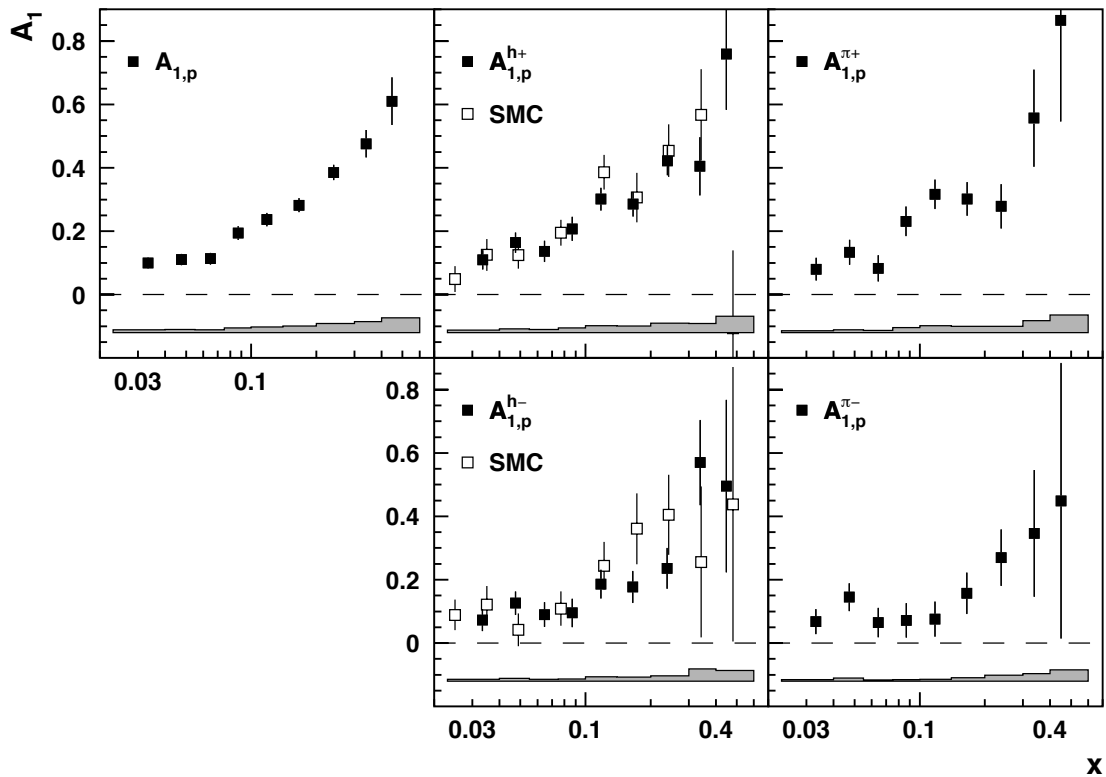


Figure B.1: The double-spin asymmetries on proton  $A_{1p}^h$  form HERMES [3] and SMC [2].

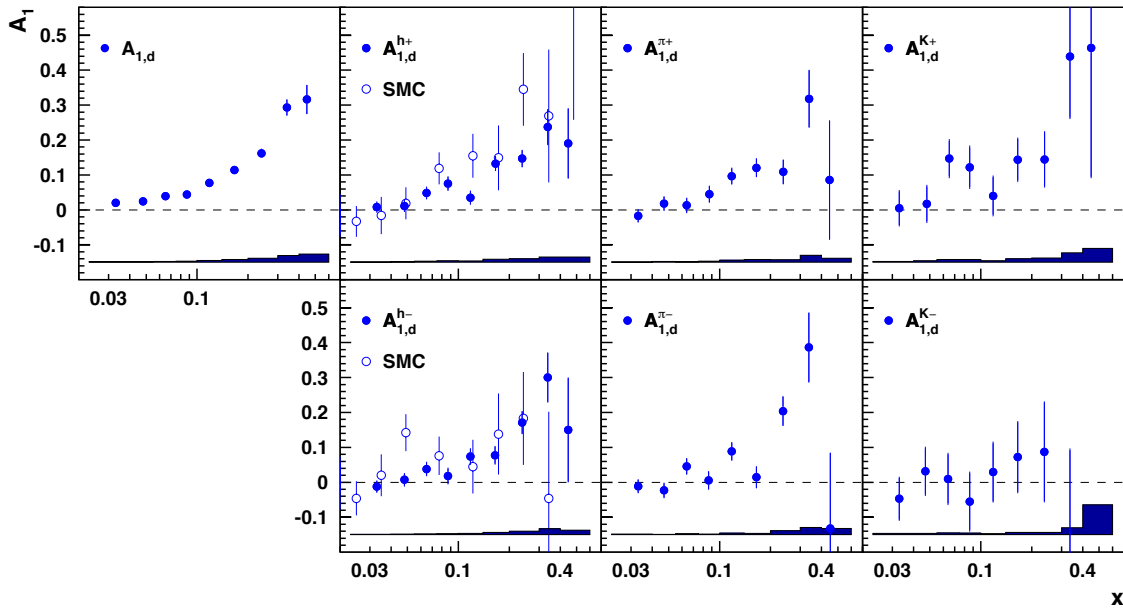


Figure B.2: The double-spin asymmetries on deuteron  $A_{1d}^h$  form HERMES [3] and SMC [2].

by solving the relations of  $\vec{A} = \mathcal{P}_f^h(x) \cdot \vec{Q}$ . The HERMES data on proton and deuteron asymmetries [?] are shown in Fig. B.1 and B.2 in comparison with the SMC data [?].

An independent effort of flavor decomposition using the leading order Christova-Leader method has also been carried out in the HERMES analysis [?], although not presented in the published data. However, due to the unfavorable  $\pi^-/\pi^+$  ratio at higher- $x$  bins in HERMES, the statistical uncertainties of the Christova-Leader method are rather large compared to that of the purity method, as shown in Fig. B.3

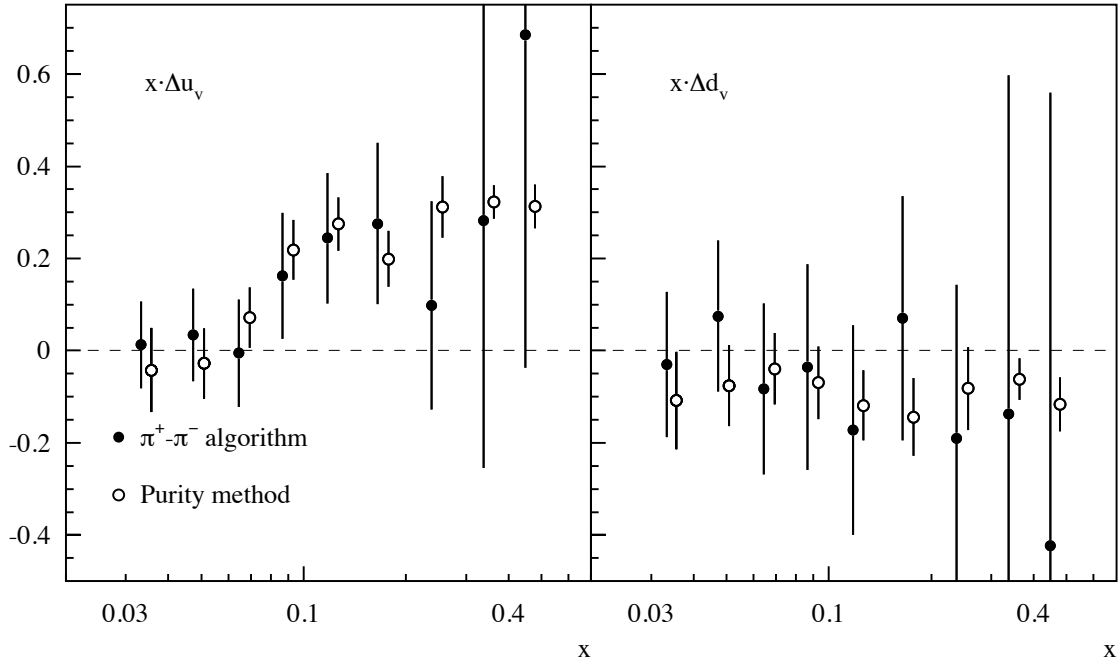


Figure B.3: Statistical error comparison of the HERMES purity method (open circles) with the HERMES Christova-Leader method analysis [?] (solid circles).

Recently, the COMPASS experiment [?] released the results of  $A_d^{h+}$  and  $A_d^{h-}$ , identified charged hardon asymmetries off a deuteron target, with improved statistical precisions at lower- $x$  region. The asymmetry results are shown in Fig. B.4.

## B.2 NLO global fit to DIS and SIDIS Data

The NLO global fit (DSSV2008) [7] to the existing DIS and SIDIS data published up to 2008 are shown in Fig. B.5.

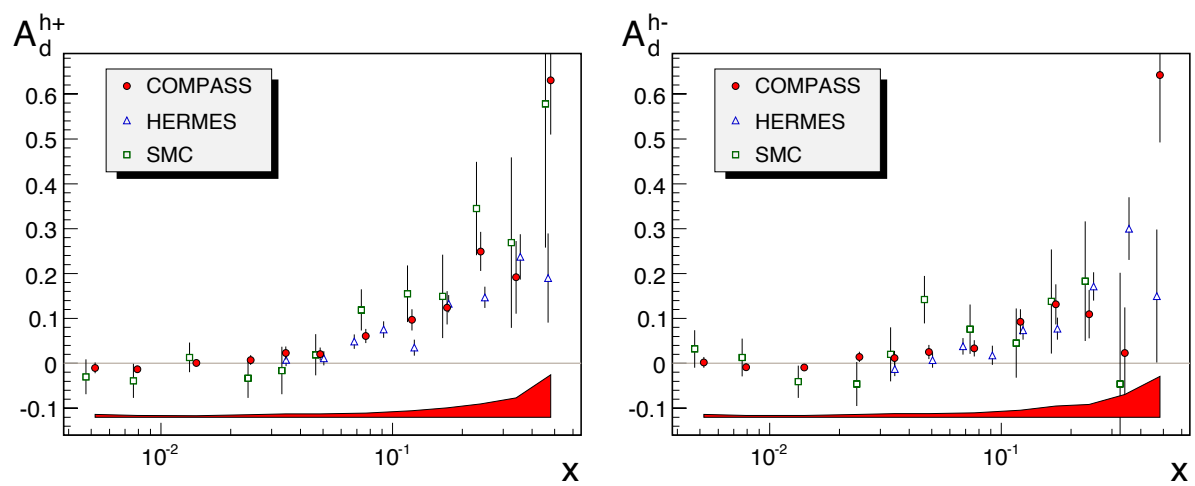


Figure B.4: Hadron asymmetry  $A_d^{h+}$  and  $A_d^{h-}$  measured by COMPASS [?], SMC and HERMES.

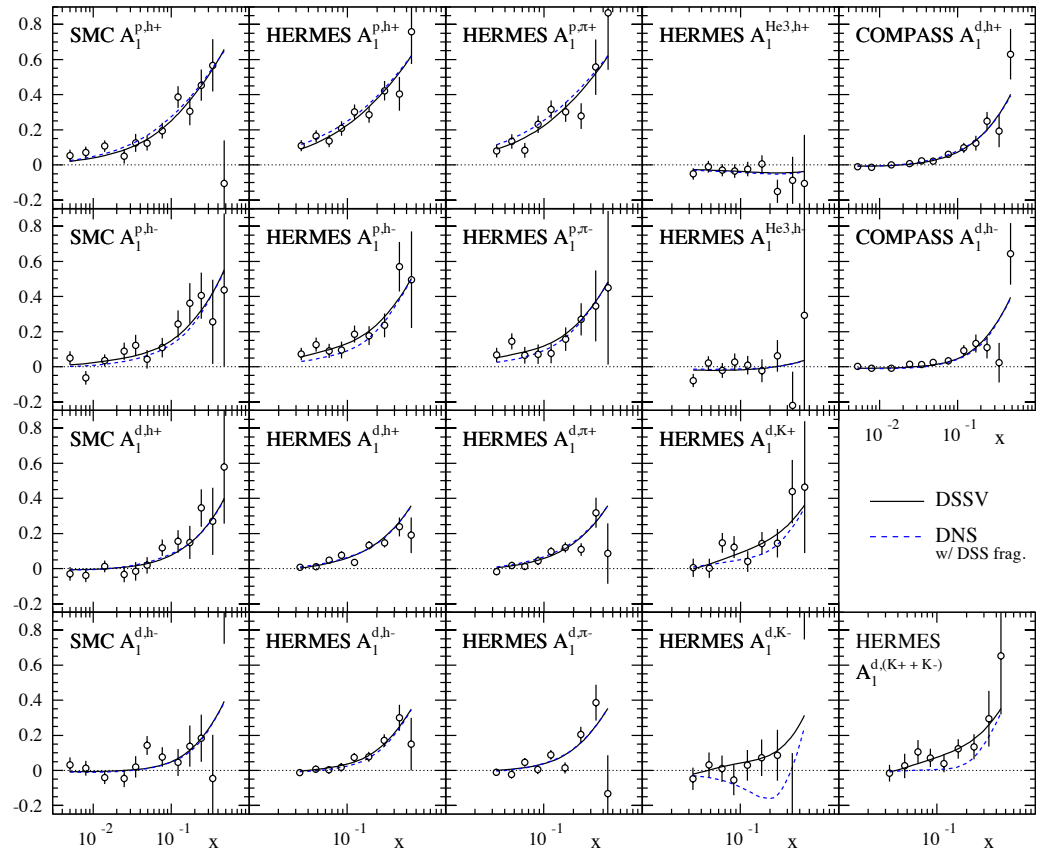
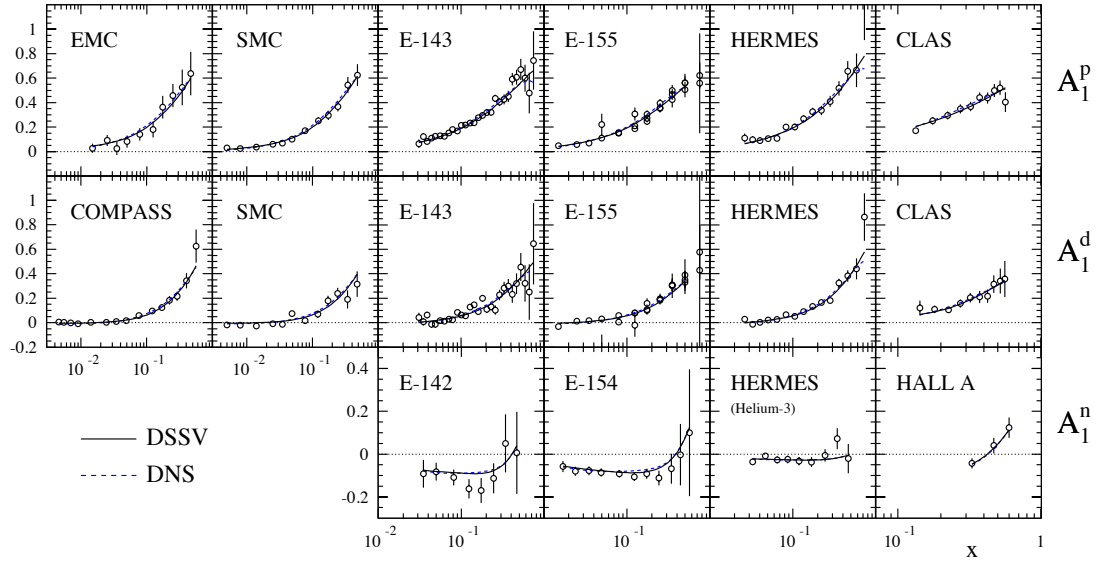


Figure B.5: NLO global fit [7] to inclusive DIS data (top) and SIDIS data (bottom).

## Appendix C

# Leading-Order SIDIS Asymmetries and SU(2) Assumptions

### C.1 Leading-order SIDIS asymmetries $A_{1N}^h$

Following the short-hand notation of Ref [?], we take the spin-independent cross section as:

$$\sigma^h(x, z) = \sum_f e_f^2 q_f(x) \cdot D_{q_f}^h(z), \quad (\text{C.1})$$

and the spin-dependent cross section as:

$$\Delta\sigma^h(x, z) = \sigma_{++}^h - \sigma_{+-}^h = \sum_f e_f^2 \Delta q_f(x) \cdot D_{q_f}^h(z), \quad (\text{C.2})$$

where  $\sigma_{ij}^h$  refers to an electron of helicity- $i$  and nucleon of helicity- $j$ . Assuming isospin symmetry and charge conjugation invariance, the number of quark to pion fragmentation functions is reduced to three types: the favored ( $D_\pi^+$ ), the unfavored ( $D_\pi^-$ ) and the  $s$ -quark ( $D_s^\pi$ ) fragmentation functions:

$$\begin{aligned} D_\pi^+ &\equiv D_u^{\pi^+} = D_d^{\pi^-} = D_{\bar{u}}^{\pi^-} = D_{\bar{d}}^{\pi^+}, \\ D_\pi^- &\equiv D_u^{\pi^-} = D_d^{\pi^+} = D_{\bar{u}}^{\pi^+} = D_{\bar{d}}^{\pi^-}, \\ D_s^\pi &\equiv D_s^{\pi^+} = D_{\bar{s}}^{\pi^-} = D_{\bar{u}}^{\pi^+} = D_{\bar{s}}^{\pi^+}. \end{aligned} \quad (\text{C.3})$$

For the quark to kaon fragmentation functions, the following relations are valid under charge conjugation [?]:

$$\begin{aligned} D_K^+ &\equiv D_u^{K^+} = D_{\bar{u}}^{K^-} = D_s^{K^+} = D_{\bar{s}}^{K^-}, \\ D_K^- &\equiv D_u^{K^-} = D_{\bar{u}}^{K^+} = D_s^{K^-} = D_{\bar{s}}^{K^+}, \\ D_d^K &\equiv D_d^{K^+} = D_{\bar{d}}^{K^+} = D_{\bar{d}}^{K^-} = D_d^{K^-}. \end{aligned} \quad (\text{C.4})$$

For this experiment, which covers  $0.16 < x < 0.73$ , we will assume a symmetrical strange quark distribution and polarization ( $s(x) = \bar{s}(x)$ ,  $\Delta s(x) = \Delta \bar{s}(x)$ ) and neglect heavy quark contributions.

### C.1.1 Spin-dependent and spin-independent cross sections at LO

According to Eq. C.1, semi-inclusive  $\pi^+$  and  $\pi^-$  cross section on proton and neutron are:

$$\begin{aligned} 9\sigma_p^{\pi^+} &= (4u + \bar{d})D_\pi^+ + (4\bar{u} + d)D_\pi^- + (s + \bar{s})D_s^\pi, \\ 9\sigma_p^{\pi^-} &= (4u + \bar{d})D_\pi^- + (4\bar{u} + d)D_\pi^+ + (s + \bar{s})D_s^\pi, \\ 9\sigma_n^{\pi^+} &= (4d + \bar{u})D_\pi^+ + (4\bar{d} + u)D_\pi^- + (s + \bar{s})D_s^\pi, \\ 9\sigma_n^{\pi^-} &= (4d + \bar{u})D_\pi^- + (4\bar{d} + u)D_\pi^+ + (s + \bar{s})D_s^\pi, \end{aligned} \quad (\text{C.5})$$

the explicit  $x$ ,  $z$ ,  $Q^2$  dependence has been left out to save space whenever not causing confusion. The semi-inclusive  $K^+$  and  $K^-$  cross sections are:

$$\begin{aligned} 9\sigma_p^{K^+} &= (4u + \bar{s})D_K^+ + (4\bar{u} + s)D_K^- + (d + \bar{d})D_d^K, \\ 9\sigma_p^{K^-} &= (4u + \bar{s})D_K^- + (4\bar{u} + s)D_K^+ + (d + \bar{d})D_d^K, \\ 9\sigma_n^{K^+} &= (4d + \bar{s})D_K^+ + (4\bar{d} + s)D_K^- + (u + \bar{u})D_d^K, \\ 9\sigma_n^{K^-} &= (4d + \bar{s})D_K^- + (4\bar{d} + s)D_K^+ + (u + \bar{u})D_d^K. \end{aligned} \quad (\text{C.6})$$

To obtain the spin-dependent cross sections ( $\Delta\sigma^h$ ), one replaces the unpolarized quark distributions  $q(x)$  in Eq. C.5 and C.6 with the quark polarization distributions  $\Delta q(x)$ .

### C.1.2 The asymmetries expressed in “fixed- $z$ purity”

For this experiment, due to the high statistics nature, we can afford to follow the HERMES analysis of “purity” method at every fixed  $z$ -bins instead of integrating over  $z$  to obtain spin-flavor decomposition, and scrutinizing the  $z$ -dependent behavior of the extracted parton distributions, as an extra systematic crosscheck.

With the “fixed- $z$  purity” method, we solve for five unknown quantities, taking the notation of  $(\Delta s + \Delta \bar{s})/(s + \bar{s}) = \Delta s/s$ ,

$$X = \{\Delta u/u, \Delta d/d, \Delta \bar{u}/\bar{u}, \Delta \bar{d}/\bar{d}, \Delta s/s\}$$

first for each kinematic bin of  $(x, Q^2, z)$  through measurements of asymmetries

$$A = \{A_{1n}, A_{1n}^{\pi^+}, A_{1n}^{\pi^-}, A_{1n}^{K^+}, A_{1n}^{K^-}\}$$

with linear relations of  $A = M \cdot X$ . Notice that for multiple  $z$ -bins corresponding to the same  $(x, Q^2)$ , the same inclusive asymmetry  $A_{1n}$  will be used. Once we have clearly verified the  $z$ -independency of the extracted polarized parton quantities  $X$ , we can solve the linear equations once again, combining data of all  $z$ -bin of the same  $(x, Q^2)$ .

We define the “fixed- $z$  purity” matrix elements  $M_{ij}$  as the linear coefficients in front of  $\Delta q/q$  in linear relations of  $A = M \cdot X$ , as defined in Eq. C.7. These coefficients ( $M_{ij}$ ) are obtained from the unpolarized parton distribution functions and the fragmentation function ratios. This experiment will have a somewhat lower statistics for SIDIS  $\pi^0$  production channel, relative to the charged pion channels, due to the lower efficiency of  $\pi^0 \rightarrow 2\gamma$  reconstruction by the SBS calorimeter. At this moment, we chose not to include  $\pi^0$  asymmetry data in “fixed- $z$ ” purity LO spin-flavor decomposition. On the other hand, we include the expected inclusive  $A_{1n}$  data points, they provide similar constrains to  $\Delta q/q$  as SIDIS  $\pi^0$  channel, but with higher available statistical precisions.

The double spin asymmetries,  $A_{1N}^h = \Delta\sigma^h/\sigma^h$  can be expressed at a fixed value of  $(x, Q^2, z)$ , we have:

$$\begin{aligned}
A_{1n} &= \frac{\Delta u + \Delta \bar{u} + 4(\Delta d + \Delta \bar{d}) + 2\Delta s}{u + \bar{u} + 4(d + \bar{d}) + 2s}, \\
A_{1n}^{\pi^+} &= \frac{4\Delta d + \Delta \bar{u} + (4\Delta \bar{d} + \Delta u) \lambda_\pi + 2\Delta s \xi_\pi}{4d + \bar{u} + (4\bar{d} + u) \lambda_\pi + 2s \xi_\pi}, \\
A_{1n}^{\pi^-} &= \frac{4\Delta \bar{d} + \Delta u + (4\Delta d + \Delta \bar{u}) \lambda_\pi + 2\Delta s \xi_\pi}{4\bar{d} + u + (4d + \bar{u}) \lambda_\pi + 2s \xi_\pi}, \\
A_{1n}^{K^+} &= \frac{4\Delta d + \Delta s + (4\Delta \bar{d} + \Delta s) \lambda_K + (\Delta u + \Delta \bar{u}) \xi_K}{4d + s + (4\bar{d} + s) \lambda_K + (u + \bar{u}) \xi_K}, \\
A_{1n}^{K^-} &= \frac{4\Delta \bar{d} + \Delta s + (4\Delta d + \Delta s) \lambda_K + (\Delta u + \Delta \bar{u}) \xi_K}{4\bar{d} + s + (4d + s) \lambda_K + (u + \bar{u}) \xi_K}.
\end{aligned} \tag{C.7}$$

where the fragmentation function ratios are defined as:

$$\begin{aligned}
\lambda_\pi(z) &= D_\pi^-(z)/D_\pi^+(z), & \xi_\pi(z) &= D_s^\pi(z)/D_\pi^+(z), \\
\lambda_K(z) &= D_K^-(z)/D_K^+(z), & \xi_K(z) &= D_d^K(z)/D_K^+(z).
\end{aligned} \tag{C.8}$$

Therefore, through Eq. C.7, we can read off matrix elements of  $M_{ij}$ , for example:

$$\begin{aligned}
M_{11} &= \frac{u}{u + \bar{u} + 4(d + \bar{d}) + 2s}, \\
M_{21} &= \frac{u \cdot \lambda_\pi}{4d + \bar{u} + (4\bar{d} + u) \lambda_\pi + 2s \xi_\pi}, \\
M_{31} &= \frac{u}{4\bar{d} + u + (4d + \bar{u}) \lambda_\pi + 2s \xi_\pi}, \\
M_{41} &= \frac{u \cdot \xi_K}{4d + s + (4\bar{d} + s) \lambda_K + (u + \bar{u}) \xi_K}, \\
M_{51} &= \frac{u \cdot \xi_K}{4\bar{d} + s + (4d + s) \lambda_K + (u + \bar{u}) \xi_K}, \text{ etc.}
\end{aligned} \tag{C.9}$$

## C.2 Systematic uncertainties in Chritova-Leader LO method introduced by SU(2) symmetry violations

This section was originally provided to PAC34 to address questions raised by Dr. N. Makins on systematic uncertainties introduced by SU(2) symmetry violations in fragmentation functions when extracting  $\Delta d_v - \frac{1}{4}\Delta u_v$  and  $\Delta u_v - \Delta d_v$ ,  $\Delta \bar{u} - \Delta \bar{d}$  when combined with (future) JLab-12 GeV proton target data.

Keeping all terms in leading-order, we have:

$$\begin{aligned}
9\sigma_p^{\pi^+} &= 4uD_u^{\pi^+} + \bar{d}D_d^{\pi^+} + dD_d^{\pi^+} + 4\bar{u}D_{\bar{u}}^{\pi^+} + (s + \bar{s})D_s^\pi, \\
9\sigma_p^{\pi^-} &= 4uD_u^{\pi^-} + \bar{d}D_d^{\pi^-} + dD_d^{\pi^-} + 4\bar{u}D_{\bar{u}}^{\pi^-} + (s + \bar{s})D_s^\pi, \\
9\sigma_n^{\pi^+} &= 4dD_u^{\pi^+} + \bar{u}D_{\bar{d}}^{\pi^+} + uD_d^{\pi^+} + 4\bar{d}D_{\bar{u}}^{\pi^+} + (s + \bar{s})D_s^\pi, \\
9\sigma_n^{\pi^-} &= 4dD_u^{\pi^-} + \bar{u}D_{\bar{d}}^{\pi^-} + uD_d^{\pi^-} + 4\bar{d}D_{\bar{u}}^{\pi^-} + (s + \bar{s})D_s^\pi.
\end{aligned} \tag{C.10}$$

Therefore, cross section differences of  $\pi^+ - \pi^-$  are:

$$\begin{aligned} 9\sigma_p^{\pi^+ - \pi^-} &= 4uD_u^{\pi^+ - \pi^-} + \bar{d}D_{\bar{d}}^{\pi^+ - \pi^-} + dD_d^{\pi^+ - \pi^-} + 4\bar{u}D_{\bar{u}}^{\pi^+ - \pi^-}, \\ 9\sigma_n^{\pi^+ - \pi^-} &= 4dD_u^{\pi^+ - \pi^-} + \bar{u}D_{\bar{d}}^{\pi^+ - \pi^-} + uD_d^{\pi^+ - \pi^-} + 4\bar{d}D_{\bar{u}}^{\pi^+ - \pi^-}. \end{aligned} \quad (\text{C.11})$$

Now we will be dealing with 4 flavor non-singlet fragmentation functions instead of 8 regular fragmentation functions. We will take two steps in accessing SU(2) violation in fragmentation functions.

### C.2.1 Case-1: only $u$ and $d$ fragmentation functions violate SU(2)

Assuming  $\bar{u}$  and  $\bar{d}$  fragmentation functions still respect SU(2) while  $u$  and  $d$ -quark fragmentation functions violate SU(2), i.e.:

$$\begin{aligned} D_{\bar{u}}^{\pi^+ - \pi^-} / D_u^{\pi^+ - \pi^-} &= -1, \\ D_{\bar{d}}^{\pi^+ - \pi^-} / D_d^{\pi^+ - \pi^-} &= -1, \\ D_d^{\pi^+ - \pi^-} / D_u^{\pi^+ - \pi^-} &= -1 + \epsilon_1. \end{aligned} \quad (\text{C.12})$$

$$\begin{aligned} 9\sigma_p^{\pi^+ - \pi^-} &= 4(u - \bar{u})D_u^{\pi^+ - \pi^-} + (d - \bar{d})D_d^{\pi^+ - \pi^-} = 4u_v D_u^{\pi^+ - \pi^-} + d_v D_d^{\pi^+ - \pi^-}, \\ 9\sigma_n^{\pi^+ - \pi^-} &= 4d_v D_u^{\pi^+ - \pi^-} + u_v D_d^{\pi^+ - \pi^-}, \\ 9\sigma_{2p+n}^{\pi^+ - \pi^-} &= (8u_v + 4d_v)D_u^{\pi^+ - \pi^-} + (u_v + 2d_v)D_d^{\pi^+ - \pi^-}. \end{aligned} \quad (\text{C.13})$$

$$A_{1p}^{\pi^+ - \pi^-}(\vec{p}) = \frac{\Delta\sigma_p^{\pi^+} - \Delta\sigma_p^{\pi^-}}{\sigma_p^{\pi^+} - \sigma_p^{\pi^-}} = \frac{4\Delta u_v - \Delta d_v + \epsilon_1 \Delta d_v}{4u_v - d_v + \epsilon_1 d_v}, \quad (\text{C.14})$$

$$A_{1He}^{\pi^+ - \pi^-}(\vec{n} + 2\vec{p}) = \frac{\Delta\sigma_{He}^{\pi^+} - \Delta\sigma_{He}^{\pi^-}}{\sigma_{He}^{\pi^+} - \sigma_{He}^{\pi^-}} = \frac{4\Delta d_v - \Delta u_v + \epsilon_1 \Delta u_v}{7u_v + 2d_v + \epsilon_1(u_v + 2d_v)}. \quad (\text{C.15})$$

Assuming a large SU(2) violation  $\epsilon_1 = \pm 5\%$ , from Eq. C.15 the fact that  $\epsilon_1 \neq 0$  has the following impacts to this experiment. First, the asymmetry  $A_{1He}^{\pi^+ - \pi^-}$  has a relative change of  $\epsilon_1(u_v + 2d_v)/(7u_v + 2d_v) \approx \frac{1}{4}\epsilon_1 \approx \pm 1.25\%$ , which is negligible. Second, the extracted value of  $x(\Delta d_v - \frac{1}{4}\Delta u_v)$  has an offset of  $\frac{\epsilon_1}{4}x\Delta u_v$ . Recall that  $x\Delta u_v \leq 0.3$ , therefore, the offset becomes  $\frac{\epsilon_1}{4}x\Delta u_v \leq 0.3\epsilon_1/4 \approx \pm 0.004$ .

### C.2.2 Case-12: only $\bar{u}$ and $\bar{d}$ fragmentation functions violate SU(2)

Assuming  $\bar{u}$  and  $\bar{d}$  fragmentation functions violate SU(2) while  $u$  and  $d$ -quark fragmentation functions do not, i.e.:

$$\begin{aligned} D_{\bar{u}}^{\pi^+ - \pi^-} / D_u^{\pi^+ - \pi^-} &= -1 + \epsilon_2, \\ D_{\bar{d}}^{\pi^+ - \pi^-} / D_d^{\pi^+ - \pi^-} &= -1 + \epsilon_3, \\ D_d^{\pi^+ - \pi^-} / D_u^{\pi^+ - \pi^-} &= -1. \end{aligned} \quad (\text{C.16})$$

$$\begin{aligned}
9\sigma_p^{\pi^+-\pi^-} &= (4u_v - d_v)D_u^{\pi^+-\pi^-} + (4\bar{u}\epsilon_2 - \bar{d}\epsilon_3)D_u^{\pi^+-\pi^-}, \\
9\sigma_n^{\pi^+-\pi^-} &= (4d_v - u_v)D_u^{\pi^+-\pi^-} + (4\bar{d}\epsilon_2 - \bar{u}\epsilon_3)D_u^{\pi^+-\pi^-}, \\
9\sigma_{2p+n}^{\pi^+-\pi^-} &= (7u_v + 2d_v)D_u^{\pi^+-\pi^-} + (7\bar{u}\epsilon_2 + 2\bar{d}\epsilon_3)D_u^{\pi^+-\pi^-}.
\end{aligned} \tag{C.17}$$

$$A_{1p}^{\pi^+-\pi^-}(\vec{p}) = \frac{\Delta\sigma_p^{\pi^+} - \Delta\sigma_p^{\pi^-}}{\sigma_p^{\pi^+} - \sigma_p^{\pi^-}} = \frac{4\Delta u_v - \Delta d_v + 4\Delta \bar{u}\epsilon_2 - \Delta \bar{d}\epsilon_3}{4u_v - d_v + 4\bar{u}\epsilon_2 - \bar{d}\epsilon_3}, \tag{C.18}$$

$$A_{1He}^{\pi^+-\pi^-}(\vec{n} + 2\vec{p}) = \frac{\Delta\sigma_{He}^{\pi^+} - \Delta\sigma_{He}^{\pi^-}}{\sigma_{He}^{\pi^+} - \sigma_{He}^{\pi^-}} = \frac{4\Delta d_v - \Delta u_v + 4\Delta \bar{d}\epsilon_2 - \Delta \bar{u}\epsilon_3}{7u_v + 2d_v + 7\bar{u}\epsilon_2 + 2\bar{d}\epsilon_3}. \tag{C.19}$$

Noticed that all terms realted to  $\epsilon_2$  and  $\epsilon_3$  are associated with sea quark densities. Again, assuming a large SU(2) violation  $\epsilon_2 = \pm 10\%$ ,  $\epsilon_3 = \pm 10\%$ , from Eq. C.19 the fact that  $\epsilon_2 \neq 0$  and  $\epsilon_3 \neq 0$  has the following impacts to this experiment. First, the asymmetry  $A_{1He}^{\pi^+-\pi^-}$  has a relative change of  $(7\epsilon_2\bar{u} + 2\epsilon_3\bar{d})/(7u_v + 2d_v) \ll \pm 3\%$ , which is negligible. Second, the extracted value of  $x(\Delta d_v - \frac{1}{4}\Delta u_v)$  has an offset of  $\epsilon_2 x \Delta \bar{d} - \frac{\epsilon_3}{4} x \Delta \bar{u}$ , which is about  $0.1x\Delta \bar{d}$ , rather small compared with statistical uncertainties of this experiment.

Recall that:

$$[\Delta \bar{u}(x) - \Delta \bar{d}(x)]_{LO} = 3[g_1^p(x) - g_1^n(x)] - \frac{1}{2}(\Delta u_v - \Delta d_v)|_{LO}. \tag{C.20}$$

For  $\epsilon_2 = \pm 10\%$ ,  $\epsilon_3 = \pm 10\%$ , it will introduce  $5\% \sim 8\%$  relative uncertainties to  $\Delta \bar{u} - \Delta \bar{d}$ .

## Appendix D

# Projected Results of SIDIS Asymmetries on ${}^3\text{He}$ and Neutron

The figures in this section show the projected statistical asymmetry uncertainties  $\Delta A_{1n}^h$  for five hadron species ( $\pi^+$ ,  $\pi^-$ ,  $\pi^0$ ,  $K^+$ ,  $K^-$ ) at 11 and 8.8 GeV beam energies in two-dimensional ( $x, z$ ) bins. For more details including numerical tables of projected asymmetry uncertainties and numbers of events for 1D, 2D and 3D kinematic binning, see [53].

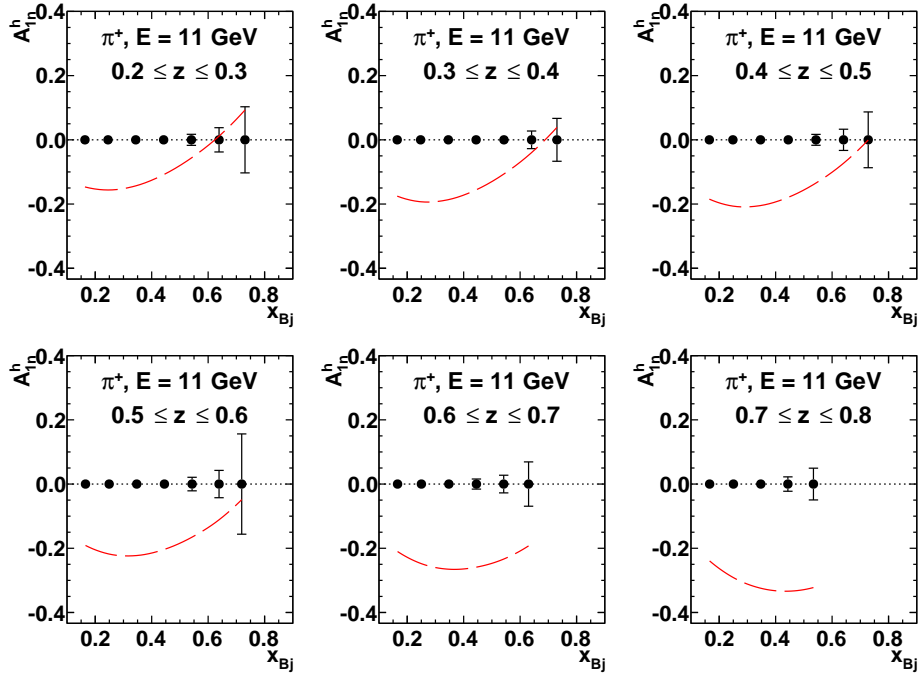


Figure D.1: Projected uncertainties in  $A_{1n}^{\pi^+}(x, z)$  from combined 11 GeV running at both SBS angle settings, compared to the predictions of the recent NLO global QCD analysis of DSSV [45]

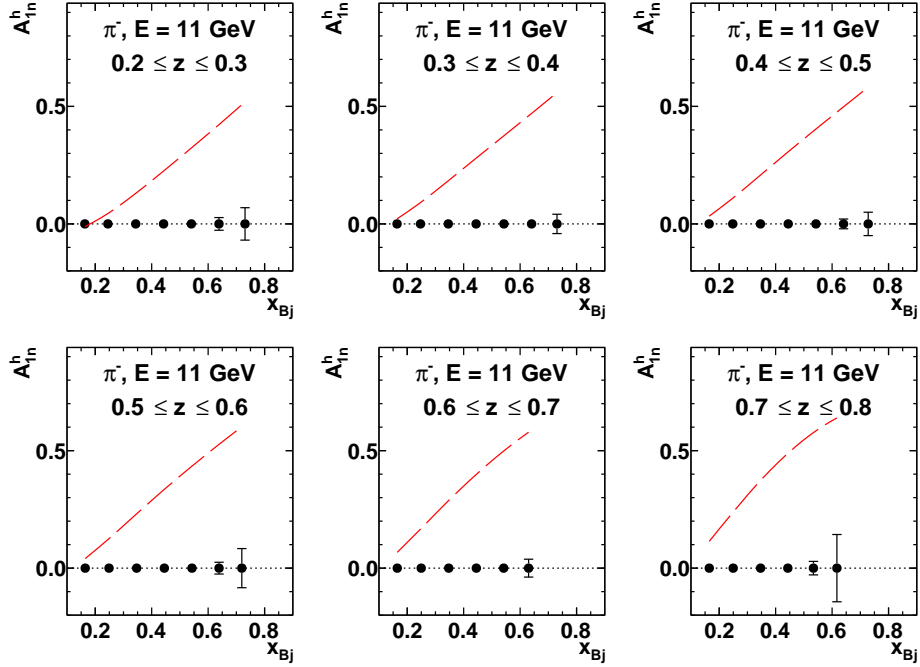


Figure D.2: Projected uncertainties in  $A_{1n}^{\pi^-}(x, z)$  from combined 11 GeV running at both SBS angle settings, compared to the predictions of the recent NLO global QCD analysis of DSSV [45]

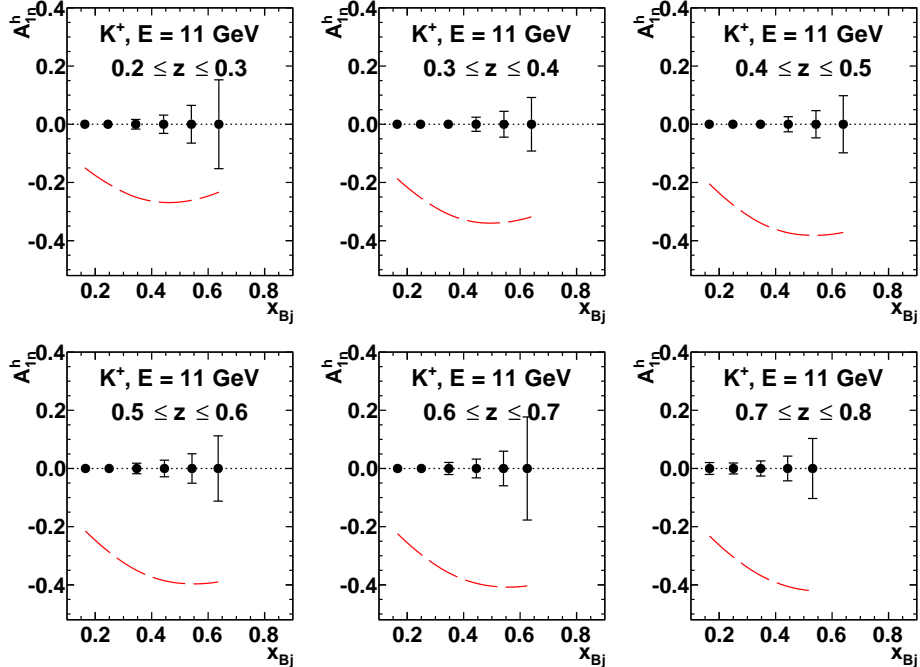


Figure D.3: Projected uncertainties in  $A_{1n}^{K^+}(x, z)$  from combined 11 GeV running at both SBS angle settings, compared to the predictions of the recent NLO global QCD analysis of DSSV [45]

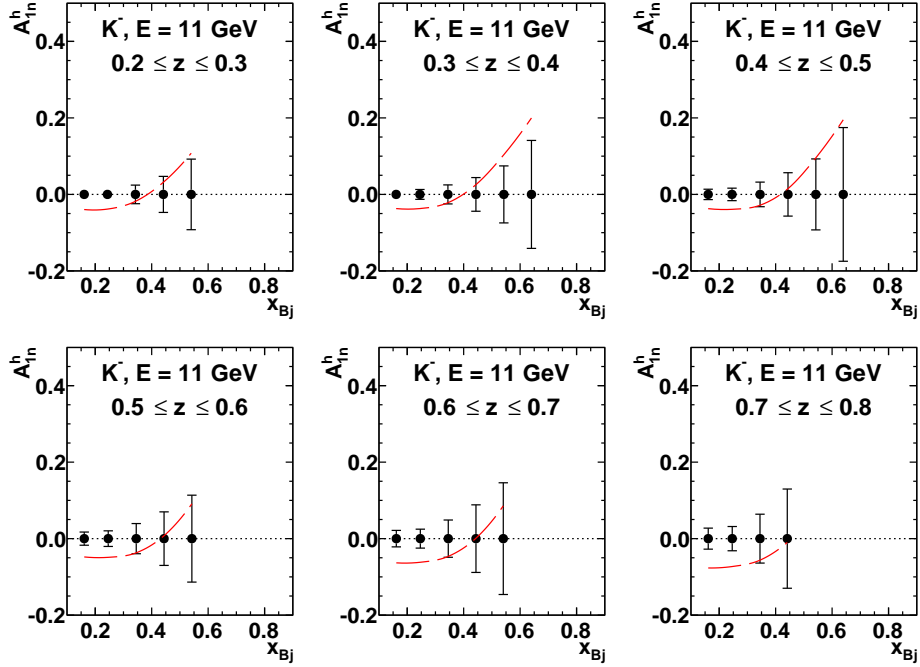


Figure D.4: Projected uncertainties in  $A_{1n}^{K^-}(x, z)$  from combined 11 GeV running at both SBS angle settings, compared to the predictions of the recent NLO global QCD analysis of DSSV [45]

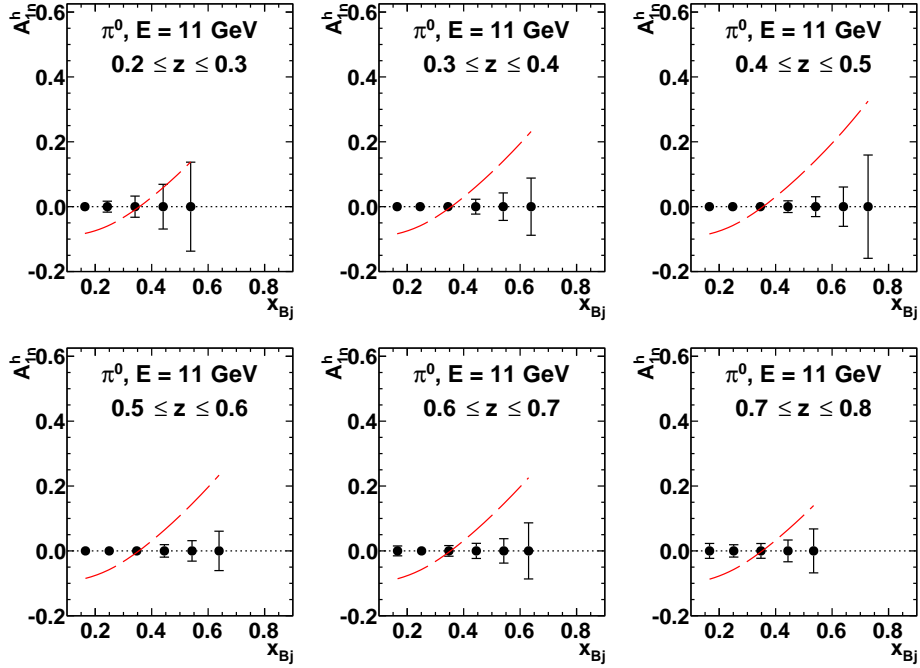


Figure D.5: Projected uncertainties in  $A_{1n}^{\pi^0}(x, z)$  from combined 11 GeV running at both SBS angle settings, compared to the predictions of the recent NLO global QCD analysis of DSSV [45]

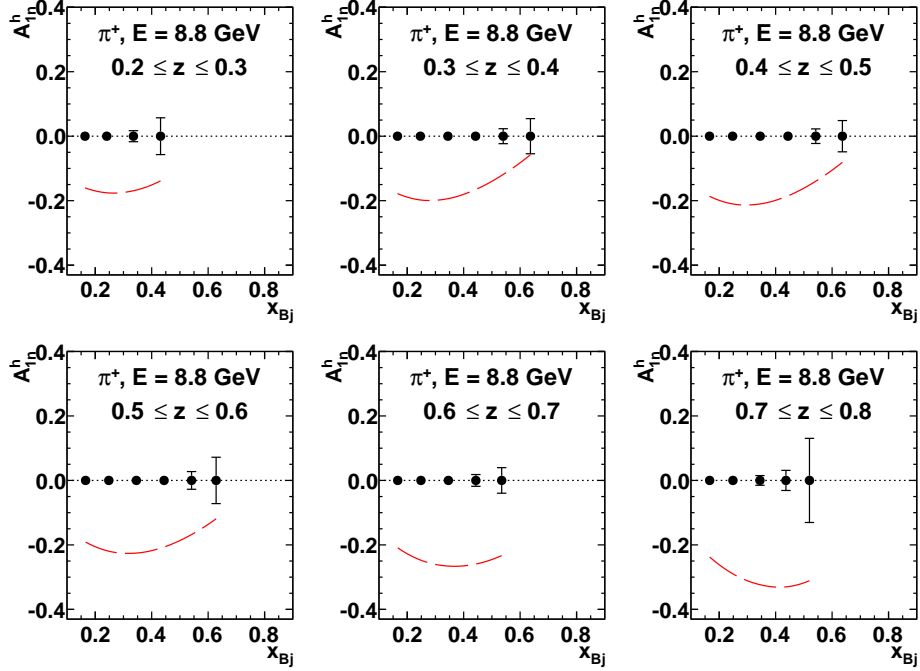


Figure D.6: Projected uncertainties in  $A_{1n}^{\pi^+}(x, z)$  from combined 8.8 GeV running at both SBS angle settings, compared to the predictions of the recent NLO global QCD analysis of DSSV [45]

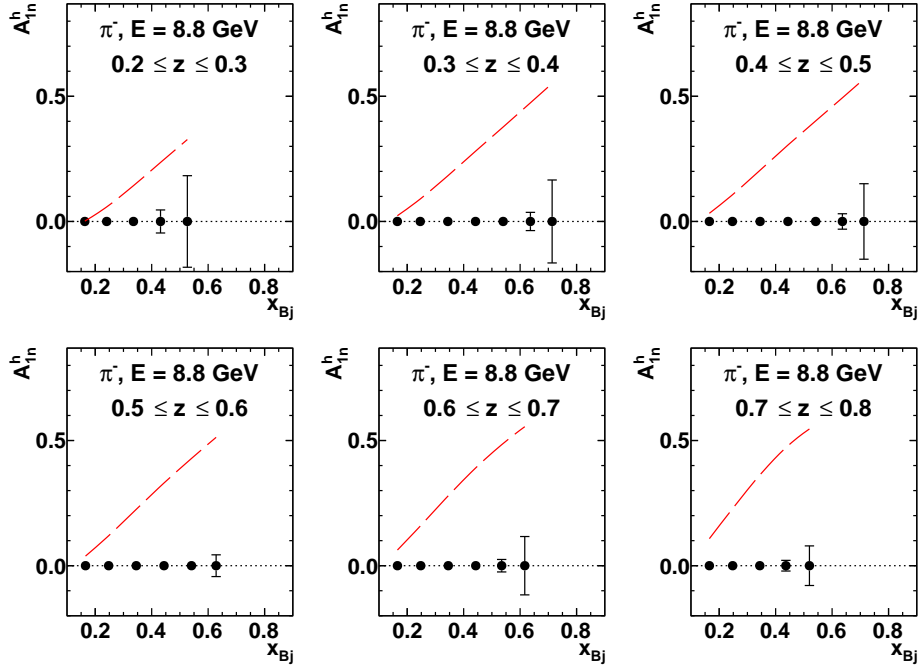


Figure D.7: Projected uncertainties in  $A_{1n}^{\pi^-}(x, z)$  from combined 8.8 GeV running at both SBS angle settings, compared to the predictions of the recent NLO global QCD analysis of DSSV [45]

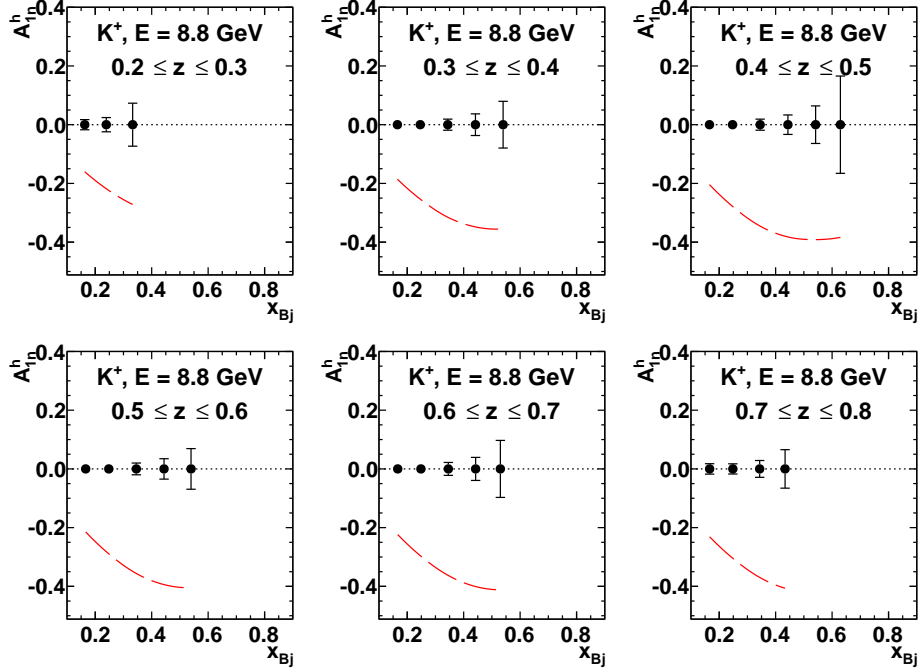


Figure D.8: Projected uncertainties in  $A_{1n}^{K^+}(x, z)$  from combined 8.8 GeV running at both SBS angle settings, compared to the predictions of the recent NLO global QCD analysis of DSSV [45]

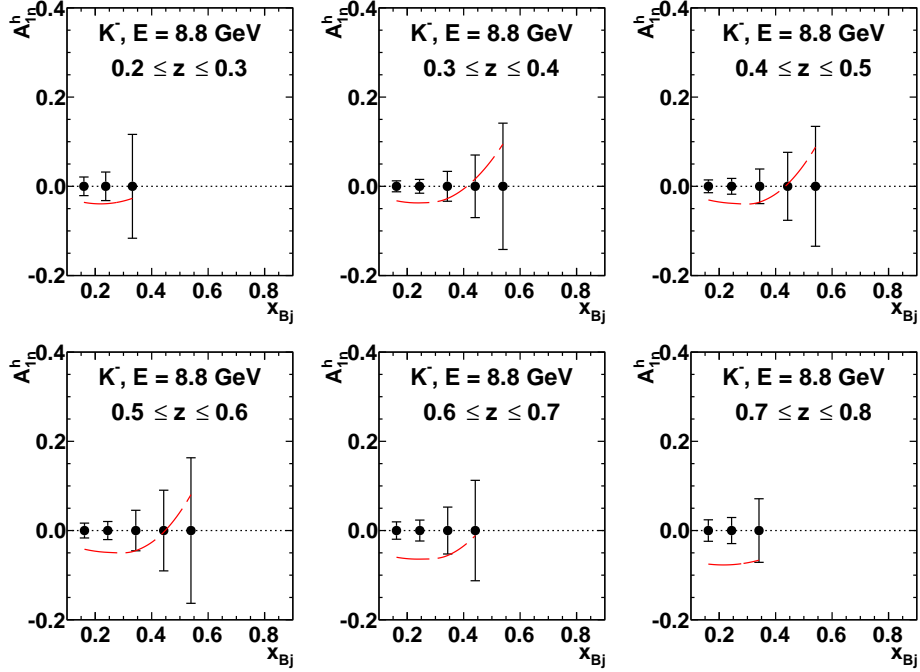


Figure D.9: Projected uncertainties in  $A_{1n}^{K^-}(x, z)$  from combined 8.8 GeV running at both SBS angle settings, compared to the predictions of the recent NLO global QCD analysis of DSSV [45]

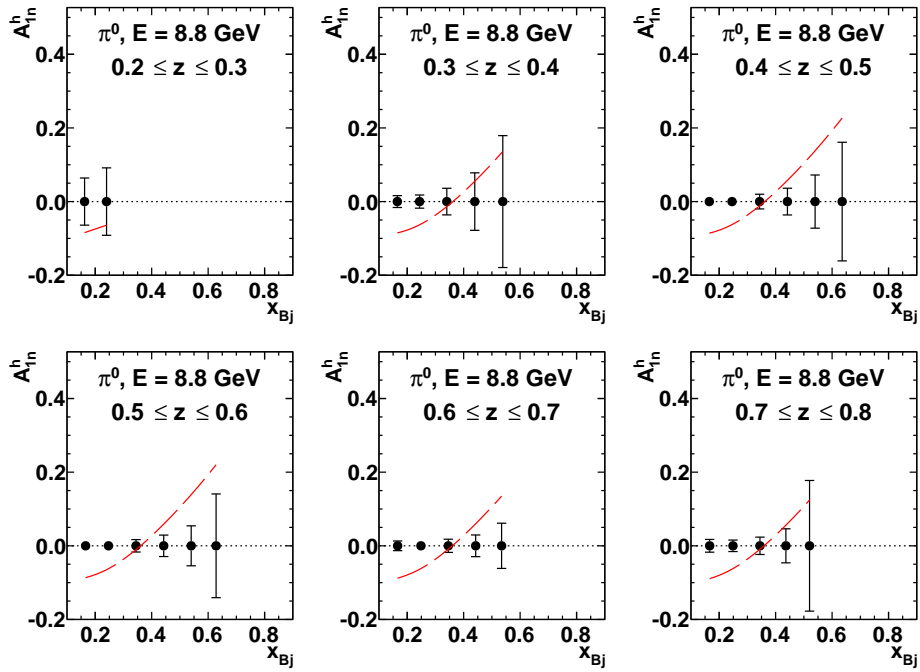


Figure D.10: Projected uncertainties in  $A_{1n}^{\pi^0}(x, z)$  from combined 8.8 GeV running at both SBS angle settings, compared to the predictions of the recent NLO global QCD analysis of DSSV [45]

## Appendix E

# Projected Results of LO Spin-Flavor Decomposition

### E.1 Statistical Uncertainties of LO Christova-Leader Method of Spin-Flavor Decomposition

$\langle x \rangle$	$\langle Q^2 \rangle$	$xu_v$	$xd_v$	$\langle z \rangle$	$\delta \left( A_{^{1}He}^{\pi^+ - \pi^-} \right)$	$\delta [x(\Delta d_v - \frac{1}{4}\Delta u_v)]_{CL}$
		GeV <sup>2</sup>			%	
0.165	3.22	0.657	0.317	0.249	0.52	0.0078
				0.345	0.49	0.0074
				0.444	0.56	0.0084
				0.545	0.65	0.0099
				0.646	0.80	0.0121
				0.747	1.05	0.0159
0.245	4.51	0.647	0.275	0.254	0.43	0.0064
				0.346	0.38	0.0056
				0.445	0.41	0.0060
				0.546	0.47	0.0068
				0.645	0.55	0.0081
				0.743	0.69	0.0101
0.343	5.95	0.519	0.188	0.260	0.59	0.0069
				0.346	0.48	0.0055
				0.446	0.49	0.0056
				0.546	0.52	0.0059
				0.646	0.60	0.0069
				0.744	0.73	0.0084
0.443	7.30	0.349	0.105	0.266	0.89	0.0068
				0.348	0.65	0.0049
				0.446	0.64	0.0048
				0.547	0.67	0.0051
				0.646	0.76	0.0058
				0.740	0.98	0.0074
0.541	8.50	0.199	0.049	0.271	1.51	0.0065
				0.347	0.96	0.0041
				0.446	0.95	0.0041
				0.547	1.00	0.0042
				0.643	1.14	0.0048
				0.733	1.89	0.0086
0.640	9.60	0.091	0.018	0.276	2.82	0.0055
				0.348	1.63	0.0032
				0.447	1.58	0.0030
				0.546	1.70	0.0033
				0.637	2.37	0.0051
0.730	10.77	0.034	0.005	0.278	6.68	0.0048
				0.348	3.50	0.0025
				0.445	3.62	0.0026
				0.534	5.48	0.0044

Table E.1: For  $E_0 = 11.0$  GeV. The expected statistical uncertainties of  $A_{^{1}He}^{\pi^+ - \pi^-}$  and extracted valence quark polarization  $\delta [x(\Delta d_v - \frac{1}{4}\Delta u_v)]_{CL}$  according to leading order Christova-Leader (CL) method.

$\langle x \rangle$	$\langle Q^2 \rangle$	$xu_v$	$xd_v$	$\langle z \rangle$	$\delta \left( A_{1He}^{\pi^+ - \pi^-} \right)$	$\delta [x(\Delta d_v - \frac{1}{4}\Delta u_v)]_{CL}$
GeV <sup>2</sup>					%	
0.161	2.47	0.660	0.323	0.281	1.00	0.0153
				0.349	0.56	0.0086
				0.447	0.56	0.0085
				0.548	0.62	0.0095
				0.645	0.69	0.0106
				0.744	0.85	0.0131
0.241	3.43	0.666	0.286	0.285	0.94	0.0143
				0.348	0.44	0.0066
				0.446	0.44	0.0066
				0.547	0.47	0.0070
				0.646	0.51	0.0077
				0.744	0.63	0.0094
0.334	4.47	0.552	0.204	0.289	1.89	0.0234
				0.350	0.59	0.0070
				0.448	0.55	0.0066
				0.547	0.56	0.0067
				0.646	0.62	0.0074
				0.742	0.78	0.0093
0.433	5.59	0.381	0.118	0.294	5.41	0.0453
				0.355	0.88	0.0071
				0.447	0.80	0.0064
				0.547	0.79	0.0063
				0.646	0.88	0.0071
				0.731	1.33	0.0110
0.541	6.39	0.211	0.052	0.360	1.56	0.0071
				0.448	1.26	0.0058
				0.548	1.26	0.0058
				0.639	1.65	0.0078
				0.717	5.51	0.0284
0.637	7.25	0.100	0.020	0.366	3.18	0.0068
				0.446	2.32	0.0050
				0.540	2.93	0.0068
0.714	8.33	0.044	0.007	0.368	12.49	0.0117

Table E.2: For  $E_0 = 8.8$  GeV. The expected statistical uncertainties of the combined asymmetry  $A_{1He}^{\pi^+ - \pi^-}$  and extracted valence quark polarization  $\delta [x(\Delta d_v - \frac{1}{4}\Delta u_v)]_{CL}$  according to the leading order Christova-Leader (CL) method. Values of  $xu_v$  and  $xd_v$  from CTEQ leading order are also listed.

## References

- [1] Johannes Blumlein and Helmut Bottcher. QCD Analysis of Polarized Deep Inelastic Scattering Data. *Nucl.Phys.*, B841:205–230, 2010. [arXiv:1005.3113](https://arxiv.org/abs/1005.3113), doi:[10.1016/j.nuclphysb.2010.08.005](https://doi.org/10.1016/j.nuclphysb.2010.08.005).
- [2] B. Adeva et al. Polarized quark distributions in the nucleon from semiinclusive spin asymmetries. *Phys.Lett.*, B420:180–190, 1998. [arXiv:hep-ex/9711008](https://arxiv.org/abs/hep-ex/9711008), doi:[10.1016/S0370-2693\(97\)01546-3](https://doi.org/10.1016/S0370-2693(97)01546-3).
- [3] A. Airapetian et al. Quark helicity distributions in the nucleon for up, down, and strange quarks from semi-inclusive deep-inelastic scattering. *Phys.Rev.*, D71:012003, 2005. [arXiv:hep-ex/0407032](https://arxiv.org/abs/hep-ex/0407032), doi:[10.1103/PhysRevD.71.012003](https://doi.org/10.1103/PhysRevD.71.012003).
- [4] M.G. Alekseev et al. Quark helicity distributions from longitudinal spin asymmetries in muon-proton and muon-deuteron scattering. *Phys.Lett.*, B693:227–235, 2010. [arXiv:1007.4061](https://arxiv.org/abs/1007.4061), doi:[10.1016/j.physletb.2010.08.034](https://doi.org/10.1016/j.physletb.2010.08.034).
- [5] Elliot Leader, Aleksander V. Sidorov, and Dimiter B. Stamenov. Determination of Polarized PDFs from a QCD Analysis of Inclusive and Semi-inclusive Deep Inelastic Scattering Data. *Phys.Rev.*, D82:114018, 2010. [arXiv:1010.0574](https://arxiv.org/abs/1010.0574), doi:[10.1103/PhysRevD.82.114018](https://doi.org/10.1103/PhysRevD.82.114018).
- [6] M. Hirai and S. Kumano. Determination of gluon polarization from deep inelastic scattering and collider data. *Nucl.Phys.*, B813:106–122, 2009. [arXiv:0808.0413](https://arxiv.org/abs/0808.0413), doi:[10.1016/j.nuclphysb.2008.12.026](https://doi.org/10.1016/j.nuclphysb.2008.12.026).
- [7] Daniel de Florian, Rodolfo Sassot, Marco Stratmann, and Werner Vogelsang. Global analysis of helicity parton densities and their uncertainties. *Phys. Rev. Lett.*, 101:072001, Aug 2008. URL: <http://link.aps.org/doi/10.1103/PhysRevLett.101.072001>, doi:[10.1103/PhysRevLett.101.072001](https://doi.org/10.1103/PhysRevLett.101.072001).
- [8] L. Adamczyk et al. Measurement of longitudinal spin asymmetries for weak boson production in polarized proton-proton collisions at RHIC. 2014. [arXiv:1404.6880](https://arxiv.org/abs/1404.6880).
- [9] Claude Bourrely, Jacques Soffer, and Franco Buccella. Strangeness asymmetry of the nucleon in the statistical parton model. *Physics Letters B*, 648(1):39 – 45, 2007. URL: <http://www.sciencedirect.com/science/article/pii/S037026930700295X>, doi: <http://dx.doi.org/10.1016/j.physletb.2007.02.063>.
- [10] Claude Bourrely, Franco Buccella, and Jacques Soffer. bosons production in the quantum statistical parton distributions approach. *Physics Letters B*, 726(13):296 – 299, 2013. URL: <http://www.sciencedirect.com/science/article/pii/S0370269313006849>, doi:<http://dx.doi.org/10.1016/j.physletb.2013.08.045>.

- [11] Xiang-dong Ji, Jian-ping Ma, and Feng Yuan. QCD factorization for semi-inclusive deep-inelastic scattering at low transverse momentum. *Phys.Rev.*, D71:034005, 2005. [arXiv:hep-ph/0404183](#), doi:10.1103/PhysRevD.71.034005.
- [12] Xiang-dong Ji, Jian-Ping Ma, and Feng Yuan. QCD factorization for spin-dependent cross sections in DIS and Drell-Yan processes at low transverse momentum. *Phys.Lett.*, B597:299–308, 2004. [arXiv:hep-ph/0405085](#), doi:10.1016/j.physletb.2004.07.026.
- [13] T. Navasardyan, G.S. Adams, A. Ahmidouch, T. Angelescu, J. Arrington, et al. The Onset of Quark-Hadron Duality in Pion Electroproduction. *Phys.Rev.Lett.*, 98:022001, 2007. [arXiv:hep-ph/0608214](#), doi:10.1103/PhysRevLett.98.022001.
- [14] R. Asaturyan, R. Ent, H. Mkrtchyan, T. Navasardyan, V. Tadevosyan, et al. Semi-Inclusive Charged-Pion Electroproduction off Protons and Deuterons: Cross Sections, Ratios and Access to the Quark-Parton Model at Low Energies. *Phys.Rev.*, C85:015202, 2012. [arXiv:1103.1649](#), doi:10.1103/PhysRevC.85.015202.
- [15] Leonid L. Frankfurt, Mark I. Strikman, Lech Mankiewicz, Andreas Schfer, Ewa Rondio, Andrzej Sandacz, and Vassilios Papavassiliou. The valence and strange-sea quark spin distributions in the nucleon from semi-inclusive deep inelastic lepton scattering. *Physics Letters B*, 230(12):141 – 148, 1989. URL: <http://www.sciencedirect.com/science/article/pii/0370269389916687>, doi:[http://dx.doi.org/10.1016/0370-2693\(89\)91668-7](http://dx.doi.org/10.1016/0370-2693(89)91668-7).
- [16] F. E. Close and R. G. Milner. Probing the polarized sea by inclusive leptoproduction of hadrons. *Phys. Rev. D*, 44:3691–3694, Dec 1991. URL: <http://link.aps.org/doi/10.1103/PhysRevD.44.3691>, doi:10.1103/PhysRevD.44.3691.
- [17] Ekaterina Christova and Elliot Leader. Semiinclusive pi+- scattering: Tests for independent fragmentation and for polarized quark densities. *Phys.Lett.*, B468:299–303, 1999. [arXiv:hep-ph/9907265](#), doi:10.1016/S0370-2693(99)01213-7.
- [18] Ekaterina Christova and Elliot Leader. A Strategy for the analysis of semiinclusive deep inelastic scattering. *Nucl.Phys.*, B607:369–390, 2001. [arXiv:hep-ph/0007303](#), doi:10.1016/S0550-3213(01)00244-9.
- [19] E. A. Hawker, T. C. Awes, M. E. Beddo, C. N. Brown, J. D. Bush, T. A. Carey, T. H. Chang, W. E. Cooper, C. A. Gagliardi, G. T. Garvey, D. F. Geesaman, X. C. He, L. D. Isenhower, S. B. Kaufman, D. M. Kaplan, P. N. Kirk, D. D. Koetke, G. Kyle, D. M. Lee, W. M. Lee, M. J. Leitch, N. Makins, P. L. McGaughey, J. M. Moss, B. A. Mueller, P. M. Nord, B. K. Park, V. Papavassiliou, J. C. Peng, G. Petitt, P. E. Reimer, M. E. Sadler, J. Selden, P. W. Stankus, W. E. Sondheim, T. N. Thompson, R. S. Towell, R. E. Tribble, M. A. Vasiliev, Y. C. Wang, Z. F. Wang, J. C. Webb, J. L. Willis, D. K. Wise, and G. R. Young. Measurement of the light antiquark flavor asymmetry in the nucleon sea. *Phys. Rev. Lett.*, 80:3715–3718, Apr 1998. URL: <http://link.aps.org/doi/10.1103/PhysRevLett.80.3715>, doi:10.1103/PhysRevLett.80.3715.
- [20] J.C. Peng et al. Anti-d / anti-u asymmetry and the origin of the nucleon sea. *Phys.Rev.*, D58:092004, 1998. [arXiv:hep-ph/9804288](#), doi:10.1103/PhysRevD.58.092004.
- [21] X. Jiang, G.A. Navarro, and R. Sassot. Sea quark polarization and semi-inclusive DIS data. *Eur.Phys.J.*, C47:81–85, 2006. [arXiv:hep-ph/0602236](#), doi:10.1140/epjc/s2006-02525-7.

- [22] D.J.J.de Lange et al. The optical properties of the bigbite spectrometer at {NIKHEF}. *Nuclear Instruments and Methods in Physics Research Section A: Accelerators, Spectrometers, Detectors and Associated Equipment*, 412(23):254 – 264, 1998. URL: <http://www.sciencedirect.com/science/article/pii/S0168900298004768>, doi: [http://dx.doi.org/10.1016/S0168-9002\(98\)00476-8](http://dx.doi.org/10.1016/S0168-9002(98)00476-8).
- [23] D.J.J de Lange, J.J.M Steijger, H de Vries, M Anghinolfi, M Taiuti, D.W Higinbotham, B.E Norum, and E Konstantinov. A large acceptance spectrometer for the internal target facility at {NIKHEF}. *Nuclear Instruments and Methods in Physics Research Section A: Accelerators, Spectrometers, Detectors and Associated Equipment*, 406(2):182 – 194, 1998. URL: <http://www.sciencedirect.com/science/article/pii/S0168900298919817>, doi:[http://dx.doi.org/10.1016/S0168-9002\(98\)91981-7](http://dx.doi.org/10.1016/S0168-9002(98)91981-7).
- [24] M. Mihovilovi et al. Methods for optical calibration of the bigbite hadron spectrometer. *Nuclear Instruments and Methods in Physics Research Section A: Accelerators, Spectrometers, Detectors and Associated Equipment*, 686(0):20 – 30, 2012. URL: <http://www.sciencedirect.com/science/article/pii/S0168900212004901>, doi: <http://dx.doi.org/10.1016/j.nima.2012.04.085>.
- [25] J. J. LeRose, B. Wojtsekowski, et al. The Super-Bigbite Spectrometer for Jefferson Lab Hall A. <https://userweb.jlab.org/%7Ebogdanw/SBS-CDR/SBS-CDR.pdf>, 2009.
- [26] J. J. LeRose, B. Wojtsekowski, et al. The Super-Bigbite Spectrometer for Jefferson Lab Hall A. [https://userweb.jlab.org/~mahbub/HallA/SBS/SBS-CDR\\_New.pdf](https://userweb.jlab.org/~mahbub/HallA/SBS/SBS-CDR_New.pdf), 2010.
- [27] G. Cates, E. Cisbani, G. Franklin, A. Puckett, B. Wojtsekowski, et al. Target Single-Spin Asymmetries in Semi-Inclusive Pion and Kaon Electroproduction on a Transversely Polarized  $^3\text{He}$  Target using Super BigBite and BigBite in Hall A. [http://www.jlab.org/exp\\_prog/PACpage/PAC38/proposals/Conditionally%20Approved/C12-09-018\\_Update.pdf](http://www.jlab.org/exp_prog/PACpage/PAC38/proposals/Conditionally%20Approved/C12-09-018_Update.pdf), 2011.
- [28] P.A.M. Dolph, J. Singh, T. Averett, A. Kelleher, K.E. Mooney, et al. Gas dynamics in high-luminosity polarized He-3 targets using diffusion and convection. *Phys.Rev.*, C84:065201, 2011. [arXiv:1107.1902](https://arxiv.org/abs/1107.1902), doi:[10.1103/PhysRevC.84.065201](https://doi.org/10.1103/PhysRevC.84.065201).
- [29] G. Cates, S. Riordan, B. Wojtsekowski, et al. Measurement of the Neutron Electromagnetic Form Factor Ratio  $G_E^n/G_M^n$  at High  $Q^2$ . <http://hallaweb.jlab.org/collab/PAC/PAC34/PR-09-016-gen.pdf>, 2009.
- [30] X. Qian et al. Single spin asymmetries in charged pion production from semi-inclusive deep inelastic scattering on a transversely polarized  $^3\text{He}$  target at  $Q^2 = 1.4\text{--}2.7 \text{ gev}^2$ . *Phys. Rev. Lett.*, 107:072003, Aug 2011. URL: <http://link.aps.org/doi/10.1103/PhysRevLett.107.072003>, doi:[10.1103/PhysRevLett.107.072003](https://doi.org/10.1103/PhysRevLett.107.072003).
- [31] S. Riordan et al. Measurements of the electric form factor of the neutron up to  $q^2 = 3.4 \text{ gev}^2$  using the reaction  $^3\text{he}[\text{over}\rightarrow](e[\text{over}\rightarrow], e'n)\text{pp}$ . *Phys. Rev. Lett.*, 105(26):262302, Dec 2010. doi:[10.1103/PhysRevLett.105.262302](https://doi.org/10.1103/PhysRevLett.105.262302).
- [32] F. Sauli. Gem: A new concept for electron amplification in gas detectors. *Nuclear Instruments and Methods in Physics Research Section A: Accelerators, Spectrometers, Detectors and Associated Equipment*, 386(23):531 – 534, 1997. URL: <http://www.sciencedirect.com/science/article/pii/S0168900296011722>, doi:[http://dx.doi.org/10.1016/S0168-9002\(96\)01172-2](http://dx.doi.org/10.1016/S0168-9002(96)01172-2).

- [33] A Bressan, J.C Labb, P Pagano, L Ropelewski, and F Sauli. Beam tests of the gas electron multiplier. *Nuclear Instruments and Methods in Physics Research Section A: Accelerators, Spectrometers, Detectors and Associated Equipment*, 425(12):262 – 276, 1999. URL: <http://www.sciencedirect.com/science/article/pii/S0168900298014065>, doi: [http://dx.doi.org/10.1016/S0168-9002\(98\)01406-5](http://dx.doi.org/10.1016/S0168-9002(98)01406-5).
- [34] E. Brash, E. Cisbani, M. Jones, M. Khandaker, L. Pentchev, C. F. Perdrisat, V. Punjabi, B. Wojtsekhowski, et al. Large Acceptance Proton Form Factor Ratio Measurements at 13 and 15 GeV<sup>2</sup> Using Recoil Polarization Method. [http://www.jlab.org/exp\\_prog/proposals/07/PR12-07-109.pdf](http://www.jlab.org/exp_prog/proposals/07/PR12-07-109.pdf), 2007.
- [35] N.V. Vlasov et al. A calorimeter for detecting hadrons with energies of 10100 gev. *Instruments and Experimental Techniques*, 49(1):41–55, 2006. URL: <http://dx.doi.org/10.1134/S0020441206010040>, doi:10.1134/S0020441206010040.
- [36] N Akopov et al. The {HERMES} dual-radiator ring imaging cherenkov detector. *Nuclear Instruments and Methods in Physics Research Section A: Accelerators, Spectrometers, Detectors and Associated Equipment*, 479(23):511 – 530, 2002. URL: <http://www.sciencedirect.com/science/article/pii/S0168900201009329>, doi: [http://dx.doi.org/10.1016/S0168-9002\(01\)00932-9](http://dx.doi.org/10.1016/S0168-9002(01)00932-9).
- [37] S. Agostinelli et al. Geant4a simulation toolkit. *Nuclear Instruments and Methods in Physics Research Section A: Accelerators, Spectrometers, Detectors and Associated Equipment*, 506(3):250 – 303, 2003. URL: <http://www.sciencedirect.com/science/article/pii/S0168900203013688>, doi:[http://dx.doi.org/10.1016/S0168-9002\(03\)01368-8](http://dx.doi.org/10.1016/S0168-9002(03)01368-8).
- [38] W.K. Tung, H.L. Lai, A. Belyaev, J. Pumplin, D. Stump, et al. Heavy Quark Mass Effects in Deep Inelastic Scattering and Global QCD Analysis. *JHEP*, 0702:053, 2007. [arXiv:hep-ph/0611254](https://arxiv.org/abs/hep-ph/0611254), doi:10.1088/1126-6708/2007/02/053.
- [39] Daniel de Florian, Rodolfo Sassot, and Marco Stratmann. Global analysis of fragmentation functions for pions and kaons and their uncertainties. *Phys.Rev.*, D75:114010, 2007. [arXiv:hep-ph/0703242](https://arxiv.org/abs/hep-ph/0703242), doi:10.1103/PhysRevD.75.114010.
- [40] M. Anselmino, M. Boglione, U. D'Alesio, A. Kotzinian, F. Murgia, and A. Prokudin. Role of cahn and sivers effects in deep inelastic scattering. *Phys. Rev. D*, 71:074006, Apr 2005. URL: <http://link.aps.org/doi/10.1103/PhysRevD.71.074006>, doi:10.1103/PhysRevD.71.074006.
- [41] K. Ackerstaff et al. Flavor decomposition of the polarized quark distributions in the nucleon from inclusive and semiinclusive deep inelastic scattering. *Phys.Lett.*, B464:123–134, 1999. [arXiv:hep-ex/9906035](https://arxiv.org/abs/hep-ex/9906035), doi:10.1016/S0370-2693(99)00964-8.
- [42] J. Huang et al. *Phys.Rev.Lett.*, 108:052001, 2012. [arXiv:1108.0489](https://arxiv.org/abs/1108.0489), doi:10.1103/PhysRevLett.108.052001.
- [43] X. Zheng et al. Precision measurement of the neutron spin asymmetrya1n and spin-flavor decomposition in the valence quark region. *Phys. Rev. Lett.*, 92:012004, Jan 2004. URL: <http://link.aps.org/doi/10.1103/PhysRevLett.92.012004>, doi:10.1103/PhysRevLett.92.012004.

- [44] K. Abe et al. *Physics Letters B*, 452(12):194 – 200, 1999. URL: <http://www.sciencedirect.com/science/article/pii/S0370269399002440>, doi:[http://dx.doi.org/10.1016/S0370-2693\(99\)00244-0](http://dx.doi.org/10.1016/S0370-2693(99)00244-0).
- [45] D. de Florian, R. Sassot, M. Stratmann, and W. Vogelsang. Global analysis of helicity PDFs: Past - present - future. 2011. [arXiv:1108.3955](https://arxiv.org/abs/1108.3955).
- [46] Daniel de Florian, Rodolfo Sassot, Marco Stratmann, and Werner Vogelsang. Extraction of spin-dependent parton densities and their uncertainties. *Phys. Rev. D*, 80:034030, Aug 2009. URL: <http://link.aps.org/doi/10.1103/PhysRevD.80.034030>, doi:[10.1103/PhysRevD.80.034030](https://doi.org/10.1103/PhysRevD.80.034030).
- [47] M. Alekseev et al. Flavour Separation of Helicity Distributions from Deep Inelastic Muon-Deuteron Scattering. *Phys.Lett.*, B680:217–224, 2009. [arXiv:0905.2828](https://arxiv.org/abs/0905.2828), doi:[10.1016/j.physletb.2009.08.065](https://doi.org/10.1016/j.physletb.2009.08.065).
- [48] M. Alekseev et al. The Polarised Valence Quark Distribution from semi-inclusive DIS. *Phys.Lett.*, B660:458–465, 2008. [arXiv:0707.4077](https://arxiv.org/abs/0707.4077), doi:[10.1016/j.physletb.2007.12.056](https://doi.org/10.1016/j.physletb.2007.12.056).
- [49] H. Avagyan, P. Bosted, K. Griffioen, K. Hafidi, P. Rossi, et al. Studies of Spin-orbit Correlations with Longitudinally Polarized Target. [http://www.jlab.org/exp\\_prog/proposals/07/PR12-07-107.pdf](http://www.jlab.org/exp_prog/proposals/07/PR12-07-107.pdf), 2007.
- [50] J. P. Chen, J. Huang, Y. Qiang, et al. Asymmetries in Semi-Inclusive Deep-Inelastic ( $e, e'\pi^\pm$ ) Reactions on a Longitudinally Polarized  ${}^3\text{He}$  Target at 8.8 and 11 GeV. [http://www.jlab.org/exp\\_prog/PACpage/PAC37/proposals/Proposals/New%20Proposals/PR-11-007.pdf](http://www.jlab.org/exp_prog/PACpage/PAC37/proposals/Proposals/New%20Proposals/PR-11-007.pdf), 2011.
- [51] H. Gao, X. Qian, J. P. Chen, X. Jiang, et al. Target Single Spin Asymmetry in Semi-Inclusive Deep-Inelastic ( $e, e\pi^\pm$ ) Reaction on a Transversely Polarized  ${}^3\text{He}$  Target at 8.8 and 11 GeV. [http://www.jlab.org/exp\\_prog/proposals/10/PR12-10-006.pdf](http://www.jlab.org/exp_prog/proposals/10/PR12-10-006.pdf), 2010.
- [52] I.C. Cloet, Wolfgang Bentz, and Anthony William Thomas. Nucleon quark distributions in a covariant quark-diquark model. *Phys.Lett.*, B621:246–252, 2005. [arXiv:hep-ph/0504229](https://arxiv.org/abs/hep-ph/0504229), doi:[10.1016/j.physletb.2005.06.065](https://doi.org/10.1016/j.physletb.2005.06.065).
- [53] A. J. R. Puckett. [https://userweb.jlab.org/~puckett/PAC42\\_deltad/projections](https://userweb.jlab.org/~puckett/PAC42_deltad/projections), 2014.